Solution plasma synthesis of CeO_2-based powders for solid oxide fuel cell electrolytes from liquid precursors

By

Ian Altri Castillo Martinez

Under the supervision of Professor Richard Munz

Department of Chemical Engineering

McGill University, Montreal

December 2003

A thesis submitted to the Faculty of Graduate Studies and Research in partial fulfillment of the requirements of the degree of Master of Engineering

Library and
Archives Canada

Published Heritage
Branch

395 Wellington Street
Ottawa ON K1A 0N4
Canada

Bibliothèque et
Archives Canada

Direction du
Patrimoine de l'édition

395, rue Wellington
Ottawa ON K1A 0N4
Canada

Your file Votre référence
ISBN: 0-612-98518-0
Our file Notre référence
ISBN: 0-612-98518-0

NOTICE:
The author has granted a non-exclusive license allowing Library and Archives Canada to reproduce, publish, archive, preserve, conserve, communicate to the public by telecommunication or on the Internet, loan, distribute and sell theses worldwide, for commercial or non-commercial purposes, in microform, paper, electronic and/or any other formats.

The author retains copyright ownership and moral rights in this thesis. Neither the thesis nor substantial extracts from it may be printed or otherwise reproduced without the author's permission.

AVIS:
L'auteur a accordé une licence non exclusive permettant à la Bibliothèque et Archives Canada de reproduire, publier, archiver, sauvegarder, conserver, transmettre au public par télécommunication ou par l'Internet, prêter, distribuer et vendre des thèses partout dans le monde, à des fins commerciales ou autres, sur support microforme, papier, électronique et/ou autres formats.

L'auteur conserve la propriété du droit d'auteur et des droits moraux qui protège cette thèse. Ni la thèse ni des extraits substantiels de celle-ci ne doivent être imprimés ou autrement reproduits sans son autorisation.

In compliance with the Canadian Privacy Act some supporting forms may have been removed from this thesis.

While these forms may be included in the document page count, their removal does not represent any loss of content from the thesis.

Conformément à la loi canadienne sur la protection de la vie privée, quelques formulaires secondaires ont été enlevés de cette thèse.

Bien que ces formulaires aient inclus dans la pagination, il n'y aura aucun contenu manquant.

Canada

“… a mis padres Alfredo y Patricia ...”

“... a mi hermana lo ...”

“... a mi canadiense Heather ...”

Abstract

The main objective of this thesis was to explore, characterize and evaluate different CeO_2-based electrolyte materials that could be employed to replace the existing yttria-stabilized zirconia oxide used as the electrolyte component of intermediate temperature solid oxide fuel cells (SOFCs). The electrolyte materials were synthesized using a radio frequency inductively coupled plasma reactor. CeO_2-based fine powders doped with different compositions of Gd, Sm or Y were synthesized from nitrate salts dissolved in water. The powders were analyzed using X-ray diffraction, inductively coupled plasma (ICP), SEM and EDS (energy dispersive spectroscopy). It was demonstrated that the concentrations of Ce and dopants fed in the solutions were retained in the synthesized powders. The products were all crystalline and had multimodal size distributions. The effect of plasma synthesis parameters, i.e. plasma power, reactor pressure, and plasma flow rate on particle size distribution was studied. This analysis provides fundamental understanding of the mechanism of particle formation and collection in thermal plasma environments.

Résumé

L'objectif principal de cette thèse a été d'explorer, caractériser et analyser différentes céramiques à base de CeO_2 , qui peuvent être utilisées pour substituer le zircone stabilisé par l'yttria existant comme matériau électrolytique de base pour le SOFC (solid oxide fuel cell ou pile à combustible à électrolyte solide) de température intermédiaire. Les matériaux électrolytiques ont été synthétisés en utilisant un réacteur de plasma de solution RF-couplé inductivement. Les poudres céramique à base de CeO_2 dopées avec différentes compositions de Gd, Sm et Y ont été synthétisées à partir des sels de nitrate dissous dans de l'eau. Les poudres ont été analysées par diffraction à rayons-X, ICP, microscopie électronique à balayage (MEB), et EDS (spectroscopie d'énergie dispersive). Il a été démontré que les concentrations de Ce et de dopant dans les poudres synthétisées restent égales à celles dans la solution injectée. Les produits étaient tous cristallins et avaient une distribution de taille multimodal. L'effet des paramètres de synthèse de plasma, par exemple la puissance du plasma, la pression du réacteur et le débit de gaz de plasma sur la distribution de taille de particule a été étudié. Cette analyse fournit une compréhension fondamentale du mécanisme de formation de particules dans le plasma.

Acknowledgments

I would like to express my gratitude to Professor Richard Munz for his moral support, edifying discussions and thoughtful guidance, without which this thesis would never have been written.

I would like to thank Professor François Gitzhofer for his support and helpful discussions during my experimental work carried out at University of Sherbrooke as well as to all the other members of the CRTP Sherbrooke, especially the Ph.D. candidate Glen Lemoine for his patience and invaluable advice. My special thanks also to Mr. Hugo Besaillon for the time spent showing me how to operate the RF-plasma equipment.

Many thanks to the non-academic staff that help me carrying out my research activities: Ms. Monique Riendeau for the X-ray diffraction analysis, Ms. Helen Campbell for the SEM training, Mr. Stéphane Gutierrez for the Mastersizer 2000 particle size distribution analysis, and Mr. Frank Caporuscio, Mr. Luciano Cusmich and Mr. Serge Gagnon for their technical support.

I thank the present members of the CRTP McGill with special mention to Victor Silla and Luis Aguilera for their company and advice. I would like to express my gratitude to Miguel Baqueiro and Julien Gabert for his help in the translation of the abstract to French.

Finally, I wish to acknowledge the financial support provided by the Natural Science and Engineering Research Council of Canada (NSERC), Fonds de Recherche sur la Nature et Technologies (FQRNT), Eugene Lamonthe Scholarship and McGill internal fee waivers.

Table of contents

ABSTRACT I

RESUME II

ACKNOWLEDGMENTS III

TABLE OF CONTENTS IV

LIST OF FIGURES VI

LIST OF TABLES VIII

CHAPTER 1 INTRODUCTION 1

- 1. A Problem definition 2
- 1. B Scope of the project and objectives 4
- 1. C Thesis outline 5

CHAPTER 2 LITERATURE REVIEW 7

- 2. A Solid oxide fuel cells (SOFCs) 7
  - 2.A.1 History 7
  - 2.A.2 Types of fuel cells and environmental impact 7
  - 2.A.3 Operation, configuration and applications 9
  - 2.A.4 Components 12
    - 2.A.4.1 Electrolyte 12
    - 2.A.4.2 Anode 16
    - 2.A.4.3 Cathode 18
    - 2.A.4.4 Interconnect 18
- 2. B Nature and composition of electrolyte powders and their material precursors 19
  - 2.B.1 Nature and composition of electrolyte powders 19
  - 2.B.2 Nature and behavior of electrolyte material precursors 21
    - 2.B.2.1 Type of feeding 21
    - 2.B.2.2 Evaluation of different liquid precursors 22
    - 2.B.2.3 Description of calcinations mechanisms of precursors 23
- 2. C Plasma processing of materials 25
  - 2.C.1 Thermal plasmas 25
  - 2.C.2 RF (radio frequency) inductively coupled discharges 25
  - 2.C.3 Thermal plasma synthesis of ceramics 27
- 2. D Conventional and plasma applications for the production of SOFC components 28
  - 2.D.1 Conventional methods for the production of SOFC components 28
  - 2.D.2 Plasma methods for the production of SOFC components 30

CHAPTER 3 EXPERIMENTAL TECHNIQUES AND METHODOLOGY 32

- 3. A Experimental setup 32
  - 3.A.1 Description 32
  - 3.A.2 Operation 32
  - 3.A.3 Recompilation of experimental conditions 34
- 3. B Electrolyte powder production and characterization 35
  - 3.B.1 Atomized droplet size distribution 35
  - 3.B.2 X-Ray diffraction 36
  - 3.B.3 Inductively coupled plasma (ICP) 36
  - 3.B.4 Powder preparation for SEM 37

3.B.5 Laser diffraction for particle size distribution 38
3. C Image analysis for particle size determination 38
3.C.1 Commercial software 38
3.C.2 Developed algorithm (In-house PSD software) 40
3.C.3 PSD methodology assessment 44
CHAPTER 4 EXPERIMENTAL RESULTS (PART 1). SOFC ELECTROLYTE POWDERS 46
4. A Atomization of the solutions 46
4. B X-ray diffraction analysis 51
4. C Metal analysis of products (ICP) 56
4. D Local composition and particle morphology by energy dispersive spectroscopy (EDS) and scanning electron microscopy (SEM) 57
4.D.1 Local composition by energy dispersive spectroscopy (EDS) 57
4.D.2 Particle morphology by scanning electron micrographs 62
CHAPTER 5 EXPERIMENTAL RESULTS (PART 2) PARTICULATE FORMATION AND ANALYSIS 67
5. A Particle size distribution analysis (SEM and laser diffraction) 67
5. B Effect of selected plasma operating parameters and collection regions on product size 71
5.B.1 Effect of selected plasma operating parameters on product size 71
5.B.2 Effect of collection regions on product size 73
5. C Study of nanopowder distributions (SEM image analysis) 73
5. D Proposed mechanism of powder formation 78
5. E Study of particle collection mechanisms 80
CHAPTER 6 CONCLUSIONS, FUTURE WORK AND RECOMMENDATIONS 83
6. A Conclusions 83
6. B Future work and recommendations 85
REFERENCES 88
APPENDIX A. PHYSICAL PROPERTIES OF SELECTED OXIDES, IONIC CONDUCTIVITY THEORY OF OXIDES AND SAMPLE CALCULATIONS. 94
a. Physical properties of selected solid oxides 94
b. Theory of ionic conductivity in fluorite oxides 95
c. Calculation of the density of solid oxide mixtures 97
d. Calculation of the atomized droplet size 97
e. Sensitivy analysis 97
f. Scherrer's formula 98
g. Bartlett's test 98
h. Comparison of two means of independent samples 98
APPENDIX B. CALIBRATION CURVES 100
a. Peristaltic pump calibration curve 100
b. Rotameter calibration curve 100
APPENDIX C. IMAGE ANALYSIS 101
a. Commercial software methodology 101
b. Developed algorithm methodology 101

List of figures

Figure 2.1 Schematic diagram showing the operating principles of a SOFC running on natural gas (*Ormerod, 2003*) 10
Figure 2.2 Schematic view of the Sulzer Hexis micro-CHP (combined heat and power) stack for residential applications (*Steele et al, 2001*) 10
Figure 2.3 Flowsheet of SOFC for electricity and heat supply to an administration building (*Silveira et al, 1999*) 11
Figure 2.4 Flowsheet of SOFC for industrial applications (maximum electricity generation) (*Silveira et al, 1999*) 12
Figure 2.5 Ionic conductivity of fluorite oxides (*Inaba et al, 1996*) 13
Figure 2.6 Ion conductivity of doped ceria at 1073K against the radius of dopant cation, r_c shown the horizontal axis is the critical of the divalent or trivalent cation. (*Inaba et al, 1996*) 14
Figure 2.7 Composition dependence of conductivities for $(CeO_2)_{1-x}(SmO_{1.5})_x$, ○ 900 °C, Δ 800 °C, □ 700 °C, ● 600 °C, ▲ 500 °C, broken line $(ZrO_2)_{1-x}(CaO)_x$ at 800 °C (*Eguchi, 1997*) 21
Figure 2.8 Isothermal conductivity of $Ce_{1-x}Gd_xO_{2-x/2}$ at 500 °C as a function of Gd concentration showing data for the lattice conductivity, grain boundary and total contributions (*Steele, 2000*) 21
Figure 2.9 Lattice and grain boundary conductivities at 500 °C and 700 °C for Y-doped CeO_2 samples (*Tian et al, 2000*) 21
Figure 2.10 a) Thermolysis curves of selected rare earth nitrates, 1) $La(NO_3).6H_2O$, 2) $Ce(NO_3).6H_2O$, 3) $Pr(NO_3).6H_2O$, 4) $Nd(NO_3).6H_2O$, 5) $Sm(NO_3).6H_2O$, (Wendlandt, 1956) ; b) Thermolysis curves of selected rare earth chlorides A) $YCl_3.6H_2O$, B) $LaCl_3.6H_2O$, C) $PrCl_3.6H_2O$, D) $CeCl_3.6H_2O$, (Wendlandt, 1957) 24
Figure 2.11 Schematic diagram of the induction plasma torch (Tekna PL-35 torch) (*Merkhouf et al, 2000*) 26
Figure 3.1 Experimental setup 33
Figure 3.2 Malvern atomized droplet size analyzer setup (Courtesy of Linda Oukacine) 35
Figure 3.3 Scion software interface showing the grey scale values along a characteristic superimposed line 40
Figure 3.4 Sample results of the in-house PSD software showing the grey values of three different parallel lines across the SEM micrograph (left y-axis) and showing the results representing the particles counted along the three lines (i.e. the number of ones) (right y-axis) as a function of location (in pixels). The dotted lines represent the beginning or end of particles 42
Figure 3.5 Sample results of the in-house PSD software showing a) the length of all particles sampled, b) the number based PSD histogram, and c) its corresponding cumulative PSD, d) volume based PSD histogram and e) its corresponding cumulative PSD 43
Figure 4.1 Sensitivity analysis for airblast atomizer based on a correlation proposed by Lefebre (*Lefebre, 1989*) 47

Figure 4.2 Different atomization conditions for the Tekna air blast atomization probe 47
Figure 4.3 Atomized droplet size distribution: a) $Ce_{0.9}Gd_{0.1}O_{1.95}$; b) $Ce_{0.9}Sm_{0.1}O_{1.95}$; c) $Ce_{0.88}Y_{0.12}O_{1.94}$ precursor solutions. Liquid flow rate 6 ml/min, Atomizing gas (air) flow rate 6.5 slpm , atomized probe aperture ¾ turn opening 50
Figure 4.4 X-ray diffraction patterns of Sm-Ce synthesized powders. Sm_2O_3 and CeO_2 shown as reference patterns 52
Figure 4.5 X-ray diffraction patterns of Gd-Ce synthesized powders. Gd_2O_3 and CeO_2 shown as reference patterns. 53
Figure 4.6 X-ray diffraction patterns of Y-Ce synthesized powders. Y_2O_3 and CeO_2 shown as reference patterns 54
Figure 4.7 Comparison of selected X-ray diffraction patterns of Gd-Y-Sm-Ce and CeO_2 synthesized powders. CeO_2 shown as reference pattern 55
Figure 4.8 X-ray diffraction patterns of doped (a) $Ce_{1-x}Gd_xO_{2-x/2}$ and (b) $Ce_{1-x}Sm_xO_{2-x/2}$ produced by the oxalate co-precipitation route (Zha et al, 2003) 56
Figure 4.9 EDS patterns of Gd-Ce oxide powders (100 sec. live time, 15 kV, 35% dead time (DT) and 12 mm working distance (WD)) 59
Figure 4.10 EDS patterns of Sm-Ce oxide powders (100 sec. live time, 15 kV, 35% DT and 12 mm WD) 60
Figure 4.11 EDS patterns of Y-Ce oxide powders (100 sec. live time, 15 kV, 35% DT and 12 mm WD) 61
Figure 4.12 EDS patterns of CeO_2 oxide powders (100 sec. live time, 15 kV, 35% DT and 12 mm WD) 61
Figure 4.13 a) $Ce_{0.9}Gd_{0.1}O_{1.95}$; b) $Ce_{0.85}Gd_{0.15}O_{1.925}$; c) $Ce_{0.8}Sm_{0.2}O_{1.9}$; d) $Ce_{0.85}Sm_{0.15}O_{1.925}$ 63
Figure 4.14 a) $Ce_{0.88}Y_{0.12}O_{1.94}$; b) $Ce_{0.85}Y_{0.15}O_{1.925}$; c) DMF dispersion CeO_2; d) H_2O dispersion CeO_2 64
Figure 4.15 a) $Ce_{0.9}Gd_{0.1}O_{1.95}$; b) $Ce_{0.85}Gd_{0.15}O_{1.925}$; c) $Ce_{0.8}Gd_{0.2}O_{1.9}$; d) $Ce_{0.9}Sm_{0.1}O_{1.95}$; e) $Ce_{0.85}Sm_{0.15}O_{1.925}$; f) $Ce_{0.8}Sm_{0.2}O_{1.9}$; 66
Figure 5.1 Particle size distribution of selected synthesized oxide powders using laser diffraction 69
Figure 5.2 SEM micrographs of a) $Ce_{0.9}Gd_{0.1}O_{1.95}$, b, c) $Ce_{0.8}Sm_{0.2}O_{1.9}$-R, d) $Ce_{0.88}Y_{0.12}O_{1.94}$, e) CeO_2, f) $Ce_{0.8}Sm_{0.15}O_{1.9}$, 70
Figure 5.3 Schematic temperature histories of the different types of particles (T_b: boiling temperature, T_m: melting temperature, T_r: reaction or calcination temperature) 71
Figure 5.4 a) Comparison of different operating parameters for selected synthesized powders at 25 kW; b) PSD of samples from two different collection regions 73
Figure 5.5 Particle size distribution of the synthesized samples based on their SEM micrographs using the in-house PSD software 75
Figure 5.6 a) 15% mole Y powders collected from the metallic filters; b) 15% mole Gd powders collected from the main reactor walls 77
Figure 5.7 A modified particle formation mechanism for RF-ICP thermal plasma synthesized particles starting form liquid precursors 79
Figure 5.8 Different physical phenomena affecting particle collection 82

List of tables

Table 2.1 Technical characteristics of selected fuel cells 8

Table 2.2 Typical SOFC air emissions from one year of operation (*Stambouli et al, 2002*) 9

Table 2.3 Ionic conductivity data for selected electrolyte compositions 15

Table 2.4 Summary of the thermal decomposition of the dopants used (M=Y, Sm, Gd) (Wendland, 1956 & 1957) 24

Table 3.1 Summary of experimental conditions 34

Table 3.2 Summary of solution preparation 34

Table 4.1 Selected oxide compositions for plasma synthesis 46

Table 4.2 Experimental and calculated properties selected synthesized products and liquid precursors 49

Table 4.3 Estimated crystallite size of the synthesized ceramic powders 55

Table 4.4 ICP analysis of synthesized oxide powders 57

Table 5.1 Volume and number based median and standard deviation values calculated from the PSD obtained from the in-house software for different synthesized conditions 76

Table 5.2 Predominant particle collection region for the different types of particles 80

Chapter 1 Introduction

"... We learn more about power when we lose it..." (*Time 2003*)

The generation of electrical energy by clean, efficient and environmental-friendly means is now one of the major challenges for engineers and scientists (*Stambouli et al, 2002*). One of the best ways to generate that energy is by the use of solid oxide fuel cells (SOFCs). These cells convert chemical energy of a fuel gas directly into electrical work without the need of combustion. Therefore much lower emissions of hydrocarbon pollutants, sulfur and nitrogen oxides and carbon dioxide are achieved. Fuel cells have been applied successfully in Japan, U.S.A. and Europe. Electrical-generation efficiencies of 70% are possible nowadays, along with the recovery of residual heat, mostly in the form of steam (*Silveira et al, 1999*).

SOFC research has extended worldwide. It has been noted, recently, that about 40 companies are working on SOFC. These companies include Global Thermoelectric's Fuel Cell Division, Cermatec-Advanced Ionic Technologies, and Siemens Westinghouse. The fuel cell built by Siemens Westinghouse combined with the microturbine supplied by Northen Research and Engineering Corporation is a case of particular importance, because the 220 kW SOFC running on natural gas achieved an efficiency of 60% in a year of operation. Further, other prototype cells have operated for 8 years demonstrating the ability to withstand more than 100 thermal cycles with a voltage degradation of less than 0.1% per thousand hours (*Stambouli et al, 2002*).

It is only in the last two decades that fuel cells have offered a realistic prospect of being commercially viable, despite being first demonstrated over 160 years ago (*Ormerod, 2003*). The major factor impeding the progress of fuel cell technology has been its cost. However, significant advances in the development of both materials with improved properties and different manufacturing processes in the last 20 years have made fuel cells a realistic proposition to compete with conventional power generation technologies.

1. A Problem definition

The main concern regarding SOFCs is that there are severe demands on the materials that are used for the principal cell components, i.e. the electrolyte, anode, cathode and interconnect. All components must possess chemical and physical stability in the appropriate chemical environment (oxidizing and/or reducing), be chemically compatible with the other components and have proper conductivity (either ionic or electronic) (*Ormerod, 2003*). In addition, these components must have similar coefficients of thermal expansion to avoid separation or cracking during fabrication and operation. Each component serves a particular function and must be tailored to achieve this function without interfering with the entire cell operation. For instance, the electrolyte and the interconnect must be dense to prevent gas mixing, whereas the anode and the cathode must be porous to allow gas transport to the reaction sites (*Minh, 1993*). As a consequence of the severe restrictions in the materials of construction, the choice of materials employed to build SOFC has been very limited and only relatively weak and brittle components have been used.

Almost all SOFCs currently being developed employ an yttria-stabilized zirconia (YSZ) electrolyte with a strontium-doped lanthanum manganite ($La_{1-x}Sr_xMnO_3$) cathode and a mixed nickel/yttria-stabilized zirconia (YSZ) cermet anode, and use doped lanthanum chromite ($LaCrO_3$) as the interconnect. Conventional zirconia based SOFCs have an optimum performance when operated at temperatures above 850 °C. These relatively high operating temperatures place further demands on the materials used as interconnects, for manifolds and sealing. Further, high cell temperatures affect cell components by: 1) promoting the sintering of the nickel particles present in the anode which affects its mechanical stability and electronic conductivity, 2) favoring the reaction of cathode materials such as manganese and/or cobalt with the electrolyte, and 3) increasing the thermal mismatch between the electrolyte and the electrodes. Moreover, the long time that is required to heat up and cool down the system could also be decreased if the SOFC is operated at lower temperatures. It is also of great interest to replace the $LaCrO_3$-based interconnects with inexpensive metallic interconnects (in particular by ferritic stainless steel composites), which can only be implemented at temperatures lower than 700 °C (*Ormerod, 2003*).

There are also inconveniences associated with the production of the cells, mainly the great number of steps required to manufacture SOFC components. This increases both the cell production cost and the time to manufacture its components. Currently, SOFCs are produced using conventional ceramic processes such as tape casting, screen printing, wet powder spraying, and sintering. All these processes are time-consuming and some occur at high temperatures, far above cell operating temperatures, i.e. 1,000 °C (*Schiller et al, 2003*). Hence, not only the cell components but also the SOFC manufacturing routes must be improved.

The heart of the SOFC is the electrolyte and the operating temperature of the cell is governed by its nature, i.e. its oxygen ionic conductivity and thickness. Therefore, there are two possible approaches to decrease the cell operating temperature. The first is to reduce the electrolyte thickness while the second is to search for alternative materials with higher oxygen ion conductivities at lower temperatures. Fine spherical particles with a narrow size distribution and uniform microstructure are desired as precursors to reduce electrolyte thickness. This type of powders provides high reactivity and high packing density (*Minh 1993*).

The development of ultra-thin, dense and non porous electrolyte films composed of doped ceria or of lanthanum gallate are the most promising alternatives. Gadolinia-doped ceria (CGO or $Ce_{1-x}Gd_xO_{2-x/2}$) offers excellent promise as a potential electrolyte for lower temperature SOFCs (*Ormerod, 2003; Steele, 2000*); mainly due to its higher ionic conductivity than YSZ at lower temperatures, and to its inertness towards the cathode and anode materials. Unfortunately, at sufficiently high temperatures (above 700 °C) and under reducing conditions, such as those present in the anode, ceria undergoes partial reduction to Ce^{3+}, which leads to electronic conductivity. This significantly lowers the efficiency of the SOFC, and leads to an undesired structural change. If the operating temperature of the CGO is lowered to 500 °C, then any electronic conductivity can be neglected, but at such low electrolyte temperatures the main problem lies with the development of sufficiently active cathode materials (*Ormerod, 2003*). Nonetheless, gadolia-doped ceria along with samarium-doped ceria and yttria-doped ceria remain the most promising electrolyte materials and have been used in the present study.

In terms of the SOFC manufacturing routes, the use of thermal plasma synthesis and thermal plasma spraying from liquid precursors has demonstrated very good results in the production of SOFC components (*Gitzhofer et al, 2000*). This is because thermal plasma synthesis allows the production of homogeneous and dense spherical particles of different materials and compositions. These synthesized particles are used to produce low porosity oxygen ion conducting electrolyte layers of reduced thickness with low cell resistance. Further, thermal plasma spraying permits rapid particle deposition at rates that are higher than those obtained with other approaches such as physical or chemical vapor deposition Finally, no further thermal post-treatment is required after the SOFC layers are deposited (*Schiller et al, 2003*).

1. B Scope of the project and objectives

It has been stated that the production of SOFC must consist of an improvement of their individual components as well as an improvement of the cell manufacturing techniques. In 1999, researchers at the CRTP (Centre de Recherche en Technolgie des Plasmas) began a project to investigate the combinatorial chemistry production of the different cell components (cathode, anode, electrolyte and internal reformer) using thermal plasma technology (*CFI, 1999*). The project also encompasses the diagnosis and evaluation of the individual components of the cell and of the overall cell performance; ultimately, the project's aim is an automated, quick and reliable in-line manufacturing of SOFCs for industrial applications. Thermal plasma technology was proposed as a novel alternative to manufacture each cell component due to the short time required to produce the components in a plasma environment.

This interdisciplinary project was subdivided and each subdivision will carry out research on the four major cell components, i.e. cathode, anode, electrolyte and internal reformer. The current thesis is concerned with the electrolyte subdivision.

The main objective of this thesis was to obtain electrolyte powders of different compositions with suitable dopants using appropriate starting materials. The powders were to be of the most promising electrolyte compositions based on the known SOFC electrolyte requirements, i.e. maximum ionic conductivity and dense layers of tightly packed particles. The powders will be the starting material for the production of electrolyte layers by either other plasma treatment or by conventional sintering methods.

The different electrolyte powders were synthesized from liquid precursors using a radio frequency inductively coupled plasma (RF-ICP). In addition, the investigation of the synthesis mechanism for oxide formation from liquid precursors was studied. Most of this analysis was based on the characterization of particle size and how particle size could be correlated to plasma processing parameters.

Thereby, the objectives of this research can be stated as follows:

1. The production of doped CeO_2-based powders from liquid precursors using RF-ICP.
2. The characterization and evaluation of the produced particles as possible raw materials for SOFC electrolyte production.
3. The study of the formation mechanism of CeO_2-based powders from liquid precursors in an oxidizing plasma environment.
4. The evaluation of the effect of plasma operating parameters on particle size and morphology.

1. C Thesis outline

This thesis is divided into 6 different chapters and 3 appendices. The appendices include equipment calibration, some physical data of the materials used, and the mathematical formulae employed to calculate relevant experimental data. The source code of the in-house software developed is also included. A brief description of each chapter is now given.

Chapter 1: Introduction.

This chapter includes an introduction, a definition of the scope of the thesis and a statement of objectives.

Chapter 2: Literature review.

The literature review is divided into four major parts. First, solid oxide fuel cells (SOFC) are described, i.e. their components and cell operation. Second, the nature and composition of electrolyte materials is discussed. Third, an explanation of how the radio frequency inductively coupled plasma operates is enunciated as well as how it can be applied to the production of ceramics. Finally, the application of thermal plasmas in SOFC research is reviewed.

Chapter 3: Experimental techniques and methodology.

The different experimental techniques used to characterize the materials produced in this work are described. Also, the experimental setup used and its operation is discussed.

Chapter 4: Experimental results. Part 1.

The results obtained from the characterization of the different CeO_2 based powders synthesized using thermal plasma are presented, i.e. X-ray diffraction, inductively coupled plasma (ICP), SEM, and energy dispersive spectroscopy (EDS).

Chapter 5: Experimental results. Part 2.

The analysis of the size distribution of the synthesized powders is presented in this chapter. A detailed particle formation mechanism starting from liquid droplets and ending with solid powders is described. Finally, particle collection mechanisms related to the synthesized powders are discussed.

Chapter 6: Conclusions, future work and recommendations.

This chapter summarizes the major contributions enumerated in this study and provides recommendations for future research endeavors.

Chapter 2 Literature review

The literature review consists of four sections. The first is a concise description of the solid oxide fuels cells, their operation and main components. The second is an analysis of the chemical composition of SOFC electrolyte materials as well as of the suitable precursors for plasma synthesis. The third describes radio frequency inductively coupled thermal plasmas (RF-ICP), and their applications towards the production of oxides and oxide coatings. Finally, the last section discusses applications of radio frequency thermal plasmas to the production of SOFC components.

2. A Solid oxide fuel cells (SOFCs)

2.A.1 History

Despite their modern high-tech allure, fuel cells have been known for more than 160 years. The solid oxide fuel cell was first conceived following the discovery of solid oxide electrolytes in 1899 by Nerst. He reported that the conductivity of pure metal oxides rose only very slowly with temperature and remained relatively low, whereas mixtures of metal oxides can possess dramatically higher conductivities. Many mixed oxides which exhibit high conductivity at elevated temperatures were quickly identified, including the particularly favorable composition of 85% zirconium oxide and 15% yttrium oxide patented by Nerst in 1899. In 1905 Haber filed the first patent on fuel cells with a solid electrolyte, using glass and porcelain as the electrolyte material, and platinum and gold as the electrode materials. Despite a very significant search by Baur and other researchers for suitable materials for SOFC operation, the development of SOFC was hindered until the 1960s. In the early 1960s a rapidly increasing number of patents was filed associated to SOFC technology. Advances in preparation and production methods through the 1970s led to the development of considerably thinner electrolytes, which significantly increased cell performance (*Ormerod, 2002*). In the last two decades, a major effort has been devoted to develop commercial SOFCs in research centers and industrial power generation facilities.

2.A.2 Types of fuel cells and environmental impact

Fuel cells are generally classified by the chemical characteristics of the electrolyte used as the ionic conductor in the cell, as summarized in Table 2.1. The first five types are characterized by their low to medium temperature of operation (50 to 210 °C), their relatively low electrical generation efficiencies (40 to 50 % when operated on readily available fuels such as methanol and hydrocarbons, 50 % when pure hydrogen fuel is used). The latter three types are characterized by their high temperature of operation (600 to 1000 °C), their ability to utilize methane directly in the fuel cell and their higher efficiencies (45 to 60 % for common fuels such as natural gas or methanol and 70 % with heat recovery) (*Stambouli, 2002*).

Table 2.1 Technical characteristics of selected fuel cells

Technical characteristics of different fuel cells

Types of fuel cell	Electrolyte	Operating T	Fuel	Oxidant	Efficiency
Alkaline (AFC)	potassium hydroxide (KOH)	50–200°C	pure hydrogen, or hydrazine	O_2/Air	50–55%
Direct methanol (DMFC)	polymer	60–200°C	liquid methanol	O_2/Air	40–55%
Phosphoric acid (PAFC)	phosphoric acid	160–210°C	hydrogen from hydrocarbons and alcohol	O_2/Air	40–50%
Sulfuric acid (SAFC)	sulfuric acid	80–90°C	alcohol or impure hydrogen	O_2/Air	40–50%
Proton-exchange membrane (PEMFC)	polymer, proton exchange membrane	50–80°C	less pure hydrogen from hydrocarbons or methanol	O_2/Air	40–50%
Molten carbonate(MCFC)	molten salt such as nitrate, sulphate, carbonates…	630–650°C	hydrogen, carbon monoxide, natural gas, propane, marine diesel	CO_2/O_2/Air	50–60%
Solid oxide (SOFC)	ceramic as stabilised zirconia and doped perovskite	600–1000°C	natural gas or propane	O_2/Air	45–60%
Protonic ceramic (PCFC)	thin membrane of barium cerium oxide	600–700°C	hydrocarbons	O_2/Air	45–60%

Among these cells, SOFCs are the most promising alternative because they have a wide range of operation and can run on natural gas. SOFCs are also resistant to carbon monoxide, which is electrochemically oxidized to CO_2 at the anode. In contrast, PEM fuel cells are highly susceptible to poisoning by CO, and thus require complex and expensive external processing of hydrocarbon feeds to convert all the CO to CO_2 (*Ormerod, 2003*). Additionally, SOFCs are liquid free which eliminates potential problems such as corrosion and loss of electrolyte.

The environmental impact of SOFC implementation depends upon the source of fuel used. If pure hydrogen is used, fuel cells have virtually no emissions except water and heat. However, hydrogen is rarely used due to problems with storage and transportation. The most common fuel, especially for stationary applications, is natural gas, which is cheap, abundant and readily available. Hydrogen must be extracted from natural gas through a series of reforming reactions and it is during this stage that most of the pollutant emissions associated with SOFCs operation are generated.

Compared to other fuel cells or power generation units, SOFC have a much lower fuel consumption to produce a given amount of electricity, even if they run on natural gas, as a result of their higher energy efficiency. Also, emissions of NO_x, SO_x and particulates are very low which greatly decreases the formation of acid rain and the emission of smog-causing pollutants. Further, if pure hydrogen is used as fuel, less CO_2 is produced, and near-zero levels of CO_2 could be achieved (Table 2.2).

Table 2.2 Typical SOFC air emissions from one year of operation (*Stambouli et al, 2002*)

Air emissions[a]	SO_X	NO_X	CO	Particles	Organic compounds	CO_2
Fossil fuelled plant	12,740	18,850	12,797	228	213	1,840,020
SOFC system	0	0	32	0	0	846,300

[a] kgs of emissions per 1650 MWh from one year full operation

2.A.3 *Operation, configuration and applications*

A fuel cell consist of two electrodes (the anode and the cathode) separated by an electrolyte (Fig. 2.1). Fuel (e.g. hydrogen or natural gas) is fed to the anode where it is oxidized and electrons are released to the external circuit. The electron flow (from the anode to the cathode) through the external circuit produces direct-current electricity. The electrolyte conducts ions between the two electrodes. SOFCs are connected in electrical series to build voltage and a series of cells is referred to as a stack. Stacks are connected through components called bipolar separators or interconnects, which have the dual function of distributing the fuel and air to the anode and cathode respectively, as well as of providing the electrical contact between adjacent cells (*Minh, 1993*).

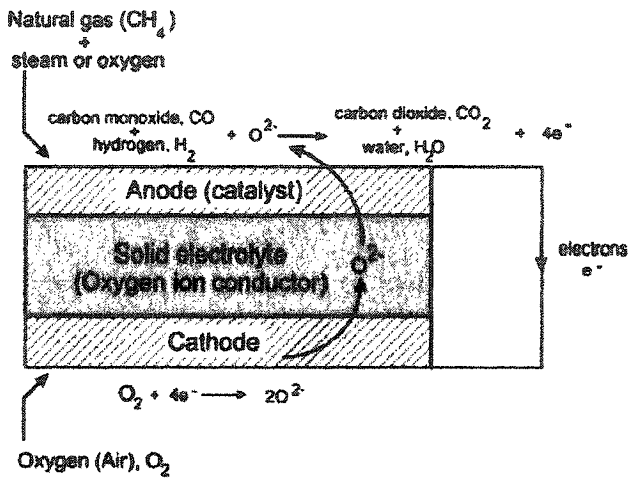

Figure 2.1 Schematic diagram showing the operating principles of a SOFC running on natural gas (*Ormerod, 2003*)

To minimize sealing requirements, many intermediate temperature solid oxide fuel cells (IT-SOFCs) stacks have adopted a circular design in which the fuel and air are introduced by means of an appropriate manifold at the centre of cathode-electrolyte-anode structures. Arrangements are made to distribute the air and fuel gases over the cathode and anode, and the flow rates are adjusted to ensure almost complete conversion of the fuel by the time it reaches the stack periphery. Unreacted fuel and air are then combusted without large temperature changes. This design features minimum sealing problems and allows limited thermal cycling for start-up and maintenance. One particular example is the Sulzer Hexis micro-CHP (combined heat and power) configuration designed for residential accommodation Fig. 2.2.

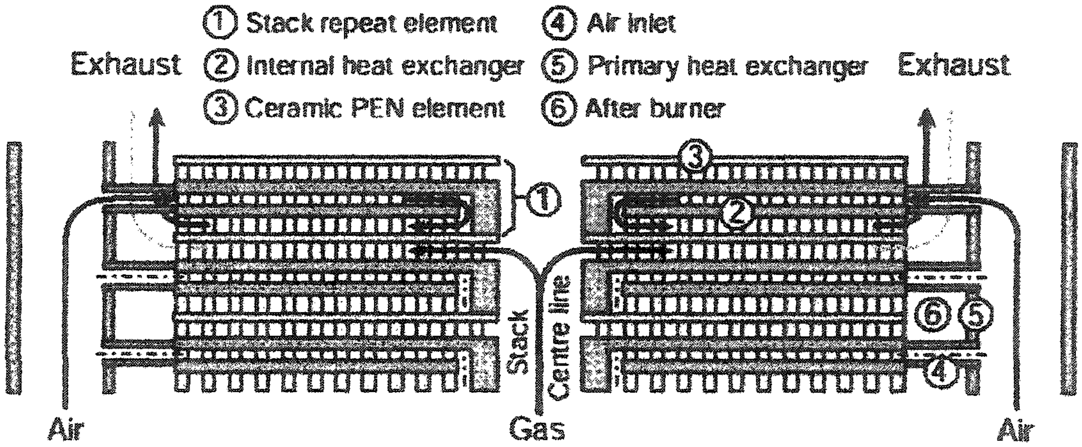

Figure 2.2 Schematic view of the Sulzer Hexis micro-CHP (combined heat and power) stack for residential applications (*Steele et al, 2001*)

The potential applications of fuel cells in society are ever increasing and range from very small-scale ones requiring only a few Watts to a large-scale distributed power generation of hundreds of MWatts. SOFCs are especially suited for highly-populated urban areas where localized pollution is a major issue as a result of their better utilization of fossil and renewable fuels, such as biomass and landfill gas. Further, SOFCs can provide both all the power and hot water from a single system to individual households, larger residential units and business and industrial facilities. This offers a greater efficiency than the current situation where electricity is distributed from a small number of centralized power stations, while heating is supplied by decentralized boiler units. In the short term, SOFCs can cope with the developing market where there is a real need for high quality, uninterrupted power supply. Such applications include information technology companies, airports and hospitals (*Ormerod, 2003*).

Two flowsheets showing how SOFCs could meet the present needs for electricity and heat for both industrial and commercial applications are provided in Fig. 2.3 and 2.4. The first depicts the decentralized power and heat supply in the 1 MW range. The second is to be used to generate power for a central power station. In this case a gas and steam turbine combined cycle is added so that an electrical efficiency of about 70 % could be achieved.

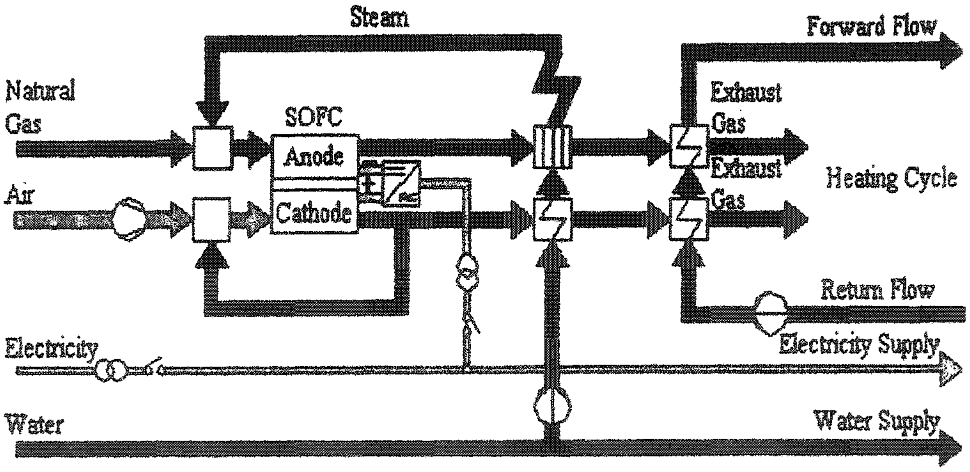

Figure 2.3 Flowsheet of SOFC for electricity and heat supply to an administration building (*Silveira et al, 1999*)

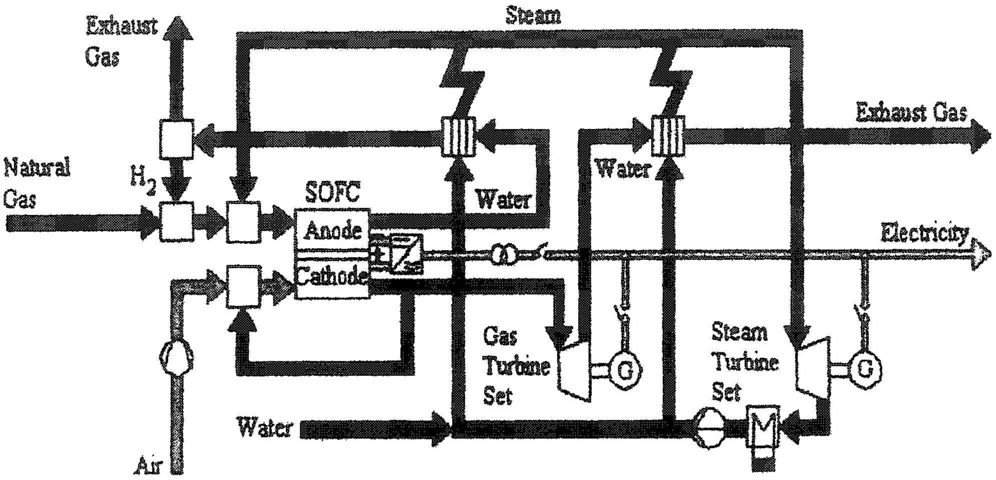

Figure 2.4 Flowsheet of SOFC for industrial applications (maximum electricity generation) (*Silveira et al, 1999*)

2.A.4 Components

2.A.4.1 Electrolyte

For a better understanding of the ensuing discussion a brief review of the conductivity of an ionic material is presented here. An electric current results from the motion of electrically charged particles in response to forces that act on them from an externally applied electric field. Within most solid materials a current arises from the flow of electrons, which is termed electronic conduction. In addition, for ionic materials it is possible that a net motion of charged ions (both cations and anions) produces a current; this is called ionic conduction. Thus an electric current will result from the net movement of charged ions and from any electron motion. Of course, anion and cation migrations will be in opposite directions. The total conductivity (or electrical conductivity) of an ionic material is thus equal to the sum of both electronic and ionic contributions (*Callister, 1997*). A complete description of the phenomena affecting ionic materials was compiled by Sorensen (*Sorensen, 1981*)

Stabilized zirconia (ZrO_2), especially yttria-stabilized zirconia (YSZ), is the most common electrolyte in SOFCs because it possesses an adequate level of oxygen-ion conductivity and exhibits desirable stability in both oxidizing and reducing atmospheres. It is also unreactive towards other components used in the SOFC. Pure ZrO_2 is monoclinic at room temperature and undergoes phase transition to a tetragonal structure above 1,170 °C and to the cubic structure above 2,370 °C (see appendix A for structures). Yttria, along with some other aliovalent oxides commonly referred to as dopants (e.g CaO, MgO, Gd_2O_3, Sc_2O_3, Sm_2O_3, and other rare earth oxides) shows a high solubility in ZrO_2. Yttria also allows the stabilization of the zirconia in the cubic fluorite structure from room temperature to its melting point (2,680 °C). Further, dopant addition increases the concentration of oxygen ion vacancies in the ZrO_2 solid structure, which in turn increases its ionic conductivity. Despite the success of YSZ, many studies have been performed with other materials looking for alternative oxides. This is a result of the high operating temperatures (>800 °C) required to obtain the desired ionic conductivity of YSZ for SOFC operation. The ionic conductivities of selected solid oxide electrolytes are shown in Fig. 2.5.

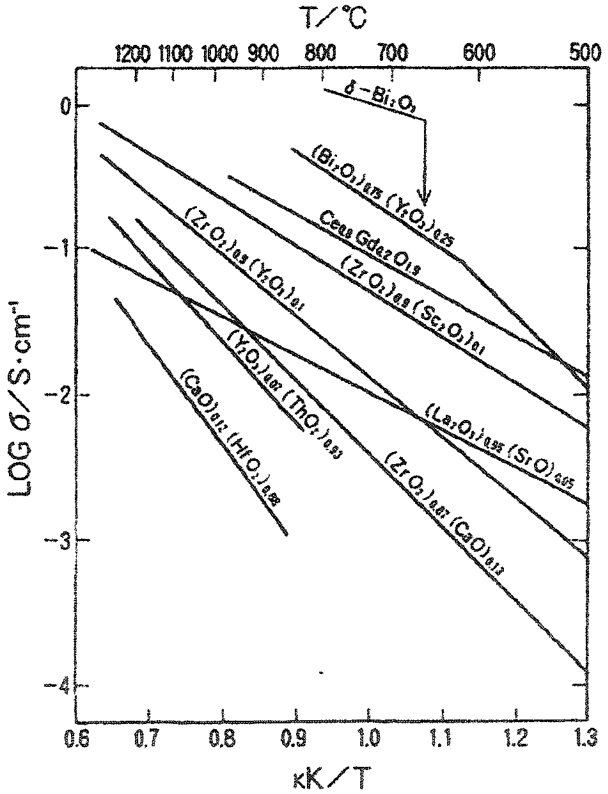

Figure 2.5 Ionic conductivity of fluorite oxides (*Inaba et al, 1996*)

It can be seen that Bi_2O_3 and yttria-stabilized Bi_2O_3 are the most ionically conductive oxides. However, these oxides are not structurally stable and are easily reduced under reducing atmospheres and therefore they are not suitable as SOFC electrolyte materials. Second after Bi_2O_3 materials are CeO_2-based electrolytes. The difficulty is now to decide which dopants and concentrations should be added to best increase the ionic conductivity of the electrolyte. The addition of too little dopant will not significantly increase the ionic conductivity and too much will induce a "hole ordering" phenomenon, which lowers the conductivity (*Bonneau, 2001*). Hole ordering results when the oxygen ions have only few paths to "jump" or "hop" within the electrolyte lattice as opposed to several paths when the holes or vacancies are randomly distributed, in which case, the oxygen ion mobility increases.

It has been almost unanimously accepted that the dopant cation radius which most closely approaches the critical lattice radius is the best dopant. This critical radius corresponds to the ionic radius of the dopant whose substitution for the host cation causes neither expansion nor contraction of the solid lattice (*Inaba et al, 1996*) (see appendix A for CeO_2 lattice structure with Ca acting as dopant). Fig. 2.6 shows that Gd^{3+} and Sm^{3+} are cations whose radii are very similar to the critical radius of M^{3+} metals (i.e. between 0.10 and 0.11 nm) and therefore Ce-based electrolytes doped with Sm or Gd present the highest conductivities, as shown below (Note that Fi.g 2.6 shows a mistake in the radius of dopant cation, i.e. the radius must be in nm)

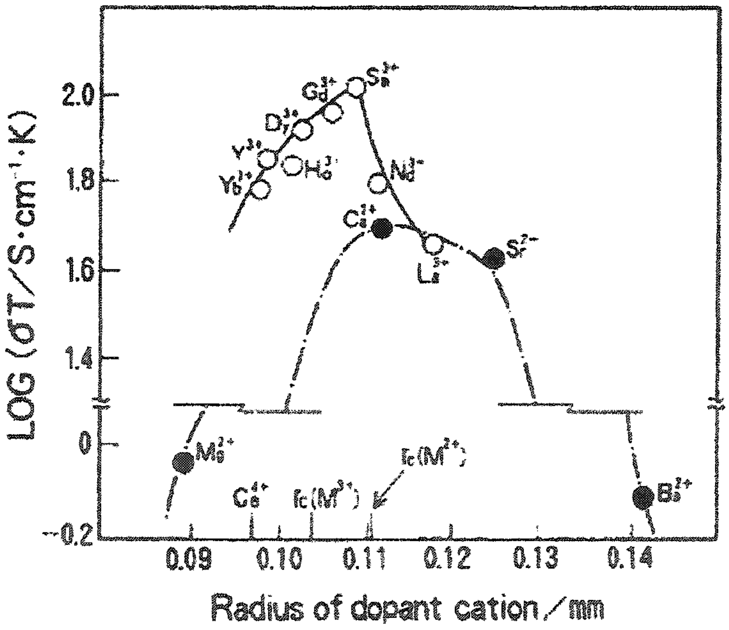

Figure 2.6 Ion conductivity of doped ceria at 1073K against the radius of dopant cation, r_c shown the horizontal axis is the critical of the divalent or trivalent cation. (*Inaba et al, 1996*)

Upon addition of either Gd or Sm, it is thought that the conduction paths within the crystal lattice become less distorted. It has also been suggested that two factors are influenced by the size of the dopant cation, which directly affect ionic conductivity, i.e. the mobility of the oxygen ions "hopping" from site to site and the bonding strength of the dopant-vacancy associates or traps typically formed at low to intermediate temperatures (*Kimpton et al, 2002*). Furthermore, it is elucidated that the substitution of larger dopants, (i.e. larger than the critical radius), into the lattice blocks the path of the migrating oxygen ions more effectively, thus increasing the ion-migration enthalpy and decreasing the ionic conductivity. For a complete description of the theory of ionic conductivity in fluorite oxides see appendix A.

Recent thermodynamic and electrical conductivity data showed that the CeO_2-$SmO_{1.5}$ and CeO_2-$GdO_{1.5}$ systems are superior ionic conductors at intermediate temperatures (~500-800 °C) than almost all of the binary zirconia-based systems (*Badwal et al, 2000*). In addition, Steele has shown that Gd^{3+} is the preferred dopant when compared to Sm^{3+} and Y^{3+} at 500 °C, in particular $Ce_{0.9}Gd_{0.1}O_{1.95}$ and $Ce_{0.8}Gd_{0.2}O_{1.9}$ are mentioned to be the best options Table 2.3 (*Steele, 2000*) (Note that σ_o is independent of temperature and is constant A in Eq. 4 in Appendix A)

Table 2.3 Ionic conductivity data for selected electrolyte compositions

Composition	Dopant	r_d (Å)	$r_d - r_c$	$r_d - r_{Ce}$	ΔE (eV)	σ_0	σ, 500°C (S cm^{-1})	σ, 600°C (S cm^{-1})	σ, 700°C (S cm^{-1})
$Ce_{0.9}Gd_{0.1}O_{1.95}$	Gd^{3+}	1.053	0.015	0.083	0.64	1.09×10^5	0.0095	00253	0.0544
$Ce_{0.9}Sm_{0.1}O_{1.95}$	Sm^{3+}	1.079	0.041	0.109	0.66	5.08×10^4	0.0033	0.0090	0.0200
$Ce_{0.887}Y_{0.113}O_{1.9435}$	Y^{3+}	1.019	−0.019	0.049	0.87	3.16×10^6	0.0087	0.0344	0.1015
$Ce_{0.8}Gd_{0.2}O_{1.9}$	Gd^{3+}	1.053	0.015	0.083	0.78	5.0×10^5	0.0053	0.0180	0.0470

It is worth noting that by co-doping with appropriate ratios of Gd^{3+}/Y^{3+} or Sm^{3+}/Y^{3+} it is possible to match the critical dopant radius exactly. Reported results for a series of co-doped compositions provided evidence that for compositions such as $Ce_{0.94}Sm_{0.04}Y_{0.02}O_{1.97}$ at 500 °C the double doping did not appear to confer any advantage (*Steele, 2000*). A recent publication by van Herle also confirms that compositions such as $Ce_{0.88}Gd_{0.04}Sm_{0.04}Y_{0.04}O_{1.94}$ have comparable conductivity at 500 °C to the values reported in Table 2.3 for the simpler $Ce_{0.9}Gd_{0.1}O_{1.95}$ (*Steele, 2000*). Therefore, double doping of the CeO_2 seemed unnecessary.

A major disadvantage associated with ceria-based systems should be mentioned. At low oxygen partial pressures the presence of significant levels of electronic conductivity due to the Ce^{4+} to Ce^{3+} reduction reaction are observed. It was demonstrated that the volume expansion associated with the Ce^{4+} to Ce^{3+} reduction reaction caused microcrack formation, which significantly decreased the ionic conductivity within the $Ce_{0.8}Gd_{0.2}O_{1.9}$ electrolyte (*Badwal, 1999*). This may be prevented by a thin layer of fully stabilized yttria-doped zirconia added to the electrolyte on the anode side (*Kimpton, 2002*).

Another significant difficulty that has restricted exploitation of Ce-Gd oxide systems at 500 °C has been the need to develop alternative cathode compositions that function effectively at lower temperatures. However, recent developments have shown that appropriate materials for composite cathodes can be fabricated with good performance (*Ralph et al, 2001*). Composite anodes such as Ni-CGO also provide adequate performance at 500 °C for simulated syngas fuels, indicating that IT-SOFC (i.e. intermediate temperature SOFC) stacks at 500 °C are now a viable option (*Steele et al, 2001*).

Another electrolyte, doped $LaGaO_3$ (LSGM), is also attracting much attention for IT-SOFC applications. Although its conductivity is slightly smaller than CGO at 500 °C, its ionic domain is wider and it could be more appropriate to use this electrolyte at temperatures around 600 °C, where the reduction of Ce^{4+} to Ce^{3+} becomes significant in CGO cells. However, it has been difficult to fabricate pure single-phase ceramic electrolytes, and second phases such as $SrLaGa_3O_7$ and $La_4Ga_2O_9$ are often detected at the grain boundaries (*Steele et al, 2001*). Further research is needed in this field.

In the following sections, only a brief account of the most significant work carried out in the anode, cathode and interconnect materials is reported, as these materials were not investigated in the present work. For a complete survey of cathode and anode materials for ceramic fuel cells, see the work by Steele (*Steele, 1996*).

2.A.4.2 Anode

In SOFCs, the fuel arriving at the anode is reducing in nature and thus metals can be used as anode materials. However, the chosen metal must not be oxidized under the operating conditions of the SOFC, in particular at the fuel outlet where the gas composition is more oxidizing. At the elevated temperatures of the SOFCs, this effectively limits the choice to nickel, cobalt and noble metals. Nickel anodes are preferred based on cost considerations.

The anode must have a porous structure, which must be maintained at the high operating temperatures. This is achieved by dispersing the nickel within the solid electrolyte material to form a cermet (usually Ni/YSZ cermet). This maintains the anode porosity by preventing the sintering of the nickel particles during operation and also gives the anode a thermal expansion coefficient comparable to that of the solid electrolyte. The anode must be electrically conductive to function as an electrode. The conductivity of the nickel/solid electrolyte cermet depends on the nickel content. The threshold for electrical conductivity is about 30 % in volume of nickel; below this level, the conductivity of the cermet is effectively that of the solid electrolyte (i.e. ionic in nature). The conductivity of the anode depends on its microstructure, in the particle size distribution of the nickel particles, and the connectivity of the nickel particles in the cermet. The thermal expansion coefficient of a nickel/yttria stabilized zirconia cermet increases linearly with the nickel content, and thus the higher the nickel content of the anode, the greater the thermal mismatch with the electrolyte. Thermal mismatch favors electrolyte cracking and anode delamination. Various means have been developed to tolerate and minimize the thermal mismatch. These include improving the fracture toughness of the electrolyte, varying the thickness and the thickness ratio of the cell components and adding minor constituents to the anode formulation. Another reason for wishing to lower the operating temperature of SOFCs is that at the higher operating temperatures sintering of the nickel particles over time is potentially a problem.

A number of researchers have studied nickel/ceria cermet anodes for ceria-gadolinia based SOFCs. These anodes have been shown to still give sufficiently good performance at temperatures as low as 500 °C (*Ormerod, 2003*). It is now believed that it will be necessary to develop a composite anode for IT-SOFC applications consisting of CGO and an electronic conducting oxide as current collector to replace the nickel. One of these anodes was copper-based and incorporated significant quantities of ceria in addition to YSZ. The development of such anodes is very active area of current research (*Ormerod, 2003*).

2.A.4.3 Cathode

The cathode must be stable in an oxidizing atmosphere and it must be electronically conductive and have a porous structure like the anode. These must be maintained at the high cell operating temperatures. Additionally, cathodes must possess a thermal expansion coefficient comparable with that of the solid electrolyte and not show any tendency to react with the electrolyte.

In the early 1970s the porous composite $La_{1-x}Sr_xMnO_3$-yttria stabilized zirconia (LSM-YSZ) electrode became established as the most appropriate to use with zirconia electrolyte fuel cells. $LaMnO_3$ is generally produced with a lanthanum deficiency to prevent formation of La_2O_3 which can cause the cathode layer to disintegrate through hydration to $La(OH)_3$. The conductivity of $La_{1-x}Sr_xMnO_3$ varies with strontium content, with an apparent optimum strontium level. Strontium doping of $LaMnO_3$ progressively increases the thermal expansion coefficient compared to undoped $LaMnO_3$, and therefore increases the mismatch with the zirconia electrolyte. In practice, two cathode layers are often employed, with the first layer being a mixture of LSM and yttria-stabilized zirconia. This improves the thermal match of the cathode with the zirconia electrolyte, and results in improved porosity and resistance to sintering. The second cathode, often called the electrical collect layer, is then pure LSM.

The development of cathodes for ceria based electrolytes was not seriously addressed until the early 1990s with the development of $La_{1-x}Sr_xCo_{1-y}Fe_yO_{3-x}$ (LSCF) materials by Anderson (*Steele, 2000*). Lanthanum ferrite cathodes are very promising alternatives that are under current investigation (*Simner et al, 2003*). Doped-$LaCoO_3$ has a superior electrical conductivity to $LaMnO_3$ under equivalent conditions as it exhibits high oxygen diffusivity, but it shows much greater reactivity towards zirconia at high temperatures (*Gödickemeier et al, 1996*). Therefore, LSC is the preferred cathode material for both ceria based electrolytes or lanthanum gallate electrolytes, operating at low temperatures (500-600 °C).

2.A.4.4 Interconnect

The interconnect is a very important component, which has two functions: first to provide the electrical contact between adjacent cells, and second to distribute the fuel to the anode and the air to the cathode. Therefore, the interconnect must posses a high electronic conductivity, be stable and impermeable in both oxidizing and reducing atmospheres and must not react with any of the other cell components.

Most groups decided to use doped $LaCrO_3$ interconnects for high temperature SOFC stacks, although the optimal composition for this component remains controversial. Unresolved issues include finding the best composition to minimize the lattice expansion associated with the loss of oxygen under anodic conditions and increasing thermodynamic stability of SrO and CaO doped $LaCrO_3$. Thermodynamic stability becomes an issue at the CO_2 partial pressures generated in the anode at large fuel conversion levels. Westinghouse initially overcame many of these problems by using an electrochemical vapor deposited (EVD) MgO doped $LaCrO_3$ interconnect. Recently, this interconnect has been changed to CaO doped $LaCrO_3$ to facilitate a cheaper processing route.

For SOFCs operating in the intermediate temperature range, 500 to 700 °C, it becomes feasible to use certain ferritic stainless steel composites which fulfill the necessary criteria as SOFC interconnects. The use of metallic interconnects offers very substantial cost benefits compared to $LaCrO_3$, but their use is presently precluded in SOFCs operating at higher temperatures. For a complete review of the current interconnect materials used in SOFC see the work by Quadakkers (*Quadakkers et al, 2003*)

2. B Nature and composition of electrolyte powders and their material precursors

2.B.1 Nature and composition of electrolyte powders

Doped-CeO_2 based powders emerged as the most promising alternatives as electrolyte materials according to the literature review (see previous section). Three dopants were chosen: samarium (Sm), gadolinium (Gd) and yttrium (Y). The amount of dopant added to the CeO_2 was selected to maximize the ionic conductivity of the doped electrolyte powders.

Fig. 2.7 shows that the amount of Sm dopant added to CeO_2 that maximized the conductivity had a range that was dependent on temperature. It appeared that the higher the temperature, the broader the range and the flatter the maximum. At lower temperatures, i.e. at 500 °C, the maximum ionic conductivity of Sm-doped-CeO_2 occurred in the range of x=0.1-0.2 and was comparable with that of doped CaO-ZrO_2, a conventionally used electrolyte material. The ionic conductivity of the $Ce_{1-x}Gd_xO_{2-x/2}$ mixture was also examined at 500 °C by Steele (*Steele, 2000*) and it is shown in Fig. 2.8. He found that the ionic, bulk or lattice conductivity of the $Ce_{1-x}Gd_xO_{2-x/2}$ mixture presented a maximum in the 10% mol vicinity (i.e. x = 0.1) and that maximizing the total material conductivity would lead to an erroneous result. This was because the total material conductivity was dominated by the grain boundary conductivity of the oxide and the bulk (not the total conductivity) has to be maximized[*] for an optimum SOFC electrolyte operation This is why a composition of dopant of 10 % mol is preferred over 25 % mol $GdO_{1.5}$.

Ytrium was also included as a possible dopant mainly as a result of its wide use as an electrolyte component. It has been known for many years that the dopant concentration that maximizes the bulk ionic conductivity lies in the 4 to 8 % mol range of Y_2O_3 oxide (i.e. $Ce_{0.92}Y_{0.08}O_{1.96}$ to $Ce_{0.84}Y_{0.16}O_{1.92}$). In particular a 6 % mol of yttrium oxide has been reported to give maximum lattice conductivity (*Tian et al, 2000*). This is further illustrated in Fig. 2.9 in which the lattice and grain conductivities are shown at two different temperatures.

---

[*] This difference in conductivities between grain boundaries and bulk is a result of grain boundary defects and SiO_2 impurities that significantly decrease the total material conductivity. The distinction between the lattice and grain boundary conductivities is possible thanks to both a technique called impedance spectroscopy (*MacDonald, 1987*), and the use of a model that represents the lattice, grain boundary and electrode contributions as equivalent electrical circuits (*Bauerle, 1969*)

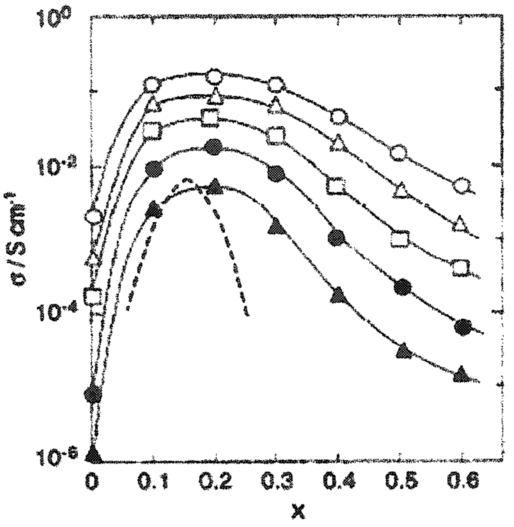

Figure 2.7 Composition dependence of conductivities for $(CeO_2)_{1-x}(SmO_{1.5})_x$, ○ 900 °C, Δ 800 °C, □ 700 °C, • 600 °C, ▲ 500 °C, broken line $(ZrO_2)_{1-x}(CaO)_x$ at 800 °C (*Eguchi, 1997*)

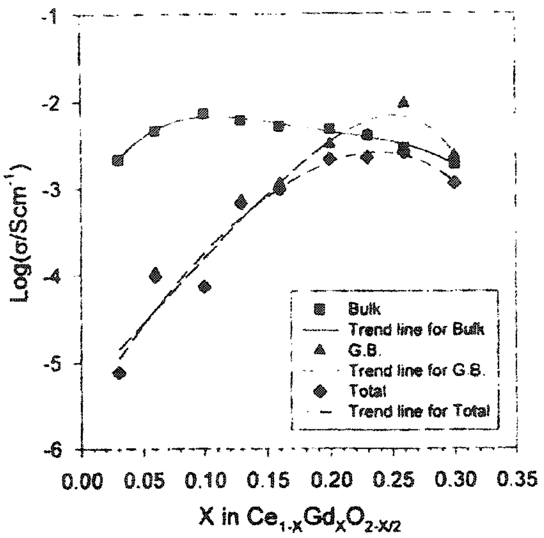

Figure 2.8 Isothermal conductivity of $Ce_{1-x}Gd_xO_{2-x/2}$ at 500 °C as a function of Gd concentration showing data for the lattice conductivity, grain boundary and total contributions (*Steele, 2000*)

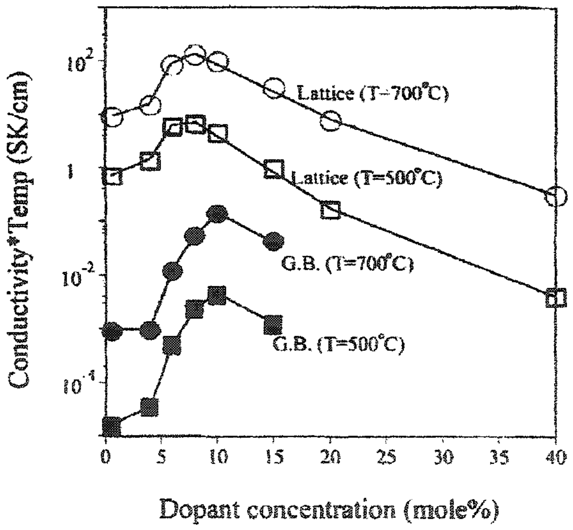

Figure 2.9 Lattice and grain boundary conductivities at 500 °C and 700 °C for Y-doped CeO_2 samples (*Tian et al, 2000*)

2.B.2 Nature and behavior of electrolyte material precursors

2.B.2.1 Type of feeding

To introduce the dopants (Sm, Gd and Y) and the cerium three possibilities were considered, i.e. solid, solution or suspension feeding. A suspension is defined as a mixture in which small solid or liquid particles are suspended in liquid or gas (Dictionary of Physics). The term suspension in this work refers to a mixture of small solid particles in liquid media.

There are several advantages in using liquid precursors. First, the rate and the composition of material introduced to the plasma can be more easily and accurately controlled with solutions than with solids or suspensions. The composition of the solutions can be accurately adjusted by properly weighing the solid materials prior to dissolution. Suspensions tend to clog the tubing through which they are fed into the plasma torch due to particle accumulation brought about by liquid evaporation and poor flowability. Thus controlling their compositions becomes problematic. Second, homogeneity is better achieved in solutions than in suspensions even if dispersant agents are used to stabilize the suspension. This is because homogeneity is an inherent property of solutions. Further, in the case of suspensions, apart from the initial mixing required to suspend the solids, mixing must be maintained while the suspension is being fed further complicating the feeding process. Solid particles have different size, shape and density, thus it is difficult to have a "uniform" and/or a "constant" solid feeding. If solid metals or metal oxides were to be introduced, particle fusion rather than particle reaction would govern the mechanism of doped oxide formation (*Bonneau et al, 2001*).

The only drawback of solution injection is the undesired amount of solvent (water being the most common) introduced to the plasma. This reduces the amount of energy available for reaction and melting of the synthesized particles. Despite this drawback, solutions were preferred, chiefly to their homogeneity, ease of preparation and handle.

2.B.2.2 Evaluation of different liquid precursors

Chlorides, nitrates, hydroxides, oxalates and organic salts have all been employed in the production of oxides from liquid precursors. Chlorides (*Bonneau, 2001; Jurewiczs et al, 2003; Lemoine et al, 2003*) and nitrates (*Schiller et al, 2003*) have yielded acceptable results. In her work, Bonneau reported very similar reaction mechanisms for the formation of ZrO_2 from both hydroxides and chlorides. She also used nitrate salts of Ce, Y and La to prepare $Ce_{0.8}La_{0.1}Y_{0.1}O_x$ but no reaction mechanism was reported. The main drawback of employing either chlorides or hydroxides was the formation of hydrochloric acid, which is highly toxic and very corrosive. Conversely, nitrates promote the formation of NO_x which is comparatively less harmful than HCl.

Oxalates due to their carbon content contaminate oxides and favor undesired side reactions (*Mosse et al, 1995*). Organic salts could be used but they are considerably more expensive than nitrates and chlorides. Further, nitrates are readily soluble in water, reducing the time required to prepare a solution. They are also the cheapest salts.

2.B.2.3 Description of calcinations mechanisms of precursors

The decomposition of different rare-earth salts was first investigated by Wendlandt. He analyzed the pyrolisis of a wide spectrum of rare-earth chloride and nitrate salts in air, including Ce, Gd, Sm and Y salts (*Wedlandt et al, 1956, 1957, 1959 and 1960*). It was found that the thermal decomposition of the lighter rare earth metal chlorides and nitrates followed a general and very similar pattern with the notable exception of Ce and Sc. The general decomposition patterns are given below (M=Y, Sm, Gd).

$$MCl_3 \cdot 6H_2O \rightarrow MCl_3 \cdot nH_2O \rightarrow MCl_3 \rightarrow MOCl \rightarrow M_2O_3 \qquad (1)$$

$$M(NO_3)_3 \cdot 6H_2O \rightarrow M(NO_3)_3 \cdot nH_2O \rightarrow M(NO_3)_3 \rightarrow MONO_3 \rightarrow M_2O_3 \qquad (2)$$

In the case of Ce, neither a basic nitrate intermediate ($CeONO_3$), nor a basic oxy-chloride intermediate ($CeOCl$) was found, and CeO_2 was obtained instead. This is of particular interest because the electrolyte powders produced were composed mainly of CeO_2, and this oxide can be formed at temperatures starting at 450 °C from nitrates (curve 2 in Fig 2.10a) and beginning at 550 °C (curve D in Fig. 2.10b) from chlorides. This finding is of particular importance as CeO_2 can be produced in a plasma environment at a temperature of 100 °C lower than that required for chlorides, and thus more energy could be available for particle melting after calcination. This confirmed that nitrates were more favorable than chlorides as starting materials

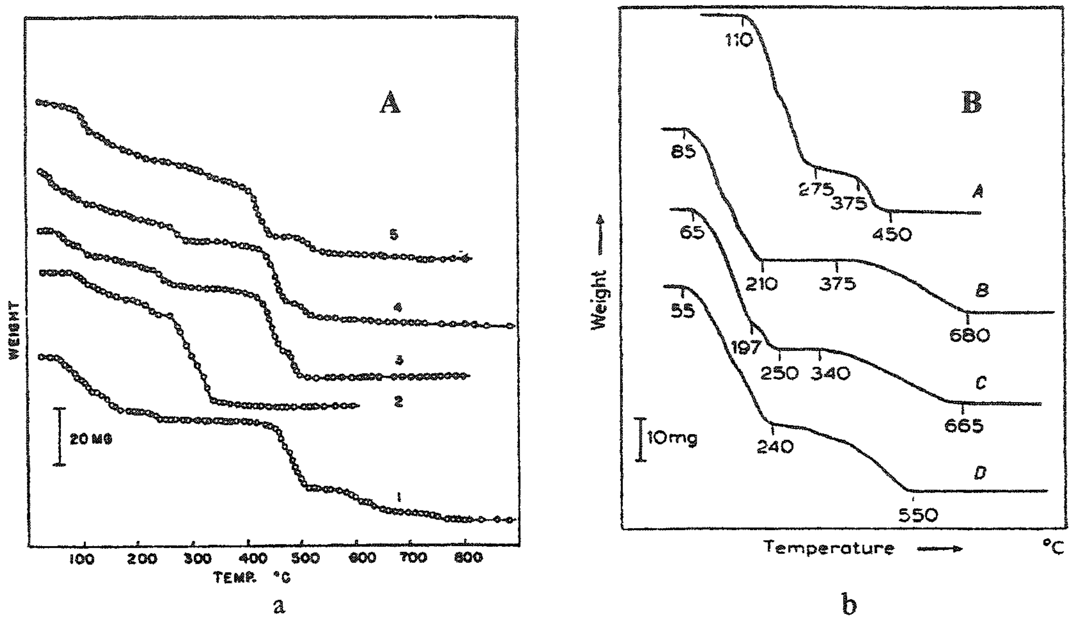

Figure 2.10 a) Thermolysis curves of selected rare earth nitrates, 1) La(NO_3).6H_2O, 2) Ce(NO_3).6H_2O, 3) Pr(NO_3).6H_2O, 4) Nd(NO_3).6H_2O, 5) Sm(NO_3).6H_2O, (Wendlandt, 1956) ; b) Thermolysis curves of selected rare earth chlorides A) YCl_3.6H_2O, B) $LaCl_3$.6H_2O, C) $PrCl_3$.6H_2O, D) $CeCl_3$.6H_2O, (Wendlandt, 1957)

Since nitrate salts for all the rare-earth metals were employed, a summary of the thermal decomposition of the dopant salts is now given.

Table 2.4 Summary of the thermal decomposition of the dopants used (M=Y, Sm, Gd) (Wendland, 1956 & 1957)

Metal	$M(NO_3)_3$ .6H_2O	→	$M(NO_3)_3$. nH_2O	→	$M(NO_3)_3$	→	$MONO_3$	→	M_2O_3
Y (°C)	25		30		Not stable		440 – 475		660 (begin)
Sm (°C)	25		50		Not stable		450 - 490		750 (begin)
Gd (°C)	25		Not stable		75		455 - 480		730 (begin)

A detailed study of the thermolysis of Ce(NO_3)$_3$.6H_2O confirmed the findings described by Wendlandt and proposed a new mechanism for the loss of waters of hydration (*El-Adham et al, 1977*). The abnormal calcination mechanism of cerium nitrate has also been observed by other authors (*Karppinen et al, 1989*), but its mechanism remained obscured. Recent findings have suggested that the thermal decomposition of nitrate salts may be initiated through dissociation of the N-O bond. It was reported that the nitrate decomposition temperature was inversely proportional to the charge density of the metal ions. High density metal ions can polarize nitrate ions and induce a sort of covalence bond between M and O and, as a result, favor the nitrate decomposition. Ce(NO_3)$_3$ has a charge density of 0.66 x 10^{-3} (e/nm^3) compared to Gd(NO$_3$)$_3$ that has 0.57 x 10^{-3} (e/nm). Therefore, cerium nitrate has a starting decomposition temperature of ~300 °C and gadolinium nitrate shows decomposition beginning at ~370 °C. Data for samarium and yttrium were not reported but since those dopants had showed thermolysis curves similar to that of gadolinium, it was expected that they would also decompose at higher temperatures than the decomposition temperature of cerium nitrate.

2. C Plasma processing of materials

2.C.1 Thermal plasmas

Thermal plasma technology has evolved over the past decade into an advanced interdisciplinary science. Its principal applications are in materials processing, including extractive metallurgy, melting and refining or metals and alloys, plasma chemical synthesis, plasma chemical vapor deposition, plasma and arc spraying, plasma waste destruction, and plasma synthesis of advanced ceramics. Plasma synthesis of fine particles down to the nanometer size range is one of the recent plasma applications, and it is still in its early stage of development (*Boulos et al, 1994*).

The high energy-density combined with the high temperature of thermal plasmas leads to high reactivity and to material heating and quenching rates in the order of 10^5-10^7 K/s. Moreover, the fact that the energy is generated through electrical coupling into the plasma and not through a combustion process also provides the additional means for the independent control of the chemistry of the reaction mixtures and its specific energy level. These are unique and important features of thermal plasma processing which allow the rapid synthesis of materials with unique and enhanced properties at high temperatures (*Boulos, 1991*).

2.C.2 RF (radio frequency) inductively coupled discharges

An RF-inductively coupled discharge was used in this project, among the different ways to generate plasmas. In RF-induction plasma torches, energy coupling to the plasma is accomplished through the electromagnetic field of the induction coil. The plasma gas does not come into contact with electrodes, thus eliminating possible sources of contamination and allowing for the operation of such plasma torches with a wide range of gases, including inert, reducing, oxidizing and other corrosive atmospheres. Pure argon or its mixture with other gases is still the usual choice as the plasma gas largely because of its ease of ionization. The excitation frequency is typically between 200 kHz and 20 MHz. Laboratory units run at power levels of the order of 30-50 kW. In addition, induction plasmas are characterized by their large volume, low velocity and high energy density, and by their ability to offer injected particles a relatively long in-flight heating time of the order of 10 to 35 ms (compared to 0.5 to 1.0 ms in the DC plasma spraying units) (*Boulos, 1992*). The relatively low radial thermal and velocity gradients in the plasma core (in comparison to the steep axial gradients) ensure a relative homogeneous treatment of a high reactant throughput injected in the central region of the plasma (*Bouyer et al, 2001*).

The plasma torch is composed, as shown in Fig. 2.11, of a water cooled confinement tube, typically, 35 to 70 mm in internal diameter and 150 to 200 mm long, for plasma torches with a nominal power rating in the range of 30 to 150 kW, respectively.

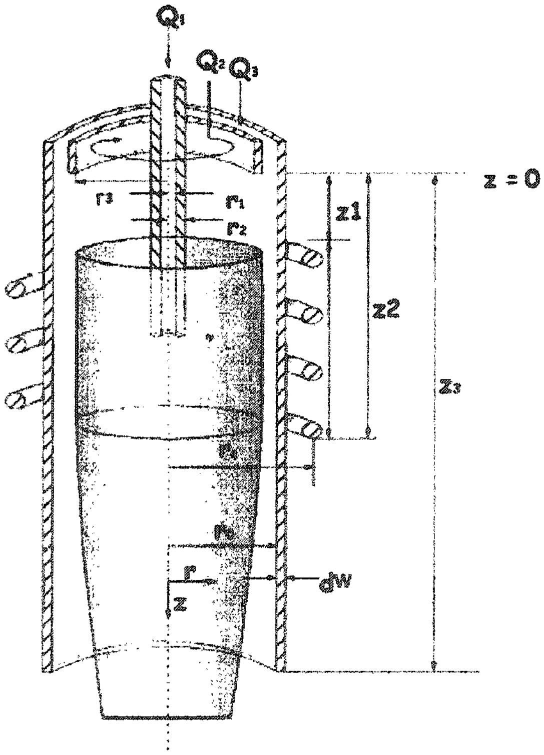

Figure 2.11 Schematic diagram of the induction plasma torch (Tekna PL-35 torch) (*Merkhouf et al, 2000*)

The confinement tube is surrounded by a three to five turn induction coil connected to the RF power supply. The coil is water-cooled with a rigid configuration to maintain a constant impedance matching to the power supply and to ensure optimum energy transfer. The upstream part of the torch is the gas distributor head, which is responsible for the introduction of the different gases. Three different gas streams are introduced into the torch. The sheath gas (Q_3) serves to protect the wall of the plasma confinement tube from the high temperature of the discharge and sometimes to favor the oxidation or reduction of the chemical species injected into the plasma (using either oxygen or hydrogen). The central gas (Q_2), which has a swirl velocity component, serves to stabilize the plasma. The powder or atomizing gas (Q_1) serves as a carrier for the axial injection of the powder or as an atomizing gas. A water-cooled stainless steel probe, which penetrates through the torch head, is used to introduce the powder, suspension or solution axially into the center of the discharge. Due to the complexity of the flow pattern in the discharge region, the position of the tip of the powder injection probe is of critical importance. If located above the first turn of the coil, it could result in the excessive deposition of the powder on the wall of the plasma confinement tube in the case of powder injection. In the case of suspension or solutions injection, it could result as possible recirculation and/or backflow of the atomized droplets. A low probe position will result in excessive cooling of the plasma and a reduction of the particle residence time in the discharge. This will give rise to a reduction of the ability of the plasma to completely melt the particles in-flight. A more detailed and technical description of the plasma system is provided in chapter 3, in which the experimental apparatus is described

2.C.3 Thermal plasma synthesis of ceramics

Thermal plasma methods applied to ceramics began with the experiments conducted by Gilman (*Gilman et al, 1968*). He reported that stoichiometric CeO_2 particles were spheroidized by an inductively coupled plasma torch. However, the use of thermal plasma to synthesized oxide particles from liquid precursors was first developed in the early 90s. Fine powders of $YBa_2Cu_3O_{7-x}$ were synthesized by injecting mixed nitrate solutions of yttrium, barium and copper into an argon RF thermal plasma (*Zhu et al, 1990*). The use of thermal plasma to produce powders of different compositions was also successfully demonstrated for nanosized zinc ferrite spinel powders. Various compositions were recently produced in a

RF thermal plasma from co-precipated hydroxides (*Mohai et al, 2001*). The plasma chemical treatment of salts and their aqueous solutions was reported as a very promising alternative to synthesized rare-earth oxides by Mosse (*Mosse et al, 1995*). He studied, numerically and experimentally, the production of oxides of rare-earth elements from dispersed aqueous salt solutions in an electric arc plasma reactor. The use of a suspension instead of a solution to produce oxide particles was first applied to the production of hydroxyapatite (*Bouyer et al, 1997*). This technique has also been employed to prepare yttria-stabilized zirconia and Al_2O_3 coatings (*Delbos et al, 2003*) and to produce $LaMnO_3$ perovskite coatings (*Monterrubio et al, 2003*) using DC thermal plasma.

2. D Conventional and plasma applications for the production of SOFC components

The real disadvantage in the production of SOFC components using conventional methods is the great number of steps involved, and thus the overall process becomes expensive, time consuming and prone to contamination. This has promoted the investigation of alternative processes. The aim of these processes is to allow the synthesis and deposition of SOFC components starting from suitable precursors (mostly liquid due to their ease of injection and facility to control their composition) in one step. These alternatives are chemical vapor deposition (CVD), electrochemical vapor deposition (EVD), and aerosol assisted metal-organic CVD (MOCVD) (*Song et al, 2003*). Both radio frequency and direct current thermal plasmas have been successfully applied to synthesize oxides and deposit ceramic coatings. The first attempts to produce SOFC components using thermal plasmas emerged as a consequence of this success. In recent years, it has been demonstrated that both RF-inductively coupled and DC thermal plasma could be implemented to prepare SOFC components. The conventional methods for the production of SOFC components are reviewed before describing the advances of RF thermal plasma in the production of these components.

2.D.1 Conventional methods for the production of SOFC components

In general, the production of cell components using conventional methods is divided into three stages. The first one involves the production of cathode, anode and electrolyte materials of adequate compositions usually in the form of powders. The second stage is the formation of the solid layers of each of the components, and finally the third stage is the assembly of all the components in a single cell unit.

Several methods have been employed in the production of the powder materials to be converted in SOFC components. The Pechini method has been extensively used to manufacture ceramic oxide powders for SOFCs (*Cüneyt et al, 2000*). It involves the formation of a polymeric resin, using citric acid and ethylene glycol at ~150 °C, from solutions (usually nitrates) of the desired metals. This resin upon constant heating forms a char. As the temperature is increased, the char undergoes calcination and the oxide powders are formed. The process involves a minimum of 10 hours. Despite its length, gadolinium doped cerium electrolyte and perovskite-type cathode powders have been synthesized using the Pechini method with good results (*Doshi et al, 1999*). Tsoga investigated several techniques to synthesize pure crystalline gadolinium doped cerium (GDC) powders, i.e. urea-nitrate combustion, spray-drying, and two strike co-precipitation methods using ammonia or oxalic acid, among these, the strike co-precipitation with oxalic acid was reported as the best alternative (*Tsoga et al, 1999*). The common denominator in the Tsoga study was the long time involved to produce the powders as a result of the sintering and calcinations processes. Recently, two ceramic powders were synthesized at several dopant compositions by the oxalate coprecipitation route using cerium nitrate and gadolinium or samarium nitrate as starting materials with good results (*Zha et al, 20003*). Solid state reactions with solid powders have also been tried. CeO_2 and Y_2O_3 powders were mixed and ballmilled with methanol as solvent to produce $(YO_{1.5})_x$ $(CeO_2)_{1-x}$ powders (*Xiong et al, 2001*). $Zr_{0.75}Ce_{0.08}M_{0.17}O_{1.92}$ (M=Nd, Sm, Gd, Dy, Ho, Y, Yb, Sc) powders were also prepared by solid state techniques. Milling of the solid materials in propan-2-ol was reported (*Kimpton et al, 2002*).

Regarding the second stage of SOFC production (i.e. the formation of solid electrolyte layers), conventional ceramic processing methods are usually involved, such as tape casting, screen printing and slurry coating. A typical case is the production of the anode supported electrolytes, which is manufactured using tape casting followed by sintering to improve the anode-electrolyte contact. Cathodes are usually applied to the anode-supported electrolyte by either slurry painting or screen printing followed by another heat treatment to ensure a proper contact between the electrolyte and the cathode. Other alternative methods commonly involved in the production of SOFCs are conventional ceramic techniques such as warm pressing, vacuum slip casting, wet powder spraying, and screen printing (*IWV, 2003*). These tedious processes for SOFC production provide a cheap alternative to manufacture SOFC components but have certain difficulties in obtaining fully dense thin films during the removal of undesired compounds and during sintering.

2.D.2 Plasma methods for the production of SOFC components

Thermal spray methods have been applied to the production of SOFC components for more than 10 years: to make SOFC cathodes by the plasma spraying of perovskite powders (*Schiller et al, 1999*); to produce dense zirconia electrolyte layers with the aid of Laval-type nozzles to accelerate the plasma flow (*Müller et al, 2002*), and to fabricate porosity-controlled Ni/YSZ cermet thick anode layers (*Lemoine et al, 2003*). Thermal-plasma technology, especially, plasma spraying, offers several advantages, the most important of which is the ability to achieve considerably higher deposition rates than those that can be obtained with such approaches as physical or chemical vapor deposition (PVD or CVD). The other advantages are the reduction of the production cost for the present technology used in the manufacture of SOFCs (i.e. series of sintering processes) and the possibility for decreasing the thickness of the electrolyte oxygen-ion conducting layer, which in turn reduces the internal electrical resistance of the cell (*Gitzhofer et al, 2000*). Further, the plasma produced SOFC layers require no further thermal post-treatment after deposition (*Schiller et al, 2003*).

Thermal plasma chemical vapor deposition (TPCVD) has been employed to deposit Sr-doped La-(Mn, Fe, Co) perovskite cathodes with better results than suspension plasma spraying (SPS). This was because the thermal plasma chemical vapor deposited layers had the open porosity required for gas migration in SOFC electrodes, whereas the suspension plasma sprayed layers had a very low porosity. The difference in porosity was a consequence of the different microstructure provided by the two different methods. SPS favored a layered microstructure and TPCVD favored a columnar microstructure (*Müller et al, 2002*). Deposition rates of up to 25 μm/min were achieved with TPCVD which are orders of magnitude higher than most of the comparable values found in the literature for TPCVD of oxide layers (*Schiller, 2003*).

Suspension plasma spraying has been applied to the production of the YSZ and CeO_2 electrolytes (*Bonneau, 2001; Gutierrez et al, 2001*) with excellent results. Bonneau surveyed several liquid precursors and found that nitrate and chloride solutions were promising alternatives. It was also noticed that the suspension stability depended on the particle size, viscosity, homogeneity, mass-liquid ratio and type of solvent. The final suspension must contain as many solid particles as possible and yet it must have a sufficiently low viscosity to avoid particle clogging. Yttria stabilized zirconia layers of 12% mass Y_2O_3 have been deposited at rates in excess of 100 µm/min. This was as efficient as most of the traditional thermal spraying methods, and dense coatings with only 3% porosity could be achieved (*Müller et al, 2002*). Finally, there has been a worldwide effort devoted to the production of SOFC components using different thermal plasma techniques to prepare the gas-tight, solid electrolyte yttria stabilized zirconia layer, the porosity controlled Ni/YSZ cermet thick anode layer and also the porosity controlled perovskite cathode. The techniques investigated were DC/RF-hybrid plasma spraying, RF-induction plasma spraying with and without supersonic nozzle, triple torch plasma spraying, and high-velocity-low-pressure DC plasma spraying. The results obtained clearly showed that SOFC components produced using thermal plasma technology performed among the highest SOFCs performance values reported for SOFC components manufactured employing conventional ceramic methods (*Gitzhofer, 2000*).

Chapter 3 Experimental techniques and methodology

3. A Experimental setup

The experimental setup used in this project has been successfully employed in the production of several materials; notable cases are the production of hydroxyapatite (*Bouyer et al, 1997*), and $MoSi_2$ (*Gutierrez et al, 2001*) and SiC nanopowders (*Guo et al, 1997*).

3.A.1 Description

The complete experimental setup consists of an induction plasma torch (PL-50 Tekna Inc.), a 50 kW radio frequency power supply (Lepel generator with an oscillator frequency 3-5 MHz), two cylindrical stainless steel hermetically sealed water-cooled reactors, i.e. primary and secondary, three parallel 5 μm porous metallic filters (Inconel 600), and an atomizing probe (Tekna Inc. SA-792 x 0.8/1.0 mm. in internal diameter x 260 mm long). The tip of the atomizing probe was located just below the first induction coil of the torch. The experimental setup is shown schematically in Fig. 3.1.

3.A.2 Operation

The procedure followed to synthesize all samples was the following. The primary and secondary reactors were water-washed before running any experiment. The system was mounted as shown in Fig. 3.1 and the vacuum started. To ignite the plasma, a pressure reading of ~10 torr (vacuum) should be obtained, but on occasion the vacuum desired was not achieved and the plasma was started at pressures below 30 torr but higher than 10 torr. The plasma must never be ignited if the pressure reading is higher than 50 torr which indicates major leaks in the system. The central gas (10 slpm Ar) and the sheath gas (45 slpm Ar) were used to ignite the plasma once the radio frequency power was turned on. The atomizing gas was then allowed to flow into the torch. The pressure was slowly increased to 200 torr and then the oxygen sheath gas was fed to the torch at the same time that the argon sheath gas flow was stopped. The reactor pressure and the atomizing, central and sheath gas flow rates were finely adjusted to the desired experimental conditions. Finally, the peristaltic pump was turned on and the precursor solution was fed to the plasma torch. The gas flow rates were stopped ~20 seconds after the feeding solution was depleted. This was done with the intention of completely reacting left over solution in the feeding line. The particles were collected from different places, i.e. the reactors walls, the collector at the bottom of the primary reactor and at the metallic filters. A brush was used to remove the particles from the filters and the reactors walls.

Figure 3.1 Experimental setup

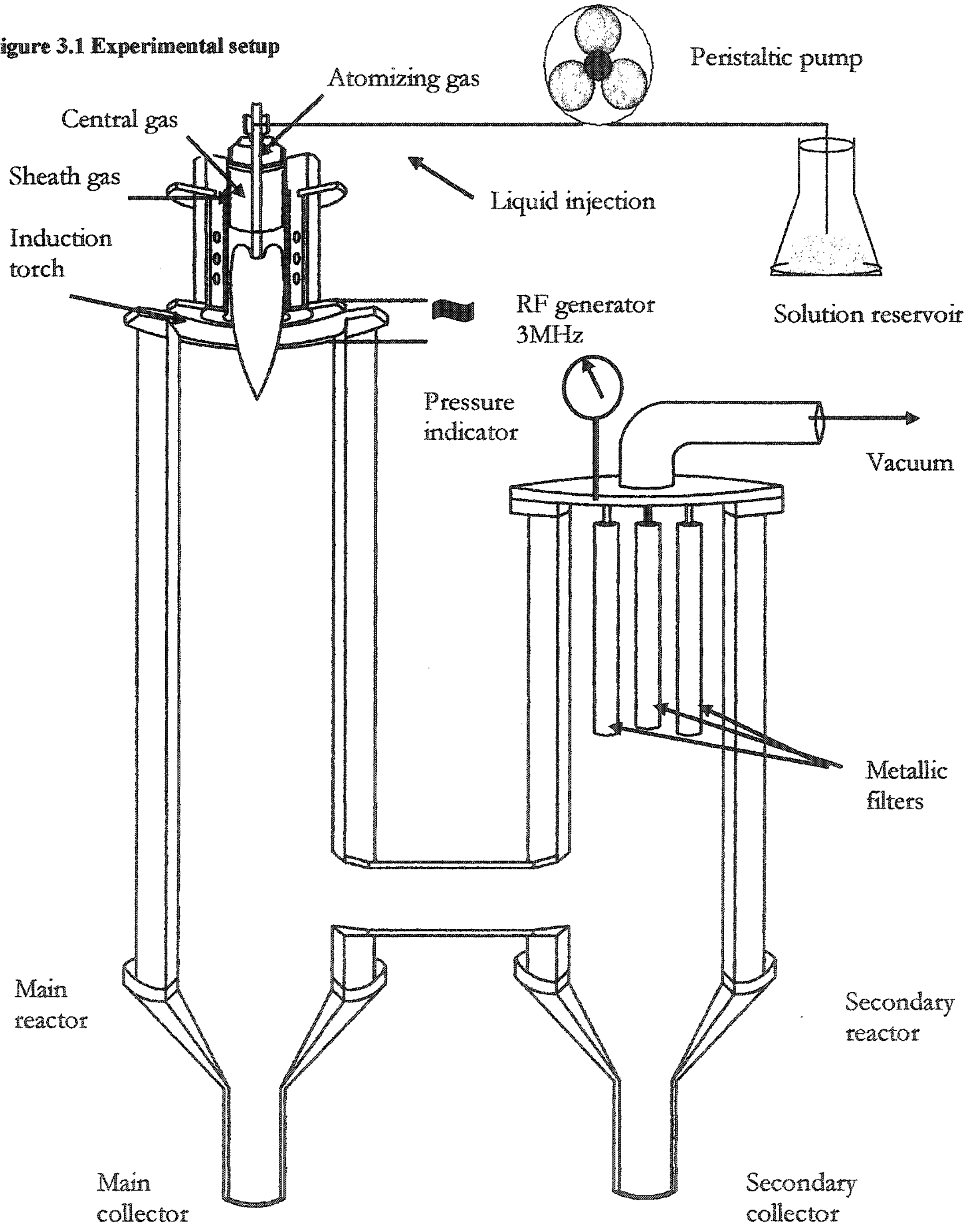

3.A.3 Recompilation of experimental conditions

The experimental conditions are shown in Tables 3.1 and 3.2. The atomization gas flow rate showed slight fluctuations (± 0.5 slpm) during operation but they did not significantly affect the experiments. These fluctuations resulted from small leaks along the atomizing gas line as a result of constant disassembly of the equipment for cleaning purposes. Also, different atomizing gas flow rates resulted in different droplet distributions with minor variations of the order of 3 microns between the lowest and the highest flow rate, 5.0 and 6.5 slpm respectively. The central and sheath gas used were argon and oxygen respectively.

Table 3.1 Summary of experimental conditions

No	Synthesized product	DC voltage *[kV]*	Current *[A]*	Plate power *[kW]*	Central gas *[slpm]*	Sheath gas *[slpm]*	Atomizing gas *[slpm]*	Liquid flow rate *[ml/min]*	Probe aperture *[degrees]*	Reactor pressure *[torr]*
1	$Ce_{0.8}Gd_{0.2}O_{1.9}$	6.3	5.5	35.0	9.5	39.0	6.560.5	6.0	270° (open)	300610
2	$Ce_{0.85}Gd_{0.15}O_{1.925}$	6.2	4.2	26.0	31.0	39.0	5.060.5	6.0	270° (open)	300610
3	$Ce_{0.9}Gd_{0.1}O_{1.95}$	6.0	5.0	30.0	9.5	39.0	6.560.5	6.0	270° (open)	300610
4	$Ce_{0.8}Sm_{0.2}O_{1.9}$	5.0	3.0	15.0	9.5	39.0	5.060.5	6.0	270° (open)	300610
5	$Ce_{0.85}Sm_{0.15}O_{1.925}$	6.0	4.0	24.0	9.5	39.0	5.060.5	6.0	270° (open)	300610
6	$Ce_{0.9}Sm_{0.1}O_{1.95}$	6.2	5.5	34.1	9.5	39.0	6.560.5	6.0	270° (open)	300610
7	$Ce_{0.85}Y_{0.15}O_{1.925}$	6.0	4.0	24.0	9.5	39.0	5.060.5	6.0	270° (open)	100610
8	$Ce_{0.88}Y_{0.12}O_{1.94}$	6.0	5.0	30.0	9.5	39.0	6.560.5	6.0	270° (open)	300610
9	CeO_2	6.2	4.2	26.0	9.5	39.0	5.560.5	6.0	270° (open)	300610

Table 3.2 Summary of solution preparation

No	Synthesized product	Precursors		Precursors		Water added	Density of the solution
			[g]		*[g]*	*[g]*	*[g/ml] @25℃*
1	$Ce_{0.8}Gd_{0.2}O_{1.9}$	$Ce(NO_3)_3.6H_2O$	41.84	$Gd(NO_3)_3.6H_2O$	10.87	30.49	1.583
2	$Ce_{0.85}Gd_{0.15}O_{1.925}$	$Ce(NO_3)_3.6H_2O$	20.92	$Gd(NO_3)_3.6H_2O$	3.84	14.18	1.657
3	$Ce_{0.9}Gd_{0.1}O_{1.95}$	$Ce(NO_3)_3.6H_2O$	41.84	$Gd(NO_3)_3.6H_2O$	4.83	23.46	1.603
4	$Ce_{0.8}Sm_{0.2}O_{1.9}$	$Ce(NO_3)_3.6H_2O$	20.92	$Sm(NO_3)_3.6H_2O$	5.35	15.19	1.637
5	$Ce_{0.85}Sm_{0.15}O_{1.925}$	$Ce(NO_3)_3.6H_2O$	41.84	$Sm(NO_3)_3.6H_2O$	7.56	28.28	1.616
6	$Ce_{0.9}Sm_{0.1}O_{1.95}$	$Ce(NO_3)_3.6H_2O$	41.84	$Sm(NO_3)_3.6H_2O$	4.76	26.42	1.616
7	$Ce_{0.85}Y_{0.15}O_{1.925}$	$Ce(NO_3)_3.6H_2O$	20.92	$Y(NO_3)_3.6H_2O$	3.21	13.76	1.624
8	$Ce_{0.88}Y_{0.12}O_{1.94}$	$Ce(NO_3)_3.6H_2O$	41.84	$Y(NO_3)_3.6H_2O$	4.70	26.38	1.600
9	CeO_2	$Ce(NO_3)_3.6H_2O$	20.92	-	-	11.62	1.666

$Ce(NO_3)_3.6H_2O$, $Y(NO_3)_3.6H_2O$, $Gd(NO_3)_3.6H_2O$, and $Sm(NO_3)_3.6H_2O$ (from Alfa Aesar, stock No. 11330, 12898, 12917 and 12906, respectively)

3. B Electrolyte powder production and characterization

The different techniques and methodologies that were employed for the particle production and analysis were the following.

3.B.1 Atomized droplet size distribution

The atomized droplet size distribution (DSD) was measured using a Malvern/INSITEC In-Line EPCS (Ensemble Particle Concentration and Size) system. This system is designed to continuously measure and display particle size distribution information from a pneumatically conveyed stream of powders or aerosols. The EPCS uses the laser diffraction technique to measure the particle or droplet size distribution. A general system layout is shown in Fig. 3.2.

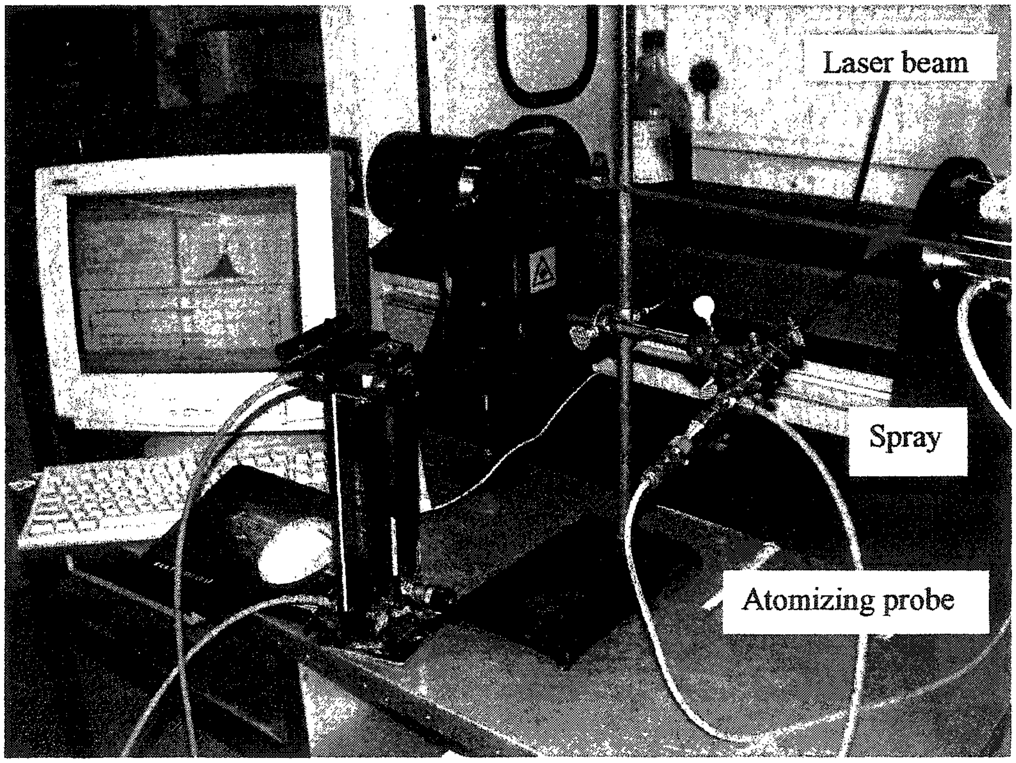

Figure 3.2 Malvern atomized droplet size analyzer setup showing a different probe than the one used in this work (Courtesy of Linda Oukacine)

The gas flow rate was controlled using a calibrated rotameter (see appendix B). A peristaltic pump (Peristaltic Pump Easy Load II. Masterflex) was used (not shown in Fig.

3.2) to inject the liquid into the atomizing probe (see appendix B for calibration curve). The optimum distance between the probe nozzle and the laser beam was 3.0 cm. The atomized spray was located 4-5 cm away from the detector mirror. These parameters were chosen based on the real time droplet size distribution displayed by the computer. The spray must intercept the laser beam in such a way that bimodal DSD were not recorded by the computer. Bimodal distributions arose because the laser detector mirror was unclean or because the spray intercepted the laser beam either too close or too far away from the optimum position. Great care must be taken to prevent atomized droplets from contacting the detector mirror as this could easily change the DSD curve. If this happens, the data acquisition must be stopped, the mirror cleaned and the system re-started.

3.B.2 X-Ray diffraction

The X-Ray diffraction analysis was done using a PHILIPS PW1710 Powder X-ray diffraction system. The Philips PC APD and Philips PC Identify software were used with this system. The system is equipped with a fine focus copper x-ray source, operated at 800 Watts.

Prior to analysis, all samples were air dried. Each sample is then tightly packed into the sample holder (a sample volume of about 5 ml is required) and exposed to X-ray radiation. A detector attached to the system measures the intensity of diffracted rays at different angles. The information is reported in a graph of diffracted angles (2θ) versus intensities and it is then compare to a reference database build-in in the software in order to identify all phases or compounds present in the sample.

3.B.3 Inductively coupled plasma (ICP)

An ultramicro balance (Sartorius S4 model 1990) with a precision of 0.0001mg was used to measure 10.0 mg of sample. Weighing wax paper (Fisher 09-898-12B) was used as sample holder to facilitate the weighing process. The sample was then dissolved in 10.0 ml of a mixture of nitiric acid (Fisher A200-500ml, ~15M) and distilled water in a 3:1 volume ratio. Gentle heat and moderate stirring was applied for 10 minutes to help in the dissolution. The solution was then transferred into a 100 ml volumetric flask and distilled water was poured up to the 100 ml mark. The resulting solution concentration was 100 ppm (1 mg per liter of solution). The same procedure was followed for all the samples. Simultaneously, solutions of

100 ppm and 50 ppm were prepared from Y, Gd, Sm and Ce standard solutions (Fisher ICP standards, 1, 000 μg/ml) to generate a calibration curve. The ICP optical emission measurements were done using a Thermo Jarrel Ash Trace Scan ICP spectrometer. The liquid injection rate was 1.5 ml/min, the radio frequency power of the axial torch running at 30 psi was 13.5 W and the torch gas flow and the auxiliary flow were 18 and 1 slpm, respectively. The wavelengths used for elemental identification were 335.0 nm for Gd, 442.4 nm for Sm, 418.6 nm for Ce and 488.3 nm for Y. The elemental analysis at these wavelengths is highly recommended as it was found that using other wavelengths caused interference among the Gd, Ce and Sm signals. The interference was especially significant at 342.2 nm for Gd, 413.7 nm for Ce and 359.2 and 330.6 nm for Sm. Four independent scans were run for each sample. Each scan was programmed to identify all four elements The results were reported with their respective standard deviations. The calibration curved was based on three points, 0, 50 and 100 ppm. The linear correlation coefficient was 0.999 (R^2=0.999) for the four elements. Another calibration was done at the end of the runs to prevent de-calibration, the R^2 dropped from 0.999 to 0.997 for yttrium and for the rest of the samples dropped to 0.998.

3.B.4 Powder preparation for SEM

Each sample was mounted on a silicon wafer that was taped using a double sided carbon tape to an SEM aluminum stub. The Sartorius ultramicro balance (used also for the ICP measurements) was employed to weight 5.0 mg of powder per sample. The powder was transferred to a 4-dram vial. Then, 2 ml of DMF (N,N-Dimethyl formamide, Fisher D131-1) were added to the vial and the vial was capped and submerged in an ultrasonic bath (1510 Branson ultrasonic bath) with water for 5 minutes to break up particle agglomerates. Several solvents were tried: ethanol, distilled water, acetone, DMF, hexane/water and toluene. DMF gave the best particle dispersion, as the particles dispersed with DMF took the longest time to settle down. A Pasteur pipette was used to deposit a droplet of the dispersed suspension onto the silicon wafer and then the sample was exposed to light (Tungsten desk lamp) for 30 min. to dry. The same procedure was followed for all the samples. Finally, the samples were analyzed using a Hitachi 4700 Field Emission Scanning Electron Microscope (FE-SEM) in ultrahigh resolution mode. Energy dispersive spectrometry (EDS) was done using an X-ray detector (Oxford Instruments X-ray detector. Model 7200) interfaced to an INCA 3.04 software for data display and analysis.

3.B.5 Laser diffraction for particle size distribution

The measurements were carried out using the Mastesizer 2000 (Malvern Instruments) with the Hydro 2000 S as the liquid injector. Each sample was dispersed in distilled water and subjected to 5 minutes of ultrasound. It was observed that none of the samples re-agglomerated after sonication. A dispersant agent (Sodium hexamethaphosphate. CAS 10124-56-8) was used to help stabilizing the de-agglomerated suspension. The concentration of the dispersant in the suspension was 0.1% per weight. Finally, the suspensions were injected to the analyzer and the results collected and displayed in the Mastersizer software.

3. C Image analysis for particle size determination

The particle size distribution (PSD) analysis of the synthesized particles was based on SEM images of the various synthesized particles. This analysis involved two steps. First, the commercial software Scion Image for Windows © 2000 was employed to provide the values of the different grey levels along parallel lines drawn on the SEM images. This information was stored in several files. In the second step, the grey level data was retrieved and processed to generate number and volume PSD curves using a computational program written in MATLAB 6.0.0.88 Release 12 developed by the author of this thesis (for simplicity, this program will be referred as the in-house PSD software). Five different images were analyzed per synthesized powder sample with the intention of having sufficient particles to measure and thus provide statistically valid results for each sample. A detailed description of how to manipulate the SEM images and of how to navigate through the Scion and MATLAB softwares is presented in appendix C. A general overview of the assumptions and steps taken to obtain particle size distributions from SEM images is now described.

3.C.1 Commercial software

The Scion software was used to extract from SEM images all grey scale values along selected parallel lines superimposed on SEM images. First, the image was filtered once to remove some noise. Then, a predetermined number of parallel lines were superimposed on the SEM image every certain number of pixels, which was determined by an estimated size of the largest particle(s) visible on the SEM micrographs, i.e. if the largest particle was 20 nm, then the distance between two parallel lines was the equivalent of 20 nanometers in pixels. This conversion was based on the SEM micrograph scale; for most images a 1:1 ratio was taken. It was not always straightforward to determine the largest particle on the SEM micrographs but the main idea was to avoid double counting of particles. Therefore, overestimating the largest(s) particle size and thus the line interspacing (i.e. the distance between two parallel lines) did not significantly affect the results since more than 1,000 particles were sampled in all cases. The Scion software was then used to extract the grey scale values of each pixel along these lines and the information of each line was stored in a text file. The same procedure was followed for all the images. Fig. 3.3 shows a typical line across an image and its respective grey scale values as a function of position (in pixels).

Three different regions are identified in the image as A, B and C. Regions A and C showed typical grey values of particles visible in the image whereas region B illustrates typical grey values of the image background. Defined peaks of different broadness are observed. These represent single or multiple particles, but in general an individual peak corresponds to a single particle. Therefore, measuring the peak's broadness gives a direct indication of particle sizes.

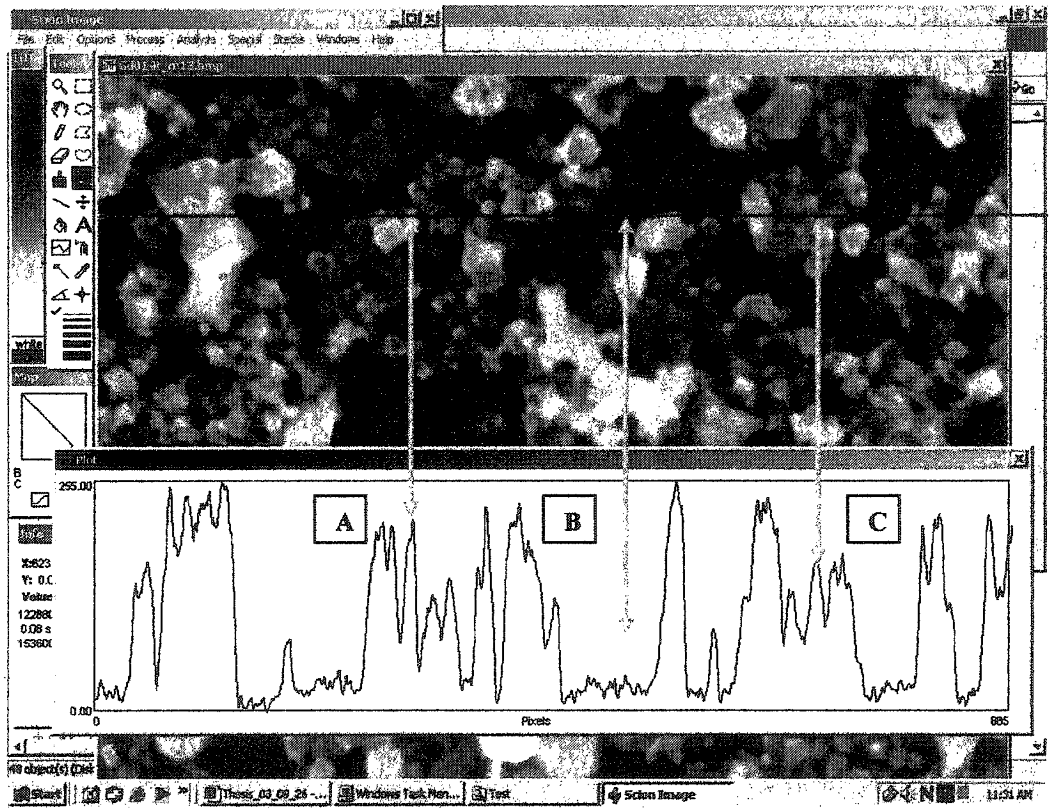

Figure 3.3 Scion software interface showing the grey scale values along a characteristic superimposed line

3.C.2 Developed algorithm (In-house PSD software)

Four separate stages involving different tasks were carried out with the in-house software. There was an additional extra task involving data fitting that was only done once after the results for all the samples analyzed were obtained. These tasks were the following: 1) data reading and organization, 2) grey scale value processing and binary matrix formation, 3) binary matrix data processing and particle size counting, and 4) particle size distribution plotting, normalization, and elimination of the technique's artifacts. The additional task was the fitting of a log-normal PSD to the computed distributions to obtain characteristic parameters for each sample. The computational algorithm employed took advantage of the fact that individual particles had very similar grey level values, and that there was a sharp decrease of these values in between particles. Therefore, individual particles could be distinguished even though they appeared agglomerated. The different stages are now described:

Stage 1: The information gathered from the Scion software was retrieved and organized in a single matrix containing all the grey scale values

Stage 2: The computational algorithm analyzed the grey values at each pixel along the superimposed lines of the SEM images. There were two requirements to meet in order to assess whether a particular grey scale value associated to an individual pixel corresponded to a particle or not. First, if the grey values were below a certain threshold value, it was assumed that the pixel belonged to the background. Second, the grey scale value of a particular pixel along the line was compared to the grey scale values of the preceding and ensuing pixels. If the grey value difference among the three pixels was smaller than an arbitrary tolerance (i.e. typically 10 units), then a value of one would be assigned to the analyzed pixel (i.e. the pixel between the preceding and the ensuing). Failure to meet this requirement would assign a value of zero to the analyzed pixel. Once the operation was completed, the ensuing pixel would now be the analyzed pixel. The entire line containing all the grey values was thus evaluated in this fashion. At the end of the line, the program switched to the next line and the examination would continue. At the end of the operation, a binary matrix would be formed, i.e. a matrix of one and zeros.

Stage 3: This binary matrix represented the different particles seen in the micrograph by continuous series of ones and the particle-particle and particle background separation was represented by at least one or more zeros. The smallest particle would be a particle in which a simple one was observed among zeros (i.e. a pixel that had an assigned a value of one). Therefore, counting the number of consecutive ones would be a direct indication of the length and thus the size of the different particles. The number of consecutive ones was then counted and the values stored in a different matrix, in this way the total number of particles could be computed. This technique underestimates the particle size by exactly two pixels and thus once the particle sizes (in pixels) were computed, two pixels were added to all particles. The underestimation was because at exactly the pixels representing the particle edges either the preceding or the ensuing pixel (i.e. the pixel before or after the edges) was greater than the tolerance and thus the value assigned to the pixel corresponding to the edge of the particle was a zero; even though it did belong to the particle. Fig. 3.4 shows the results of three randomly selected parallel lines, the left y-axis represents the grey scale values and the right y-axis represents the binary value assigned to each pixel. A dotted line was drawn after every one-zero or zero-one switch in the binary matrix to help visualize where particles begin or end. It can be seen that where sharp peaks delimited particles, the accuracy of this technique is high in determining the particle length, and it diminished somehow as the peaks resemble the pattern of a noise signal, i.e. several up-and-downs of small magnitude. Even in this situation the algorithm showed a remarkable performance when the patterns were visually compared to the analyzed image. This extra-check was done for all the samples, based on three random lines.

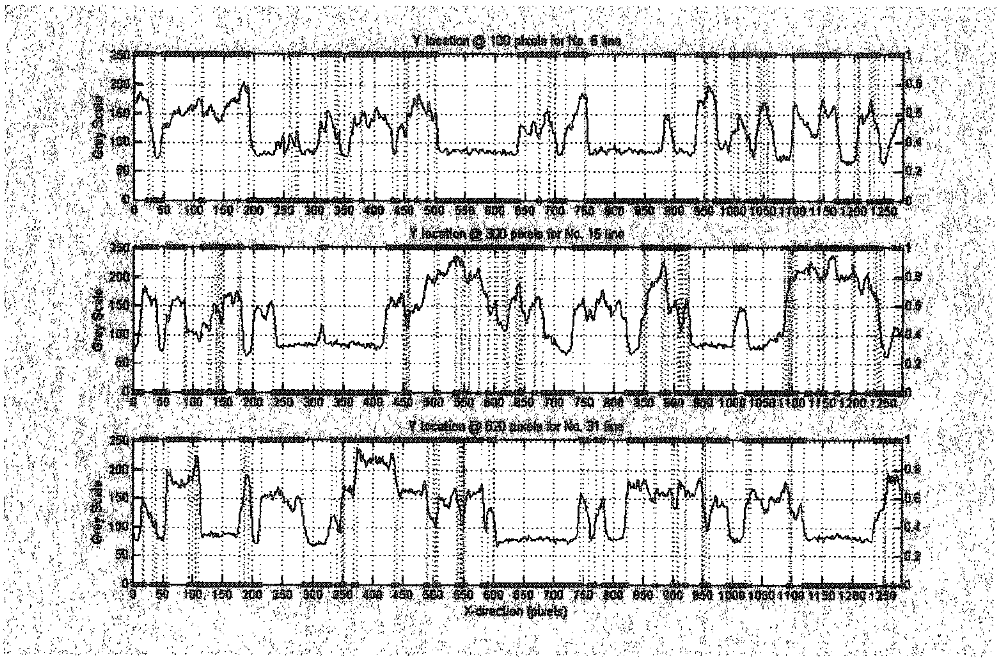

Figure 3.4 Sample results of the in-house PSD software showing the grey values of three different parallel lines across the SEM micrograph (left y-axis) and showing the results representing the particles counted along the three lines (i.e. the number of ones) (right y-axis) as a function of location (in pixels). The dotted lines represent the beginning or end of particles

Stage 4: A histogram of the total number of particles counted was plotted. This histogram was a number based PSD. The number based was used to plot another histogram in which this distribution was converted into a volume based PSD (Fig. 3.5). In this figure, it can be seen that particles of different lengths were computed (Fig. 3.5a), and that the number and the volume PSD are remarkably different (Fig. 3.5b and 3.5d).

Stage 5 (after all images were analyzed for a given powder sample): A log-normal distribution was fitted to the volume PSD based on its estimated parameters, i.e. median and standard deviation. These estimated parameters were obtained from a technique that has been used for particles present in atmospheric emissions (*Nevers, 1995*). Before estimating the volume-based PSD parameters, this distribution was truncated at the lower and upper ends and then renormalized.

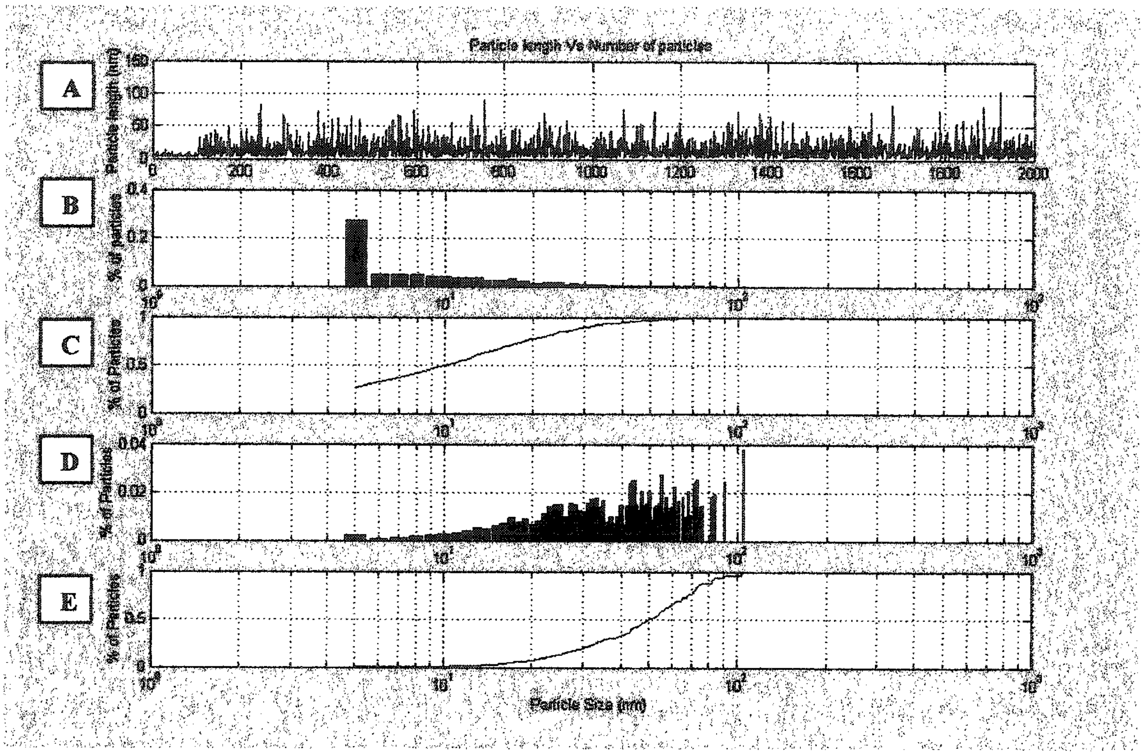

Figure 3.5 Sample results of the in-house PSD software showing a) the length of all particles sampled, b) the number based PSD histogram, and c) its corresponding cumulative PSD, d) volume based PSD histogram and e) its corresponding cumulative PSD

The truncation of the distribution was done to remove artifacts. There were two types of artifacts; the first one was exceedingly long particles that were not observed after visually comparing the results to the raw image. These long particles were the result of a series of agglomerated particles that had extremely close grey scale values, and thus were considered a single unit by the algorithm. The other artifact was the presence of very small particles, typically less than 5 nm or roughly 5 pixels. These particles appeared as a consequence of an inadequate binary assignment of values from large particles showing sharp grey scale contrasts, and they were thus removed from the original PSD. These two artifacts defined the optimum tolerance in terms of grey scale values used in the analysis of a single image. A loose tolerance between adjacent particles would favor exceedingly long particles when agglomerates were present (i.e. grey scale tolerance values greater than 15 units), and a thigh tolerance would favor particle break-up within one individual particle (i.e. values lower than 7). Therefore, this optimum tolerance must be found for each image; typically the grey scale value tolerance was found between 10 to 12 units. This very narrow range indicated that all the different images were comparable and that the technique was not especially sensitive to different grey scale values resulting from various levels of brightness or sharpness among images.

3.C.3 PSD methodology assessment

In general, commercial softwares count the number of objects in an image by first converting the image intensity (i.e. the greyscale values of each pixel) into a binary image (i.e. black and white). This implies that a certain threshold value must be selected and thus any objects below this value are ignored as they become part of the background, i.e. either black or white. The objects observed in the black and white images are then labeled. The accuracy of this process usually depends on four parameters: 1) the size of the objects, 2) whether or not any objects are touching, 3) the accuracy of the approximated background, 4) the level of connectivity selected (i.e. pixels of the same intensity, black or white, must touch along an edge to be considered connected). Finally, the area of the labeled objects is computed and the results are given in pixels. This could later be translated into any other scale by knowing the equivalence of a pixel in units of length.

The PSD commercial software approach was not adequate for the SEM micrographs taken for several reasons. First, the particles were agglomerated and thus many particles were superimposed, this meant that two or more particles were considered as one individual particle when labeling the number of objects. Second, background spots were observed within the particles as a consequence of adjusting the threshold of the image, therefore, when the particles areas were computed, these spots would not be included. Third, the level of connectivity was not well defined because most particles did not have clear separations among themselves and among themselves and the background. This significantly affected the apparent size of the objects (i.e. particles).

The method developed in this thesis was inspired by the technique described by Kaye (*Kaye, 1999*) and first developed for studying the structure of holes and dispersed species in items made from powder compacts, which use random tracks drawn across a dispersed set of fineparticles to obtain a PSD. This type of evaluation is known as the

Rosiwal intercept method and yields excellent results for log-normal particle size distributions.

The PSD methodology developed for this project offered significant advantages compared to other commercial PSD softwares used for image analysis. It took advantage of the fact that the grey scale values within particles were very similar but still sufficiently different among particles. Consequently, a binary conversion of the intensity of the image (i.e. black and white) was not required. The absence of this transformation permitted to differentiate particle boundaries adequately, since usually after conversion all particle boundaries were lost. Further, the in-house method could also account for the agglomerated particles that were located on top of other particles to which they were superimposed. Finally, the grey level tolerance that was required to define whether or not adjacent pixels correspond to the same particle could be adjusted to tighter or looser (i.e. smaller or larger tolerance) values. This provided great flexibility for images in which agglomerated particles presented similar grey values, and thus the agglomerated particles were individually counted.

There were only two scenarios in which the developed software did not perform at its best. The first one was when large particles had significantly different grey scale values within the same particle; this situation however was minimized by consistently taking SEM micrographs with lower levels of sharpness and by smoothing the image to remove excessive noise and sharpness. The second scenario occurred when the drawn lines did not exactly intersect the particles through their centers or apparent centers. Despite this drawback, it was expected that due to large number of particles sampled (more than 1,000 particles in all cases), the results would be statistically representative. Finally, adequate particle dispersion was observed to increase the algorithm accuracy because fewer agglomerates were present and thus it was easier to distinguish individual particles.

Chapter 4 Experimental results (Part 1). SOFC electrolyte powders

Cerium oxide based powders of different dopant compositions were produced using the experimental equipment described in chapter 3. Chapter 4 describes the results obtained from their characterization using: X-ray diffraction, inductively coupled plasma (ICP), scanning electron microscopy (SEM) and energy dispersive spectroscopy (EDS).

The targeted oxide compositions are given in Table 4.1

Table 4.1 Selected oxide compositions for plasma synthesis

Dopant	Selected oxide composition
Gd	• $Ce_{0.8}Gd_{0.2}O_{1.9}$
	• $Ce_{0.85}Gd_{0.15}O_{1.925}$
	• $Ce_{0.9}Gd_{0.1}O_{1.95}$
Sm	• $Ce_{0.8}Sm_{0.2}O_{1.9}$
	• $Ce_{0.85}Sm_{0.15}O_{1.925}$
	• $Ce_{0.9}Sm_{0.1}O_{1.95}$
Y	• $Ce_{0.85}Y_{0.15}O_{1.925}$
	• $Ce_{0.88}Y_{0.12}O_{1.94}$

4. A Atomization of the solutions

A study was conducted to measure the droplet size distribution of three selected solutions (each containing a different dopant) using the laser diffraction setup for droplet atomization described earlier (see chapter 3). The purpose of this study was to achieve the proper atomization parameters that would give a predetermined median droplet volume diameter (all the atomization results are based on volume diameters which should not be confused with number or surface particle diameters (see *Bernhardt, 1994*)).

The atomizing probe used was a modified version of the more general air blast atomizers which had been previously studied (*Lefebre, 1989*). From this study, an empirical correlation was found involving atomizing parameters and liquid and gas properties (see appendix A). A sensitivity analysis was carried out by varying all the variables in the correlation by a factor of two (i.e. multiplied by two and divided by two). Fig. 4.1 clearly shows that the gas flow rate is the dominant factor, as the droplet diameter greatly changed when this parameter was modified. From this figure, the liquid flow rate appeared to have a significant effect but this was not observed in the experiments reported in this work, possibly as a result of different atomizing probe designs and droplet size distribution ranges.

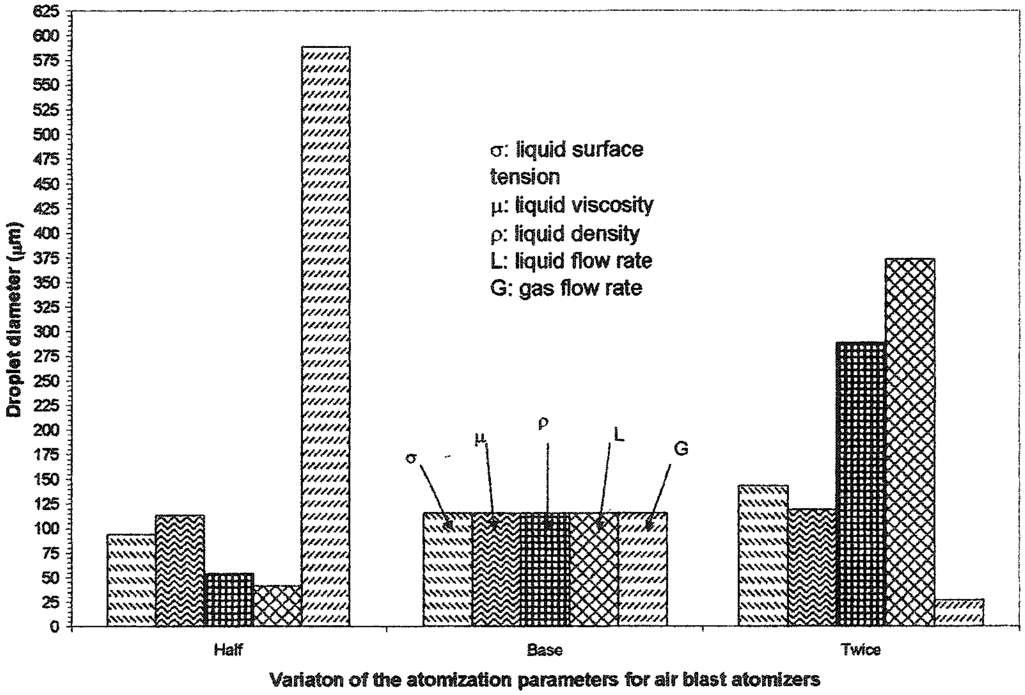

Figure 4.1 Sensitivity analysis for airblast atomizer based on a correlation proposed by Lefebre (*Lefebre, 1989*)

The gas flow rate and the probe opening were two of the most important atomizing parameters determining the atomization performance. The effect of these parameters is depicted in Fig. 4.2 where the tip of the atomization probe is greatly magnified.

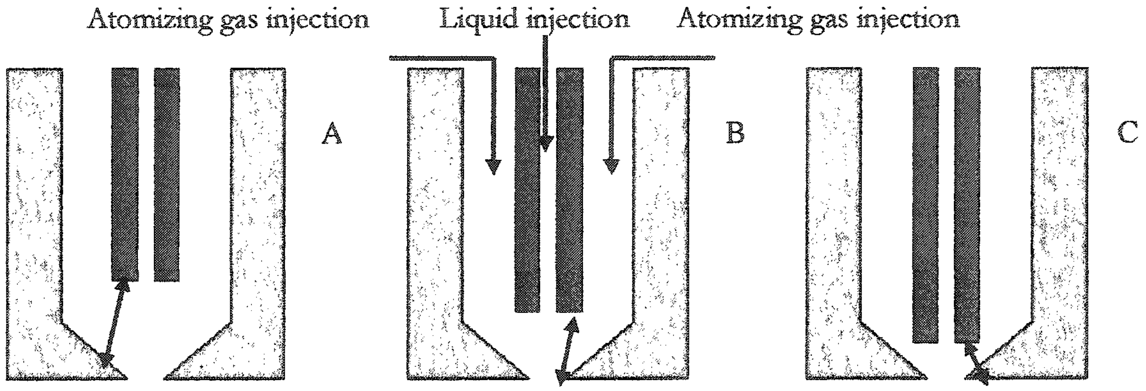

Figure 4.2 Different atomization conditions for the Tekna air blast atomization probe

Fig. 4.2b shows an optimum combination of parameters in which the gas flow rate and probe opening provide a narrow distribution center over a certain droplet diameter. The gas passes through the gap between the tip of the center tube and the edges of the tip of the probe where it meets the liquid film and causes its rupture. This gap has a particular cross-sectional area for a given probe aperture. When opening the probe, Fig. 4.2a, the gap area increases and the gas velocity decreases for a constant gas flow rate. Consequently, the energy for atomization is lower as the gas possesses less momentum and larger and broader droplet distributions are obtained. The picture is reversed when the gap decreases in area, the gas velocity greatly increases and a very fine atomization is obtained (Fig. 4.2c). Keeping the probe opening constant and changing the gas flow rate has the same effect on droplet atomization, i.e. the higher the flow rate the finer the atomization and vice versa.

The desired droplet diameter was calculated assuming that the spherical atomized droplet would follow the reaction sequence described by Bouyer (*Bouyer et al, 1997*). He suggested that the atomized droplet undergoes a reduction of size due to water evaporation, in-flight reaction, and solidification. However, the results obtained in the present work suggested that the mechanism proposed by Bouyer was incomplete. This will be addressed later (see chapter 5).

Previous findings showed that oxide particles of 10 μm in diameter were successfully used in the deposition of dense yttria stabilized zirconia coatings using induction plasma spraying (*Mailhot et al, 1997* and *Theophile et al, 1999*). Consequently, oxide particles of this diameter were taken as the basis of calculation. Table 4.5 illustrates that to obtain oxide particles of 10 μm in diameter, the diameter of the atomized droplets must be approximately 27 μm (rounded up to 30 μm for simplicity). These results also revealed that the choice of dopant did not significantly affect the calculated droplet diameter, as all the values were very close (Me represents Gd, Sm or Y).

The results presented in Table 4.2 assumed a complete reaction of the nitrate precursors, total water evaporation (i.e. water of hydration and water in the solution), dense and spherical oxide particles (as the synthesized product) and spherical atomized droplets.

Additionally, the % wt of Ce in $Ce(NO_3)_3.6H_2O$ was 32.27 and the solubility in water was 1.8 g. of cerium nitrate per gram of water. The algorithm to calculate droplet diameter is given in appendix A.

Table 4.2 Experimental and calculated properties selected synthesized products and liquid precursors

Synthesized sample	Calculated ρ of the oxide *[g/ml]*	% wt of Me in MeNitrate %	Solubility of MeNitrate in water *% g. nitrate / g. H_2O*	Measured ρ of solution *[g/ml]*	Calculated droplet diameter *[μm]*
$Ce_{0.9}Gd_{0.1}O_{1.95}$	7.59	34.84	1.5	1.603	27.3
$Ce_{0.9}Sm_{0.1}O_{1.95}$	7.64	33.83	1.5	1.616	27.4
$Ce_{0.88}Y_{0.12}O_{1.94}$	7.45	23.21	1.5	1.600	27.3

The atomization parameters were modified until the desired droplet size distribution (DSD) was attained. The results are shown in Fig. 4.3a, b and c for the three different solutions (i.e. Gd, Sm and Y precursor solutions). It can be seen that there was no further need to change the density or the viscosity of the solutions, as the DSD in all cases exhibited a maximum centered around 30 μm (Ideally, the droplet size distribution should be as narrow as possible and center over the desired median droplet diameter). The optimum parameters were obtained with a liquid flow rate of 6 ml/min and a gas flow rate of 6.5 slpm with an atomizer probe opening of ¾ of a turn. These results were highly reproducible as can be seen by comparing the three graphs. Further, from the similarly of the atomized droplet distribution results with different dopants it is expected that solutions properties such as density, surface tension and viscosity would not affect the behavior of the solutions. Finally, the atomization results presented in this section were carried out at atmospheric pressure and were only considered as the best estimations of the actual droplet size distribution during plasma operation. The operating conditions of the RF-plasma torch, i.e. reduce pressure and very high temperatures could greatly affect these estimations. It was reported that a finer droplet size coupled with a higher droplet velocity should be expected for atomization in reduced pressure environments (*Bouyer et al, 2001*). There has not been an experimental study in which the exact droplet size distribution was measured for atomized droplets in thermal plasmas.

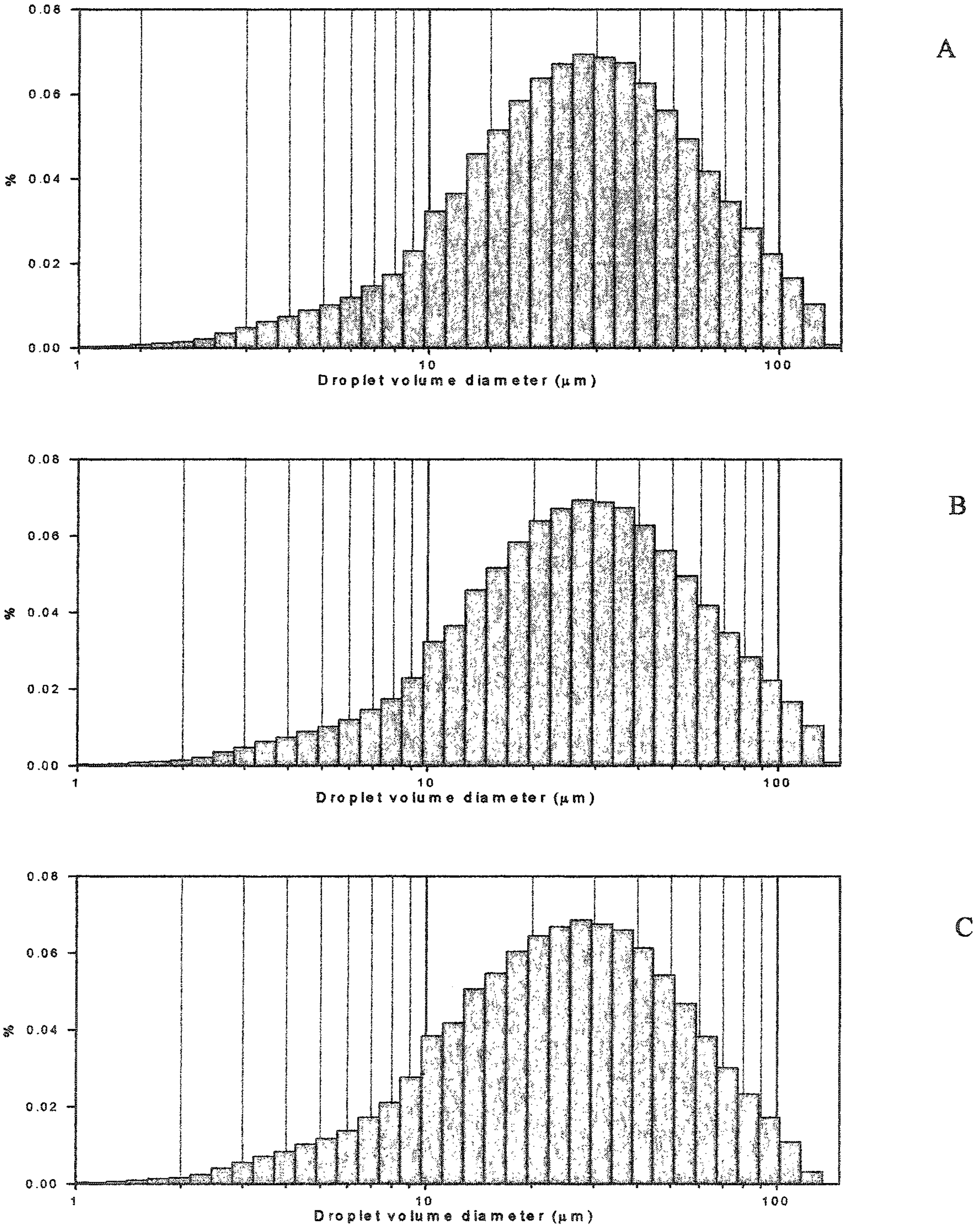

Figure 4.3 Atomized droplet size distribution: a) $Ce_{0.9}Gd_{0.1}O_{1.95}$; b) $Ce_{0.9}Sm_{0.1}O_{1.95}$; c) $Ce_{0.88}Y_{0.12}O_{1.94}$ precursor solutions. Liquid flow rate 6 ml/min, Atomizing gas (air) flow rate 6.5 slpm , atomized probe aperture ¾ turn opening

4. B X-ray diffraction analysis

The oxide powders produced were analyzed using X-ray diffraction. The results for the different dopants and dopant compositions are shown in Fig. 4.4, 4.5 and 4.6, where the different diffraction patterns are plotted in the form of normalized measured intensity (ordinate axis), versus the Bragg angle 2θ (abscissa). The X-ray diffraction patterns of the various samples were compared to the reference patterns of the pure oxides showing only Bragg peak positions as represented by the vertical bars with variable lengths (the higher the intensity of diffraction, the longer the bar). The main purpose of using powder diffractometry was to identify compounds by their diffraction pattern. No extraneous peaks were found in any of the analyzed samples, indicating that the route used to synthesize the powders allowed the production of contaminant-free products. One of the main reasons why clean samples were produced was the absence of electrodes in the plasma. In the presence of electrodes, material removed from the electrodes could contaminate the powders (i.e. electrode erosion).

Fig. 4.4, 4.5 and 4.6 showed that all major dopant peaks closely overlapped with CeO_2 peaks, especially in the case of Sm and Gd. A small amount of dopant was added to the synthesized powders and unless the dopants changed the structure of CeO_2, only CeO_2 peaks would be observed (which was the case in this work). Dopants were added to stabilize the CeO_2 solid matrix and to increase its oxygen ionic conductivity but not at the expense of disturbing its lattice structure. Therefore, the fact that all samples showed peaks at the same location with similar relative intensity than pure CeO_2 suggested that the doped CeO_2 structure was not appreciably altered and yet the dopants were incorporated into the CeO_2 lattice, as demonstrated by a chemical analysis (see section 4.C). Further, the addition of Y dopant seemed to broaden the CeO_2 peak located at ~28° as a result of a slight difference of angles between Y_2O_3 and CeO_2 reference peaks. This indicated that Y was present in the Y-synthesized samples. The small peak broadness was not observed for the Sm and Gd samples in which the dopant peaks clearly overlapped CeO_2 peaks.

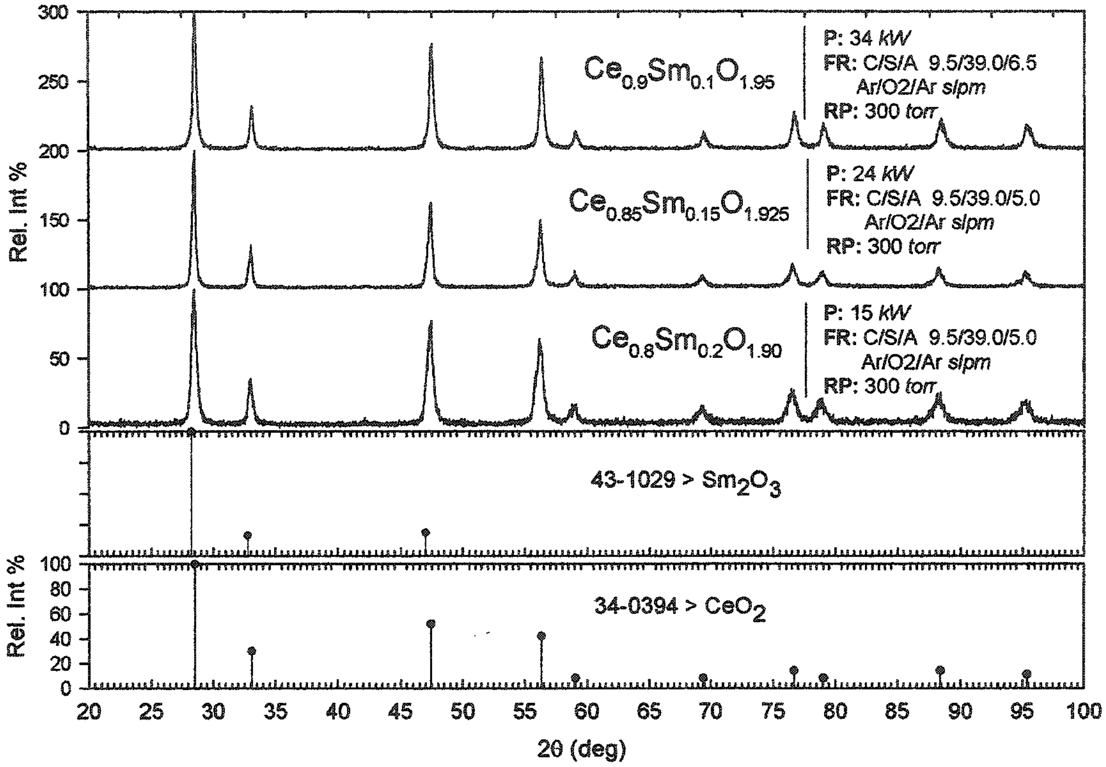

Figure 4.4 X-ray diffraction patterns of Sm-Ce synthesized powders. Sm_2O_3 and CeO_2 shown as reference patterns

The presence of characteristic CeO_2 peaks in the 2θ > 50° (Fig. 4.4), 2θ > 85° (Fig. 4.5) and 2θ > 65° (Fig. 4.6) range for the Sm, Gd and Y synthesized powders respectively confirmed the predominant presence of CeO_2 as in these ranges only the CeO_2 shows a define diffraction pattern.

Further analysis of the X-ray diffraction patterns of the different dopants did not reflect a significant change with the variation of the plasma operating conditions, i.e. plasma plate power (Sm) (Fig. 4.4), central gas flow rate and plasma power (Gd) (Fig. 4.5) and reactor pressure (Y) (Fig. 4.6). The peak intensity, peak location and peak broadening seemed to be very similar in all cases, thus indicating that the crystallinity of the powders was independent of plasma operating conditions within the range investigated.

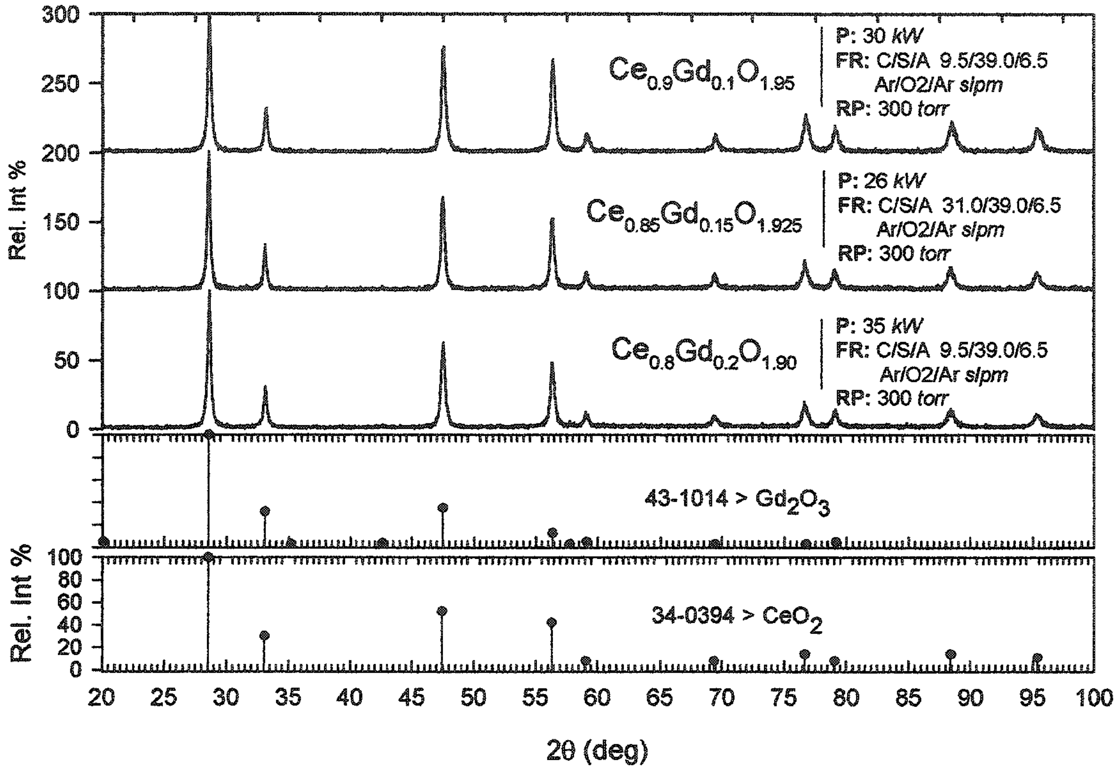

Figure 4.5 X-ray diffraction patterns of Gd-Ce synthesized powders. Gd_2O_3 and CeO_2 shown as reference patterns.

The effect of using various different dopants is illustrated in Fig. 4.7 in which the X-ray pattern of pure CeO_2 and powders of very similar dopant compositions are plotted (i.e Y=0.88, Gd=0.9 and Sm=0.9). The X-ray pattern of CeO_2 and CeO_2 with dopants all seemed to be fairly similar and therefore both the addition of dopant and the choice of dopant did not appreciably affect the crystalline pattern.

Furthermore, all samples exhibited very narrow and sharp peaks which are characteristic of highly crystalline solids. In spite of this, the small peak broadness was sufficient to estimate the size of the crystallites using the Scherrer's formula (*Cullity et al, 2001*). This formula employs the width of their diffraction curves at an intensity equal to half the maximum intensity, termed the full-width at half maximum (see appendix A). The crystallite sizes are given in Table 4.3 for all the samples based on the (100), (200), (220) and (311) planes (i.e. approximately 2θ = 28°, 35°, 47°, and 57°).

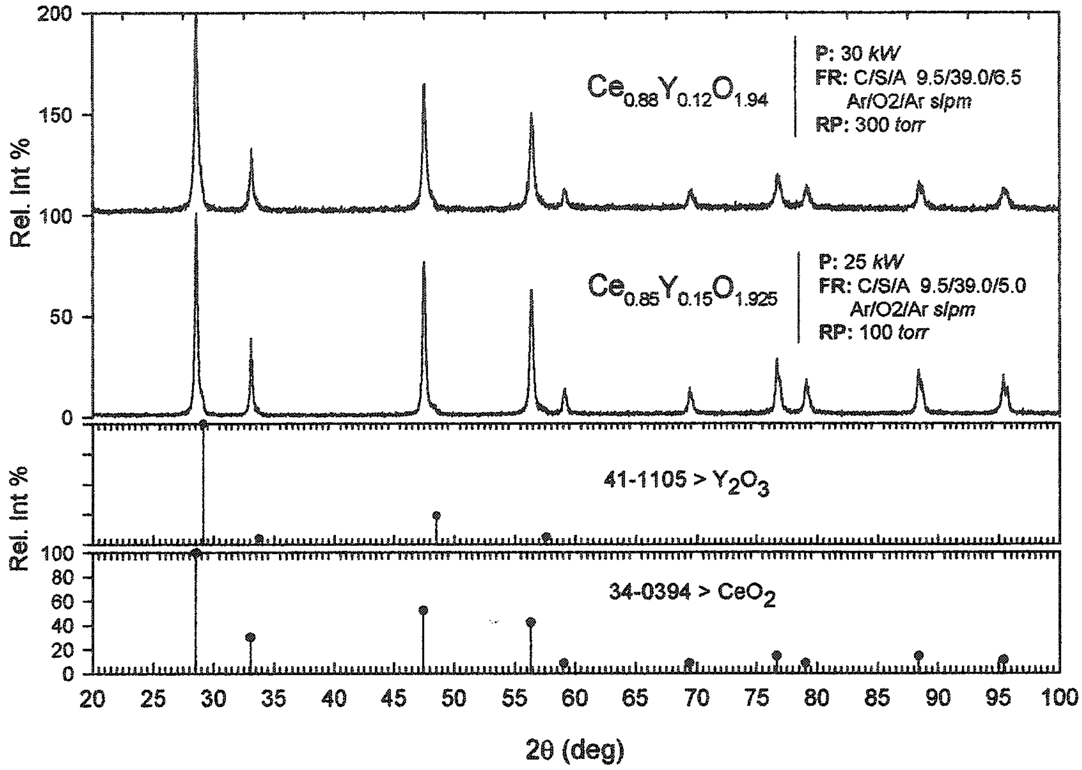

Figure 4.6 X-ray diffraction patterns of Y-Ce synthesized powders. Y_2O_3 and CeO_2 shown as reference patterns

The estimated crystallite sizes for a given plane were within the 20-35 nm range for all the samples with the exception of CeO_2. Samples of different dopants did not show a significant difference among their crystallite sizes and thus it was confirmed that the choice of dopant did not affect the size of the crystals. It also appeared that pure CeO_2 showed slightly larger crystallite sizes, indicating that dopant addition favored smaller crystals. The presence of dopants slows the CeO_2 crystal growth. It is hypothesized that, as the CeO_2 crystals start growing, the incorporation of dopant cations into the CeO_2 solid lattice retarded crystal growth. It is important to note that even though the crystalline size remained fairly constant, the particle size did not follow the same behavior. This was because a particle could be composed of several crystals of unaffected size but the size of the particle could change (i.e. the number of crystals in a particle could vary depending on the particle size).

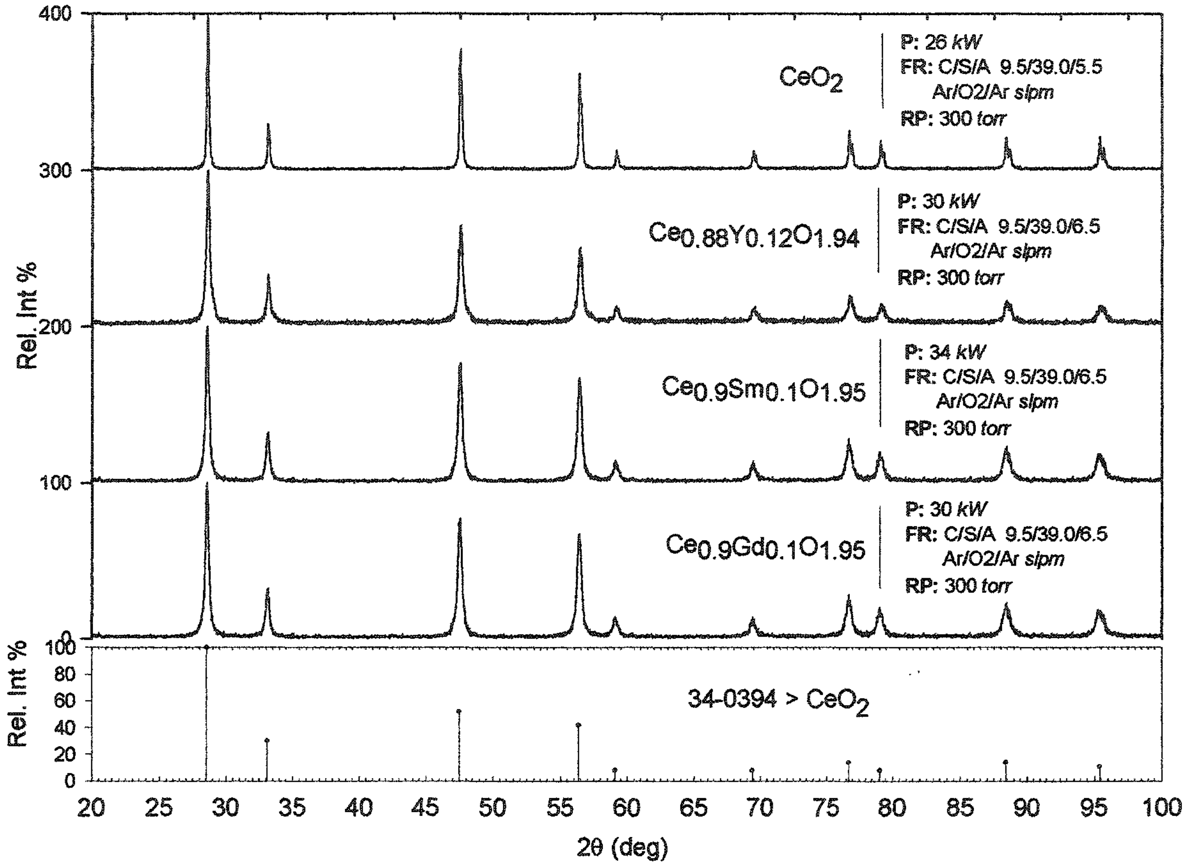

Figure 4.7 Comparison of selected X-ray diffraction patterns of Gd-Y-Sm-Ce and CeO_2 synthesized powders. CeO_2 shown as reference pattern

Table 4.3 Estimated crystallite size of the synthesized ceramic powders

	Synthesis product	Estimated crystallite size for selected planes (nm) Plane (111)	Plane (200)	Plane (220)	Plane (311)
1	$Ce_{0.8}Gd_{0.2}O_{1.9}$	29.1	24.5	24.2	25.1
2	$Ce_{0.85}Gd_{0.15}O_{1.925}$	32.5	34.1	35.0	42.7
3	$Ce_{0.9}Gd_{0.1}O_{1.95}$	27.8	26.9	24.2	25.1
4	$Ce_{0.8}Sm_{0.2}O_{1.9}$	19.5	21.9	23.4	24.4
5	$Ce_{0.85}Sm_{0.15}O_{1.925}$	27.0	28.3	28.0	42.7
6	$Ce_{0.9}Sm_{0.1}O_{1.95}$	22.4	24.5	24.2	22.3
7	$Ce_{0.85}Y_{0.15}O_{1.925}$	29.3	51.1	31.7	34.8
8	$Ce_{0.88}Y_{0.12}O_{1.94}$	29.1	32.7	27.6	25.1
9	CeO_2	39.0	51.1	50.7	51.5

It was shown that varying the dopant composition of a particular dopant appeared not to have a significant effect on the X-ray diffraction patterns as equally sharp and narrow peaks of comparable relative intensities were observed for the plasma synthesized powders. However, it was reported in a recent work that ceramic powders of $Ce_{1-x}Gd_xO_{2-x/2}$ and $Ce_{1-x}Sm_xO_{2-x/2}$ produced by other method showed a relationship between peak intensity and dopant amount, especially for the (111) and (200) planes (Fig. 4.8a and 4.8b) (*Zha et al, 2003*). These samples were produced from nitrate salts by the oxalate co-precipitation route (precipitation with dilute oxalic acid and ammonia at pH 6.6-6.9), followed by calcinations in air at 750 °C and sintering at 1,400 °C for 5 h in air.

It is evident that the two methods produced powders of different crystallinity. The plasma route produced powders in which the X-ray pattern resembled that of pure CeO_2, despite the amount of dopant added, and thus it may lead to better electrolyte materials once tested during SOFC operation. The confirmation of this hypothesis is beyond the scope of this thesis as the electrolyte layers were not produced, but the difference in crystallinity of the same materials was considered an interesting finding and thus it is included in this work.

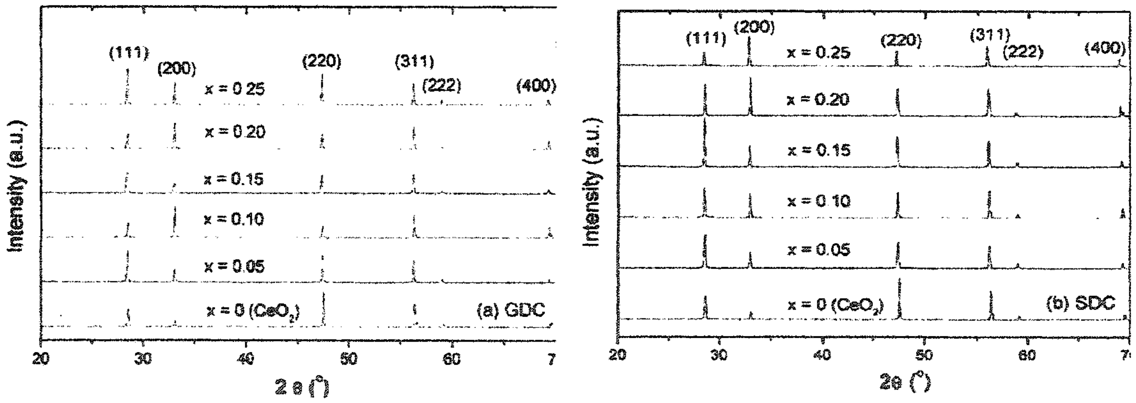

Figure 4.8 X-ray diffraction patterns of doped (a) $Ce_{1-x}Gd_xO_{2-x/2}$ and (b) $Ce_{1-x}Sm_xO_{2-x/2}$ produced by the oxalate co-precipitation route (Zha et al, 2003)

4. C Metal analysis of products (ICP)

The oxide powders produced were analyzed using ICP to determine the exact cerium and dopant content. The results obtained are presented in Table 4.4. This table shows the mole fraction of different Ce, Gd, Sm and Y synthesized samples. Four different measurements were taken per sample.

It could be seen that 7 out of 9 samples were within the 95% confidence intervals (two sided t-statistics with 3 degrees of freedom). For 2 of the Sm samples, the Sm dopant content exceeded the desired mole fraction values by approximately 0.01 to 0.02, which was a very small deviation. Therefore, the ICP results could be used as strong evidence to support solution plasma synthesis as an adequate method to produce oxides of compositions within a 5% error.

The Sm difference could be attributed to a slight inaccuracy in the weighing of the initial samarium nitrate amounts or to peak interference among dopants (even though the wavelengths at which the elements were detected were carefully selected (see Chapter 3)).

Table 4.4 ICP analysis of synthesized oxide powders

Target powder composition	Cerium content (Mole fraction)			Dopant content (Mole fraction)		
	Ce μ	**Std**	**95% Confidence Interval**	**Gd μ**	**Std**	**95% Confidence Interval**
$Ce_{0.8}Gd_{0.2}O_{1.9}$	0.794	0.012	$0.775 < \mu < 0.812$	0.206	0.006	$0.196 < \mu < 0.215$
$Ce_{0.85}Gd_{0.15}O_{1.925}$	0.834	0.019	$0.804 < \mu < 0.864$	0.166	0.006	$0.156 < \mu < 0.176$
$Ce_{0.9}Gd_{0.1}O_{1.95}$	0.894	0.030	$0.846 < \mu < 0.894$	0.106	0.004	$0.100 < \mu < 0.112$
	Ce	**Std**	**95% C.I.**	**Sm**	**Std**	**95% C.I.**
$Ce_{0.8}Sm_{0.2}O_{1.9}$	0.780	0.021	$0.747 < \mu < 0.813$	0.220	0.002	$0.217 < \mu < 0.223$
$Ce_{0.85}Sm_{0.15}O_{1.925}$	0.832	0.028	$0.787 < \mu < 0.877$	0.168	0.003	$0.163 < \mu < 0.173$
$Ce_{0.9}Sm_{0.1}O_{1.95}$	0.888	0.031	$0.839 < \mu < 0.937$	0.112	0.002	$0.109 < \mu < 0.115$
	Ce	**Std**	**95% C.I.**	**Y**	**Std**	**95% C.I.**
$Ce_{0.85}Y_{0.15}O_{1.925}$	0.842	0.003	$0.837 < \mu < 0.847$	0.158	0.003	$0.153 < \mu < 0.163$
$Ce_{0.88}Y_{0.12}O_{1.94}$	0.884	0.019	$0.854 < \mu < 0.914$	0.116	0.002	$0.113 < \mu < 0.119$
	Ce	**Std**	**95% C.I.**			
CeO_2	0.981	0.009	$0.967 < \mu < 0.995$			

4. D Local composition and particle morphology by energy dispersive spectroscopy (EDS) and scanning electron microscopy (SEM)

4.D.1 Local composition by energy dispersive spectroscopy (EDS)

To investigate the individual elements present in the oxide powders a qualitatively energy dispersive spectroscopy procedure was employed. This technique detects the X-rays emitted from the specimen under study bombarded by electrons from the scanning probe. The X-ray spectrum provides information on the elements present from their energy through a previously calibrated multichannel analyzer and the elemental concentration from X-ray intensity (*Goldstein, 1992*). Fig. 4.9, 4.10 and 4.11 show the spectra obtained for all the samples produced. Some figures showed gold (Au), palladium (Pd), silicon (Si), boron (B) and oxygen (O) peaks, in addition to the expected Ce, Gd, Sm and Y peaks.

Gold and palladium peaks were found because a gold-palladium coating was applied to the silicon wafers that were used as sample holders to increase their electronic conduction and prevent particle charging by the impinging SEM electron beam. Applying these coatings did not significantly decrease particle charging because SEM images and EDS analyses of equal resolution and quality were obtained when the coatings were not applied. This was later found when several images were collected for the particle size distribution (PSD) study (see chapter 5). In this study, high quality SEM images were taken using only particles deposited on silicon wafers to avoid having the coating as the image background. Therefore, Au-Pd wafer coating is unnecessary and not recommended in the future.

Boron peaks were also seen because the silicon wafers used had boron traces in their lattice. Carbon peaks were identified. These peaks are generally present in EDS analysis due to carbon contamination from CO_2 in the microscope chamber as a consequence of sample handling.

Finally, the larger K_α oxygen peak at 0.523 keV, encountered in all samples, corroborated the fact that oxide mixtures of CeO_2 and Me_2O_3 (Me=Gd, Sm and Y) were produced, as this peak was too high to be confused for oxygen contamination. The height (i.e. the number of counts) and broadness of the peaks could not be used for quantitative studies of dopant or cerium contents. Quantitative EDS analysis was beyond the scope of this project due to the difficulties involved in acquiring EDS spectra for both the samples and pure standards under exactly the same experimental conditions, i.e. different electron-material interaction volumes, and particle orientations. There was a strong influence of the area analyzed with the EDS detector on the relative intensities of the metal peaks, i.e. the 15% Gd sample appeared to have the smallest peak intensity and similar effects were observed in Sm samples. Therefore, EDS analyses were used only as a qualitative technique.

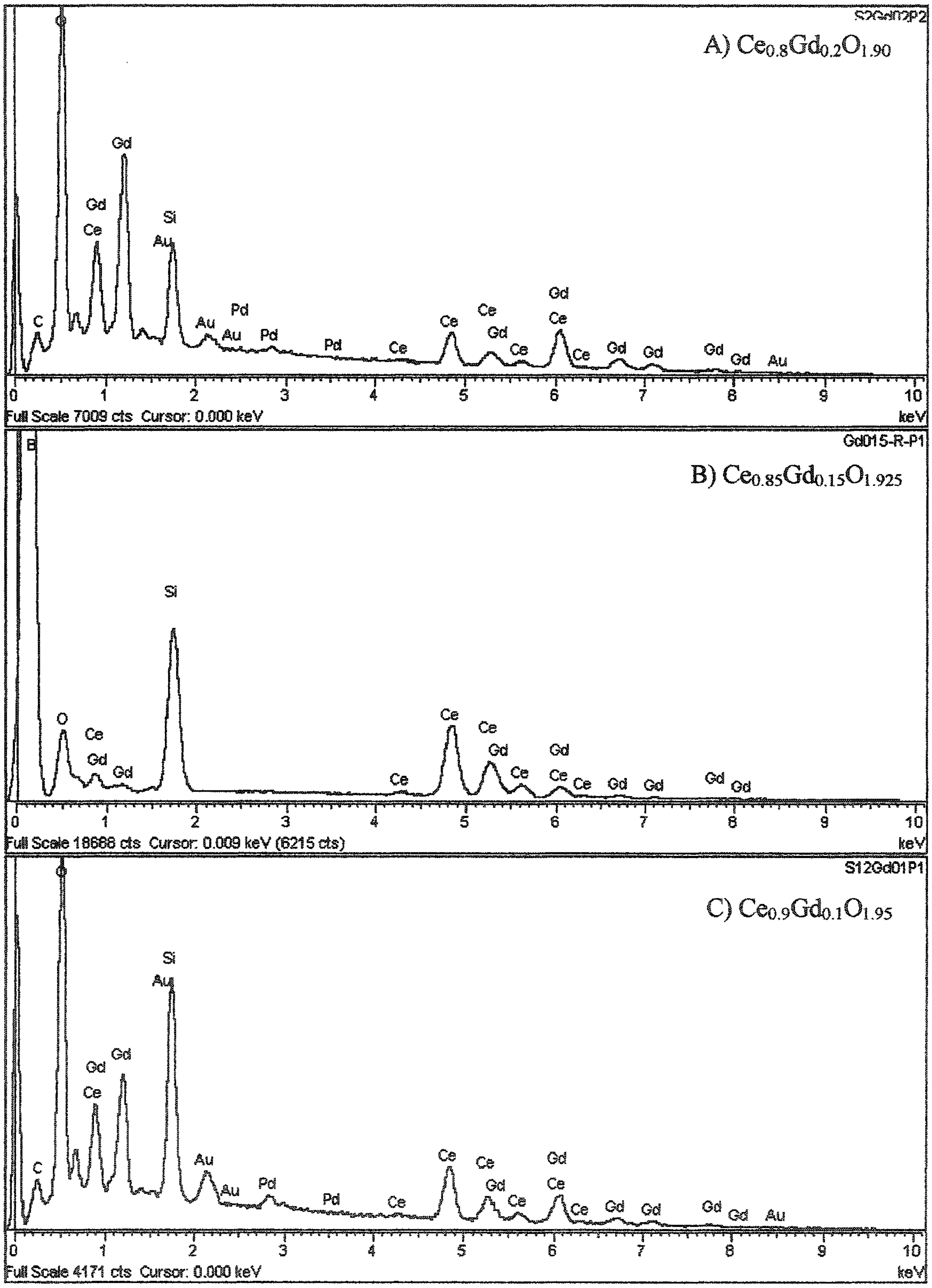
A) $Ce_{0.8}Gd_{0.2}O_{1.90}$

B) $Ce_{0.85}Gd_{0.15}O_{1.925}$

C) $Ce_{0.9}Gd_{0.1}O_{1.95}$

Figure 4.9 EDS patterns of Gd-Ce oxide powders (100 sec. live time, 15 kV, 35% dead time (DT) and 12 mm working distance (WD))

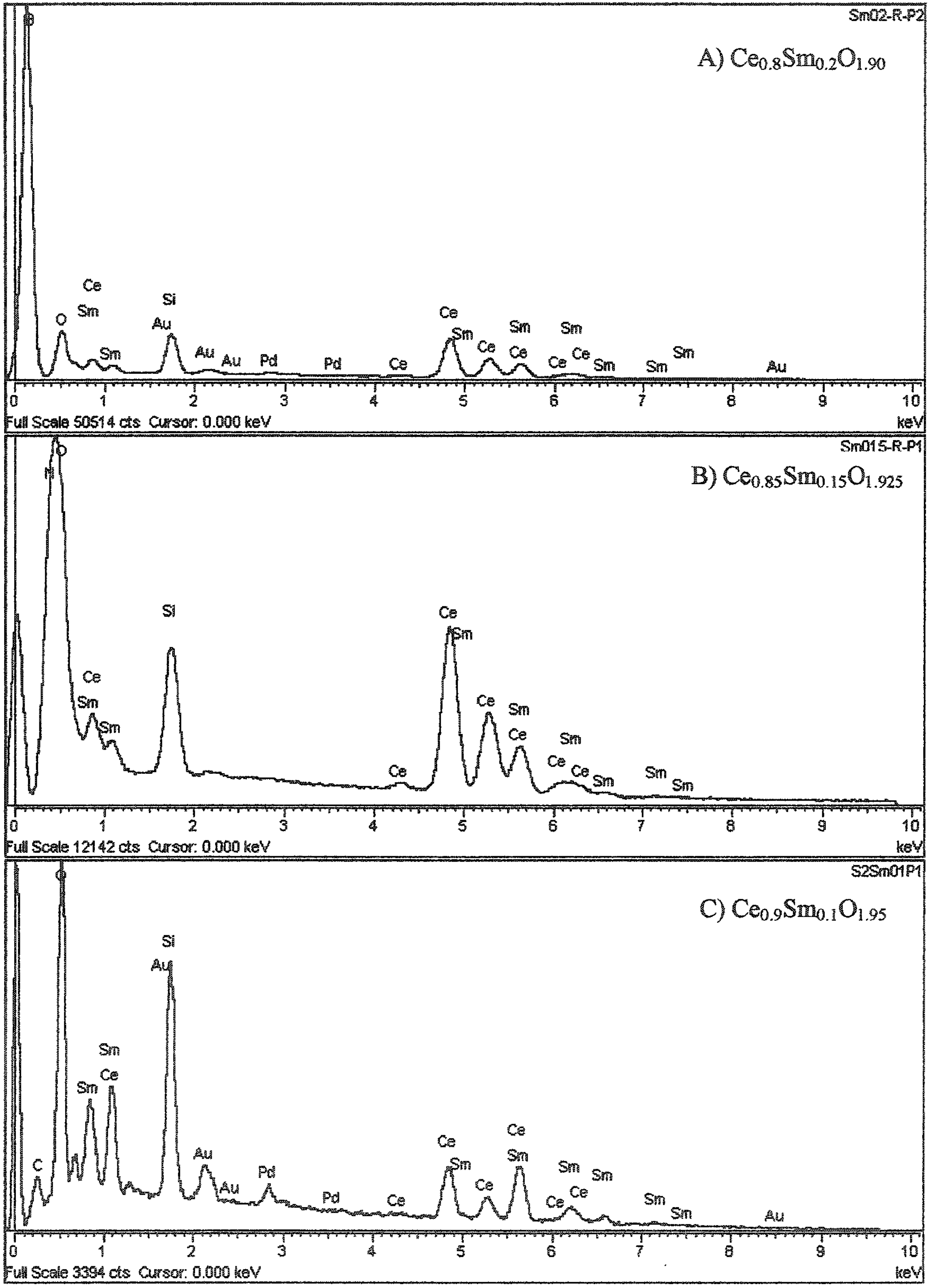

Figure 4.10 EDS patterns of Sm-Ce oxide powders (100 sec. live time, 15 kV, 35% DT and 12 mm WD)

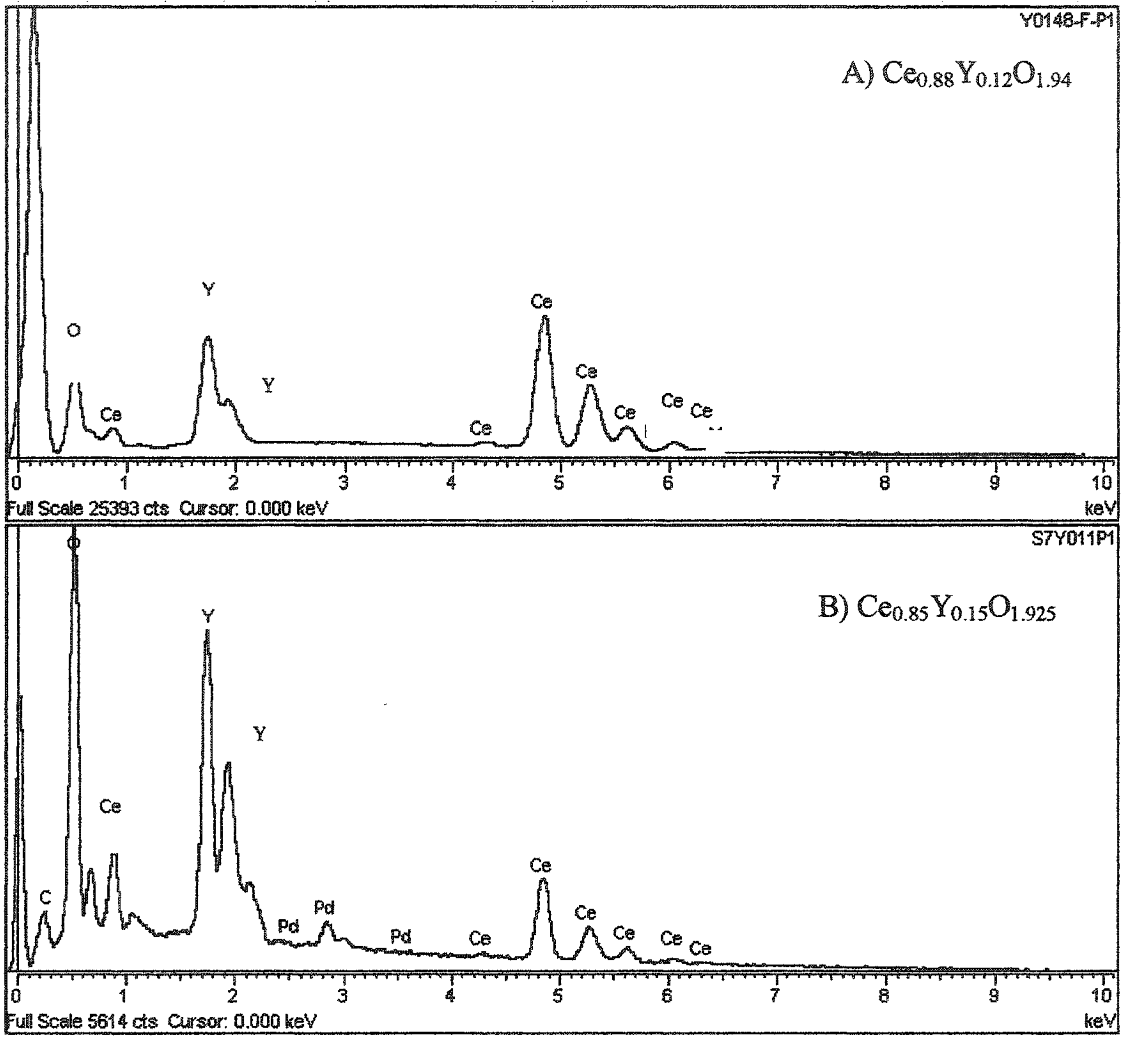

Figure 4.11 EDS patterns of Y-Ce oxide powders (100 sec. live time, 15 kV, 35% DT and 12 mm WD)

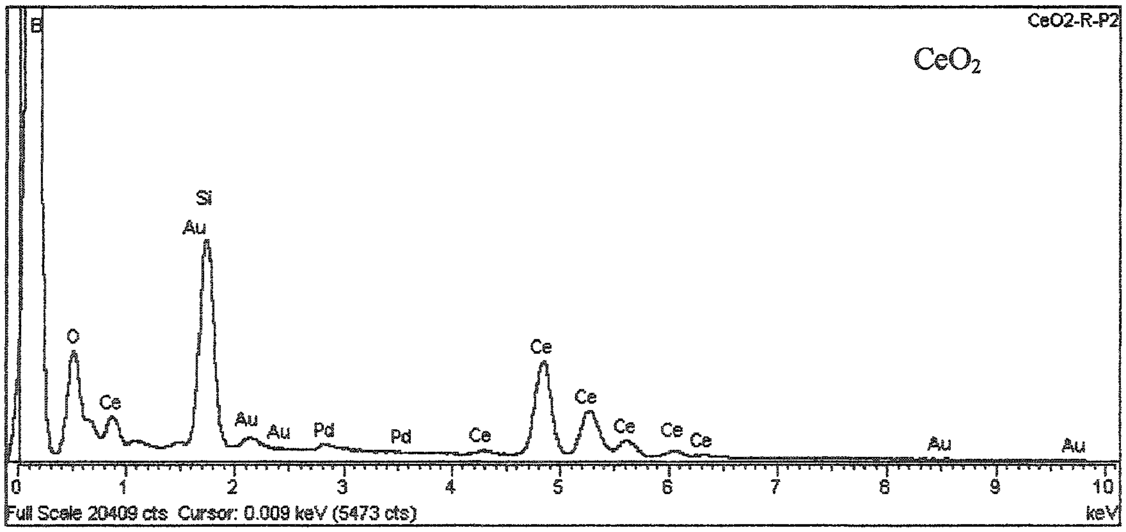

Figure 4.12 EDS patterns of CeO_2 oxide powders (100 sec. live time, 15 kV, 35% DT and 12 mm WD)

There were several X-ray emission peaks representative of Ce. Among these the L_β and L_α at 5.262 and 4.840 keV respectively, and one well defined M_α at 0.8831 keV were the most important. These peaks were present in all the samples, thus confirming the presence of Ce. Gd showed well defined peaks at 6.714, 6.069 and 1.185 keV (Fig. 4.9). Some of the Gd peaks overlapped with those of Ce but the ones located at 1.185 and at 6.714 keV validated the presence of Gd as these did not overlap with any of the Ce peaks. In Fig. 4.10, Sm and Ce peaks were observed. Sm displayed peaks at 6.206 and 5.636 keV in the high energy range and 1.081 keV in the low range. The peak located at 1.081 keV was particularly useful to determine the presence of Sm as it did not significantly overlap with any of the Ce peaks. Yttrium identification (Fig. 4.11) was simpler as this element had L_β and L_α peaks at 1.996 and 1.922 keV that could be clearly distinguished from any of the Ce peaks.

Moreover, Y has no peaks overlapping with the Ce peaks in the >5 keV range and consequently Ce was easily detected in all the Y-Ce samples. Pure CeO_2 was successfully synthesized as confirmed by the presence of only Ce and O peaks in Fig. 4.12. A nitrogen peak, at 0.392 keV (Fig. 4.10b) fairly close to the one of oxygen, was found in only one sample suggesting that some nitrate traces remained unreacted after the plasma treatment for this sample. This occurred at the lowest plasma power (15 kW) used to synthesized the $Ce_{0.85}Sm_{0.15}O_{1.925}$ oxide and thus this power represented the lower operating limit at which complete calcination was no longer achieved. EDS could then be used to determine the plate power range at which complete calcinations could be obtained within the nitrogen detection limit of the SEM (approximately 5-10% in mass depending on the machine used).

4.D.2 Particle morphology by scanning electron micrographs

The oxide powders produced were analyzed using the SEM. Tyical results are shown in Figs. 4.13, 4.14 and 4.15. Four micrographs of Gd-Ce and Sm-Ce samples are presented in Fig. 4.13 to illustrate what was observed for each powder oxide sample. Each sample exhibited three different levels of particle size, i.e. hard and loose agglomerates in the ~2-10 μm range (Fig. 4.13a); dense spherical particles and hard and loose agglomerates in the ~0.1-1.0 μm interval (represented by bright particles in Fig. 4.13b and clearly seen in Fig. 4.13c,d), and a great number of nanoparticles <0.1 μm (Fig. 4.13d).

Particle dispersion was a key issue when analyzing the samples. If the particles were not properly dispersed, particle agglomeration was easily observed. For instance, Fig. 4.14c and 4.14d showed the same sample dispersed with DMF (N,N-dimethyl foramide) and H_2O. When the sample was dispersed with DMF, the particles remained separated after sonication helped break down the agglomerates. It was important to choose the correct dipersing agent so that a clear sample could be analyzed. DMF had been suggested as the dispersant agent for Si-C-N nanopowders (*Chen et al, 2001; Bernhardt, 1994*) based on the time that it took for the particles to settle once dispersed. DMF also provided the best results in this study.

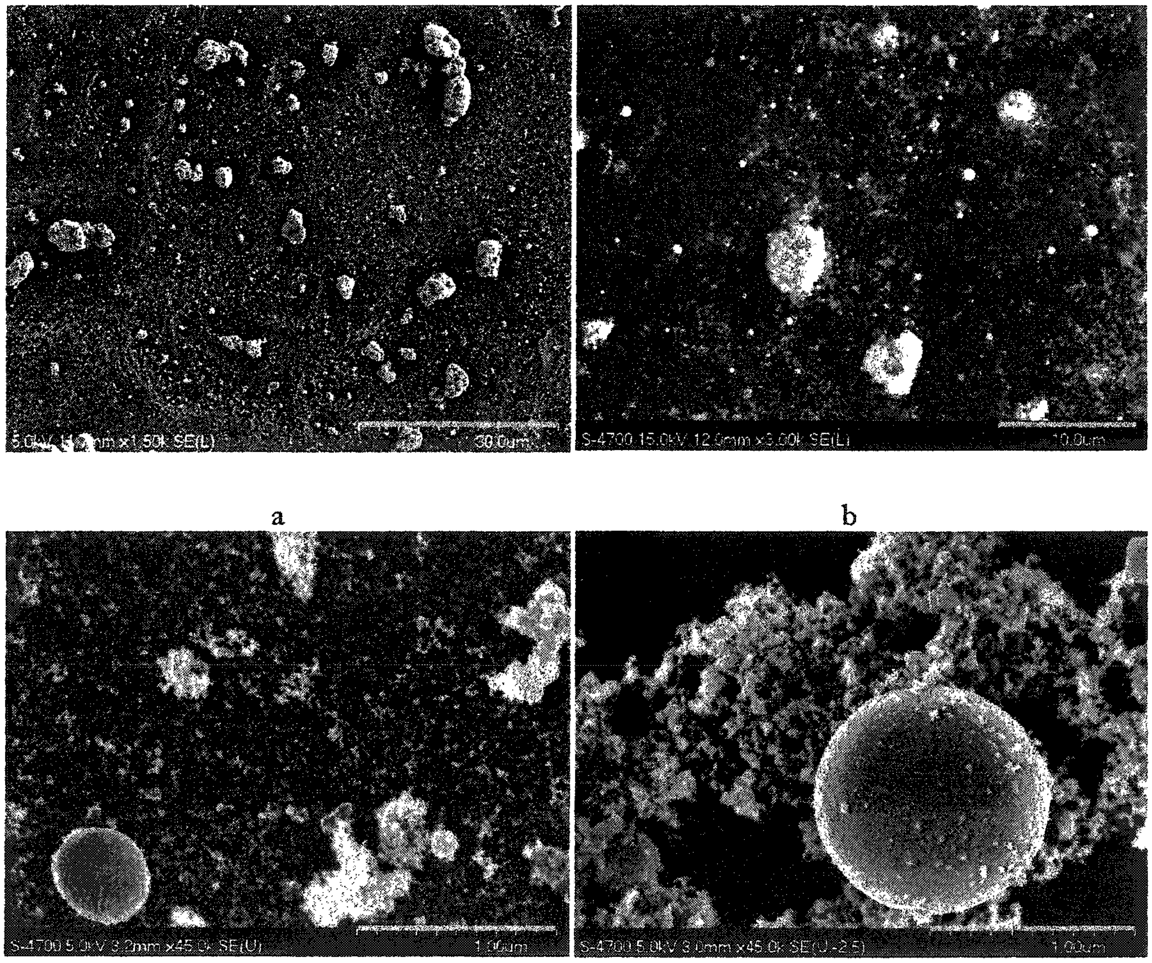

a b

c d

Figure 4.13 a) $Ce_{0.9}Gd_{0.1}O_{1.95}$; b) $Ce_{0.85}Gd_{0.15}O_{1.925}$; c) $Ce_{0.8}Sm_{0.2}O_{1.9}$; d) $Ce_{0.85}Sm_{0.15}O_{1.925}$

Utrasonication was also very effective in dispersing the nanopowders, confirming what it was reported in previous studies (*Jorge et al, 1990*).

Micrographs taken with the same scale showing all the samples produced are illustrated in Fig. 4.14a and 4.14b and 4.15a-f. It can be seen that all nanoparticles had similar structures and had a strong inclination to form agglomerates. This is a result of the strong van der Wals forces present at the surface of the particles. There was little difference among the nanoparticles containing Sm, Gd or Y, even though the plasma operating parameters were not exactly the same for all the samples. The nanoparticles were angular rather than spherical. Spherical particles were always much larger than these nanoparticles. Finally, the SEM images of pure CeO_2 showed only angular particles (Fig. 4.14c and 4.14d). Based on this finding, it was hypothesized that the most stable configuration for CeO_2 was angular and not spherical and that the addition of dopant favored the formation of spherical particles.

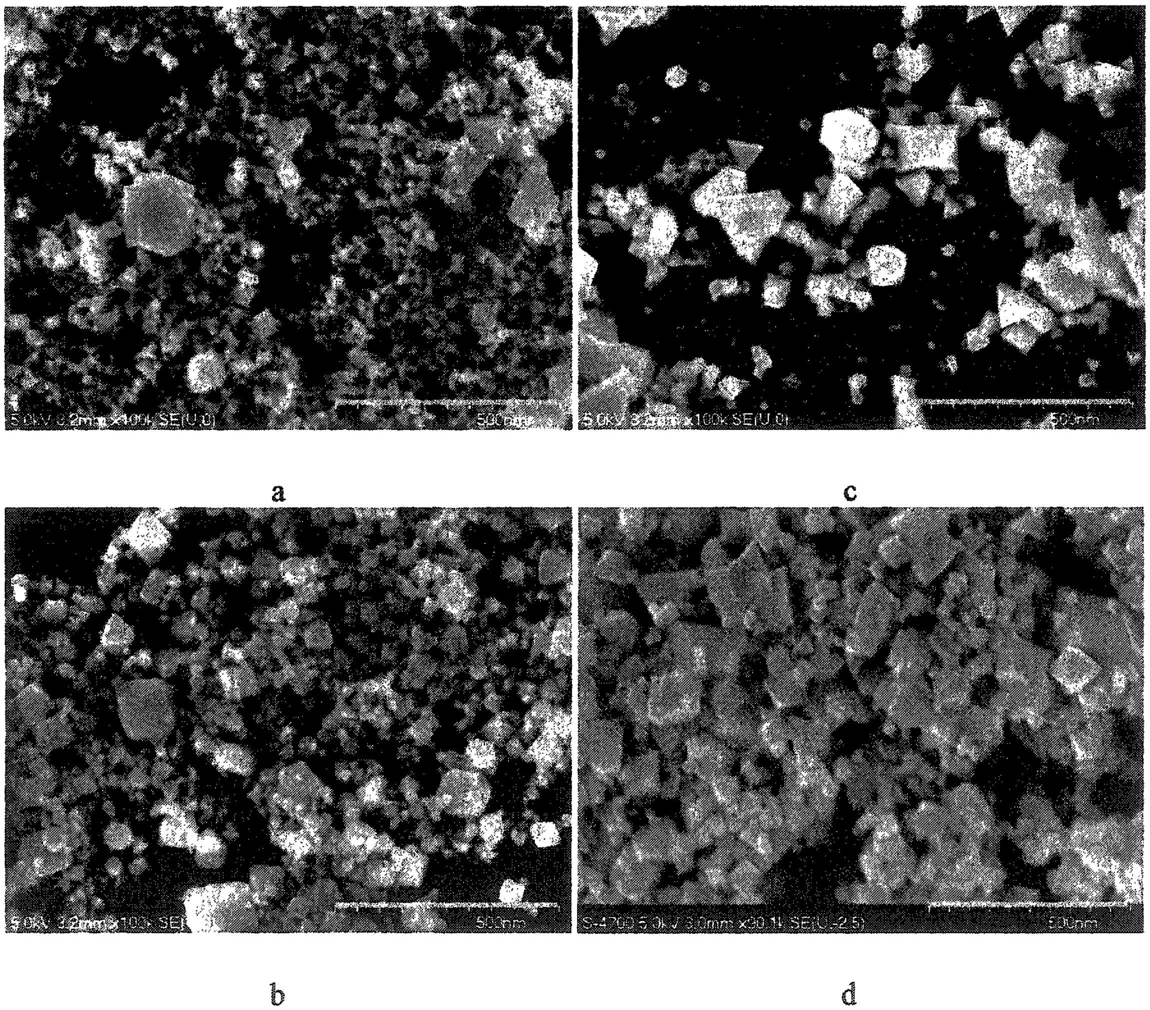

a c

b d

Figure 4.14 a) $Ce_{0.88}Y_{0.12}O_{1.94}$; b) $Ce_{0.85}Y_{0.15}O_{1.925}$; c) DMF dispersion CeO_2; d) H_2O dispersion CeO_2

The mechanism proposed by Bouyer (*Bouyer et al, 1997*) should have led to obtain ~10 µm dense and spherical particles based on the calculations done for the size of the atomized droplets. However, all spherical particles analyzed were produced in much smaller sizes (~1.0 µm or less). This suggested that the proposed particle formation mechanism was incomplete and other phenomena were affecting particle formation. A new mechanism has been proposed to account for the three different particle size levels; this will be thoroughly discussed in chapter 5.

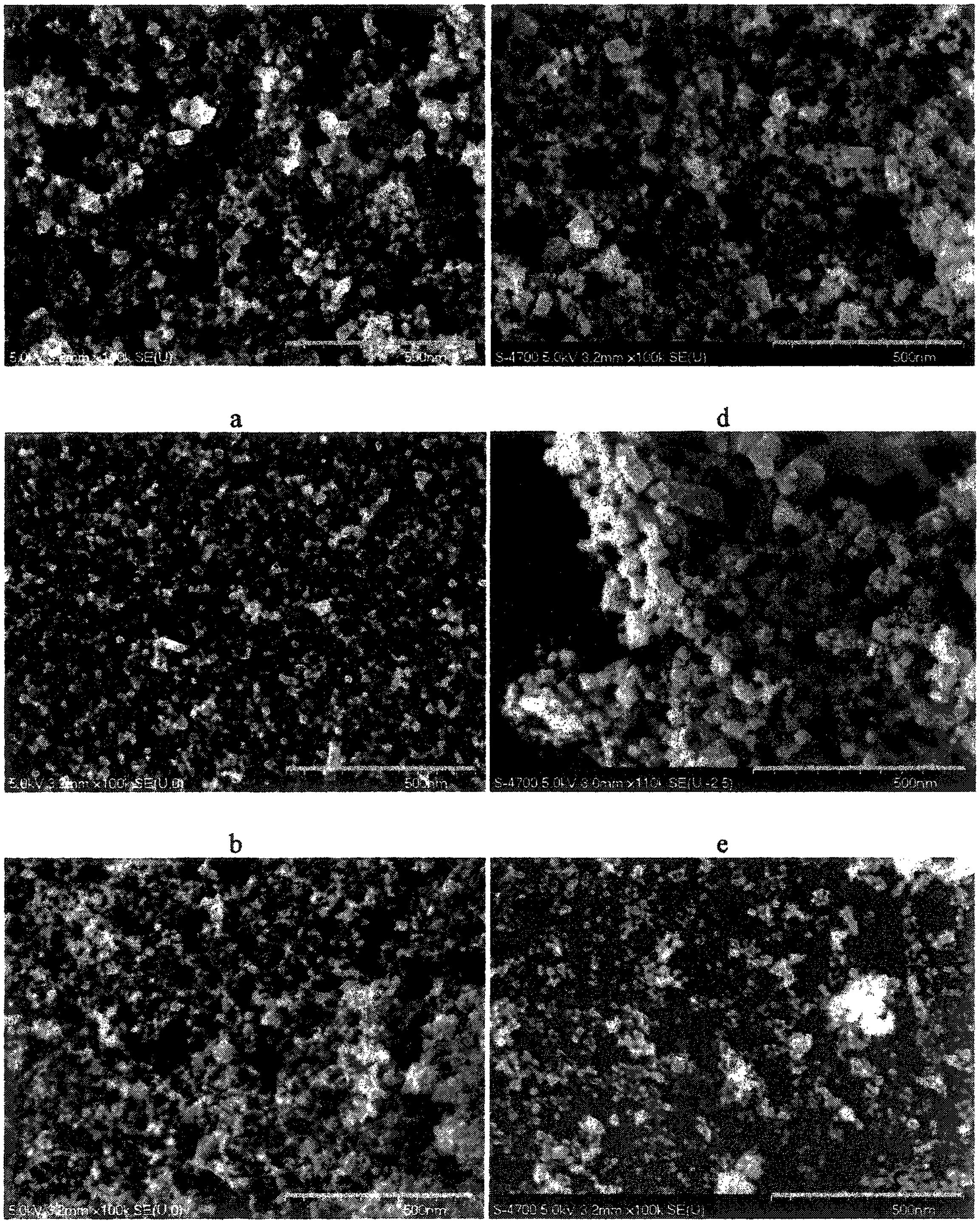

a d

b e

c f

Figure 4.15 a) $Ce_{0.9}Gd_{0.1}O_{1.95}$; b) $Ce_{0.85}Gd_{0.15}O_{1.925}$; c) $Ce_{0.8}Gd_{0.2}O_{1.9}$; d) $Ce_{0.9}Sm_{0.1}O_{1.95}$; e) $Ce_{0.85}Sm_{0.15}O_{1.925}$; f) $Ce_{0.8}Sm_{0.2}O_{1.9}$;

Chapter 5 Experimental results (Part 2) Particulate formation and analysis

In this chapter, the different types of synthesized particles are described. Also, a study is presented of the effects of selected plasma operating parameters, i.e. plate power, reactor pressure and central gas flow rate, on product size. This information served as the basis for the development of a more detailed model of particle formation starting from atomized droplets. Although it was shown in chapter 4 that the operating conditions did not influence the powder composition and crystallinity, they did affect the particle size distribution. In this chapter, the synthesized powders were labeled *"R"* if collected from the main reactor and *"F"* if the powders were collected from the filters (e.g. $Ce_{0.8}Sm_{0.2}O_{1.9}$-R or $Ce_{0.8}Sm_{0.2}O_{1.9}$-F)

5. A Particle size distribution analysis (SEM and laser diffraction)

The volume particle size distributions obtained from laser diffraction measurements of several samples synthesized at different plate powers are shown in Fig. 5.1. Each distribution showed either two or three distinctive "humps" or "modes". Having multimodal distributions was unexpected because each mode is associated with a particular particle formation mechanism. These results suggested that there must be different types of particles of roughly 0.04 -0.5 µm, 1-4 µm and 5-20 µm, and that these particles were produced in different amounts according to the various operating conditions. The different types of particles are now described:

1. Hard-agglomerates: These particles were in the range between 5 to 20 µm (Fig. 5.1) and observed in SEM micrographs, Fig. 5.2a and 5.2b. These agglomerates were chunks of porous material that had irregular shapes and that seemed to be present in all the samples in various quantities as indicated by the different heights of the 5-20 µm humps in different samples. They were abundant for the 15 kW plate power (the lowest) samples. The hard agglomerates were formed when the temperature of the agglomerated particles was less than the oxide melting temperature but it was sufficiently close to promote sintering and thus particle coalescence (typically 2/3 of the oxide melting temperature in Kelvin).

2. Spherical particles: These particles were dense and solid with sizes ranging from 0.1 μm to 1 μm in diameter (Fig. 5.1), and were almost spherical (Fig. 5.2c and 5.2d). The surface of these particles was not entirely smooth. Spherical particles were formed when the particle temperature was equal to or greater than the oxide melting temperature. The surface tension of materials in the liquid state and a relatively fast cooling rate favored the formation of these particles. Particle spheroidization has been previously observed in studies conducted with Al_2O_3 particles *(Fan et al, 1998)* in RF-thermal plasma.

3. Angular and cubic (crystal-like) particles: These were non porous particles that were either agglomerated forming a cluster or large crystals forming single units. These structures were observed in all samples in the 0.1 to 1 μm range in different amounts (Fig. 5.1). There were predominantly present in the CeO_2 sample as observed in Fig. 5.2e. These particles resulted from particles solidifying at a relatively slow cooling rate, sufficiently slow to promote crystalline angular particles.

4. Loose nanoparticle agglomerates: Nanoparticles were also present in all the samples in different amounts as shown in Fig. 5.2a-f. The nanoparticles were all particles less than 100 nm or 0.1 μm (Fig. 5.1) and all presented crystal-like structure (Fig. 5.2f), mostly cubical. The complete deagglomeration of these particles was not possible due to their strong surface interaction even after sonication in a dispersant liquid. These particles probably resulted from two different possible formation mechanisms. The first involved material condensation from the vapor phase followed by particle nucleation and growth. The second was when fine atomized droplets were calcined, melted and later solidified into angular shapes; in this case, the particles never reached the vapor phase.

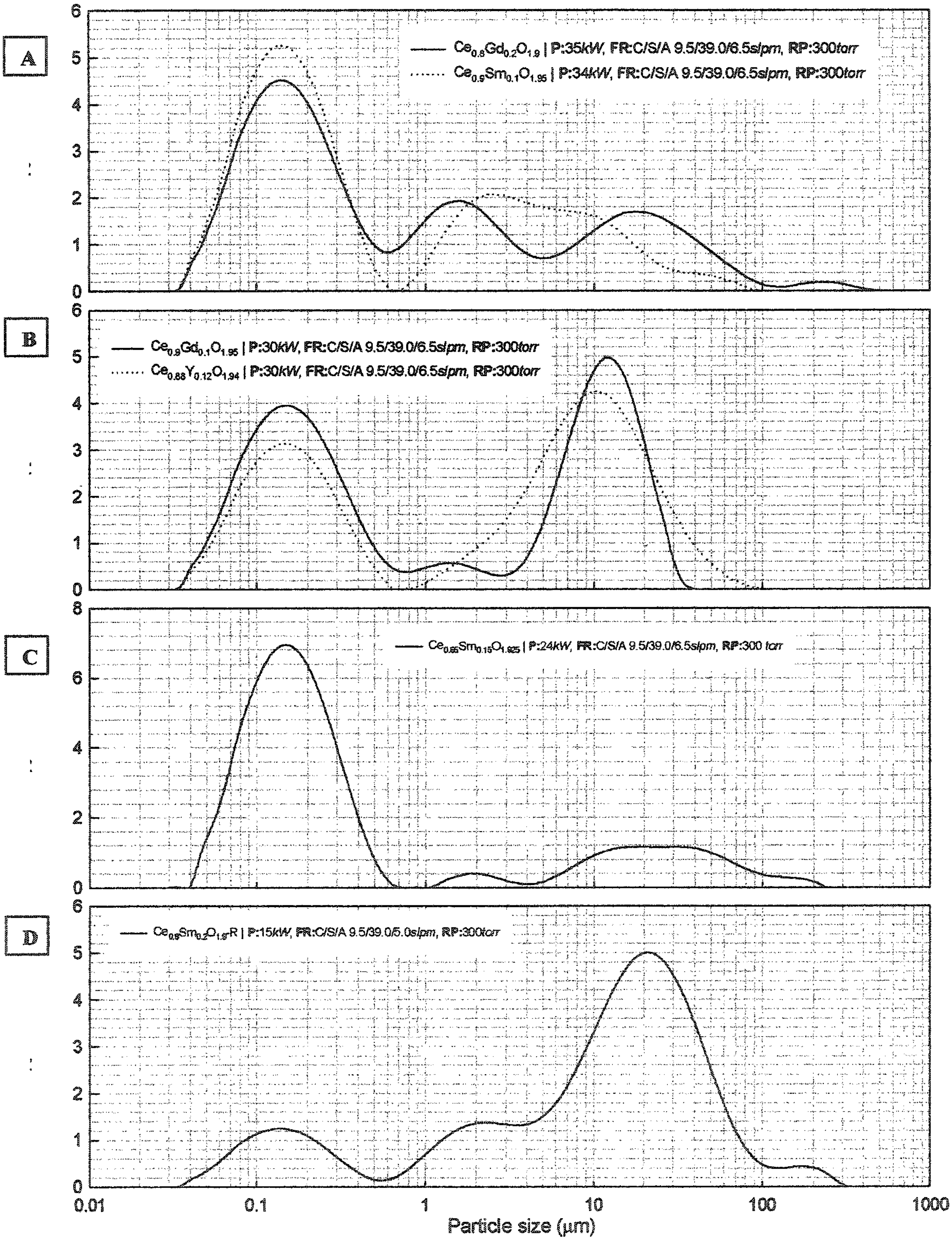

Figure 5.1 Particle size distribution of selected synthesized oxide powders using laser diffraction

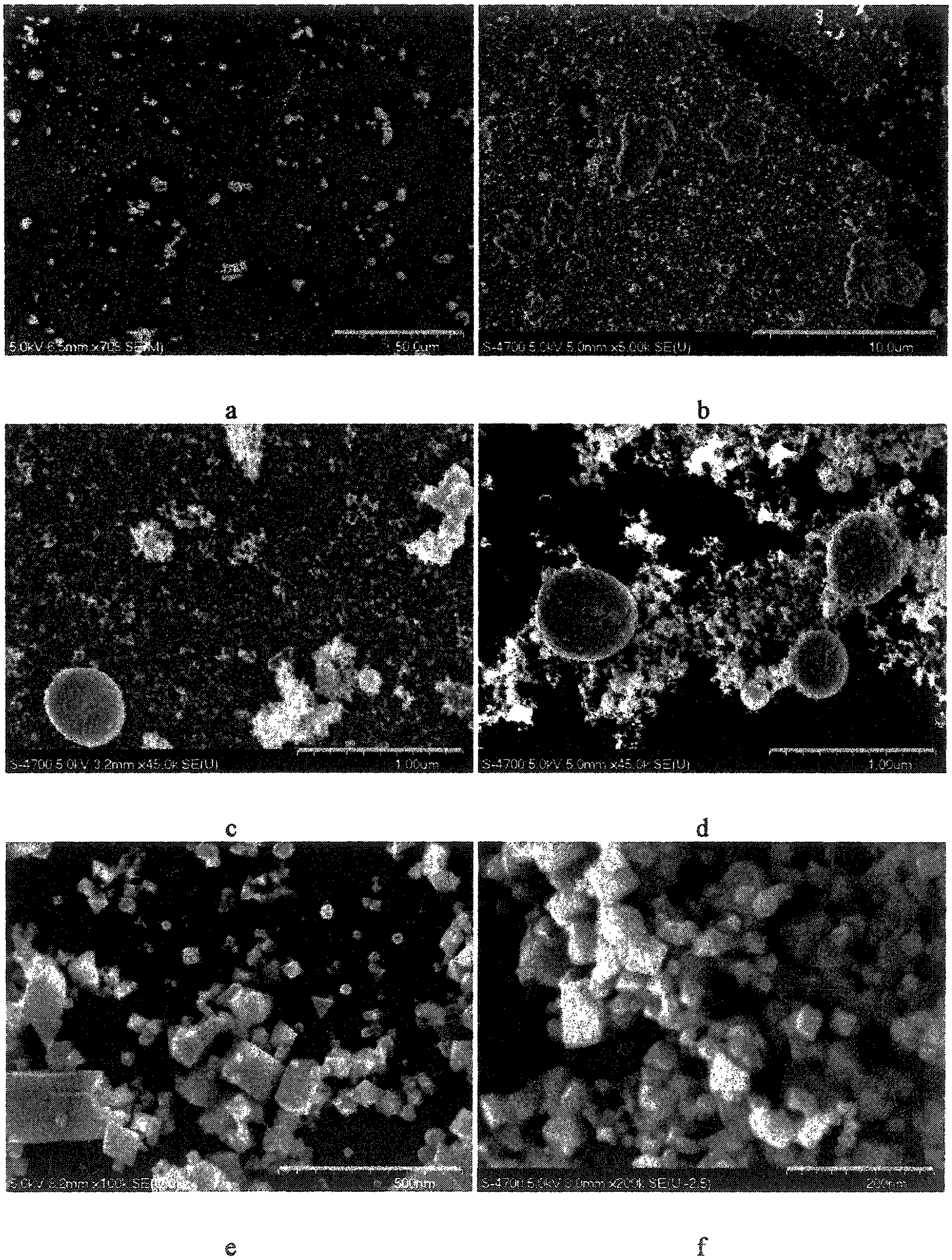

Figure 5.2 SEM micrographs of a) $Ce_{0.9}Gd_{0.1}O_{1.95}$, b, c) $Ce_{0.8}Sm_{0.2}O_{1.9}$-R, d) $Ce_{0.88}Y_{0.12}O_{1.94}$, e) CeO_2, f) $Ce_{0.8}Sm_{0.15}O_{1.9}$,

A schematic figure showing the different types of oxide particles and the corresponding temperatures at which they were probably formed is given below (Fig. 5.3). The nanoparticles were formed at two different temperatures. Noted that all particles exceeded the calcination temperature (T_r). Further, the shape of the synthesized particles was greatly dependent on the size of the atomized droplet and on the rate of cooling when particles were formed.

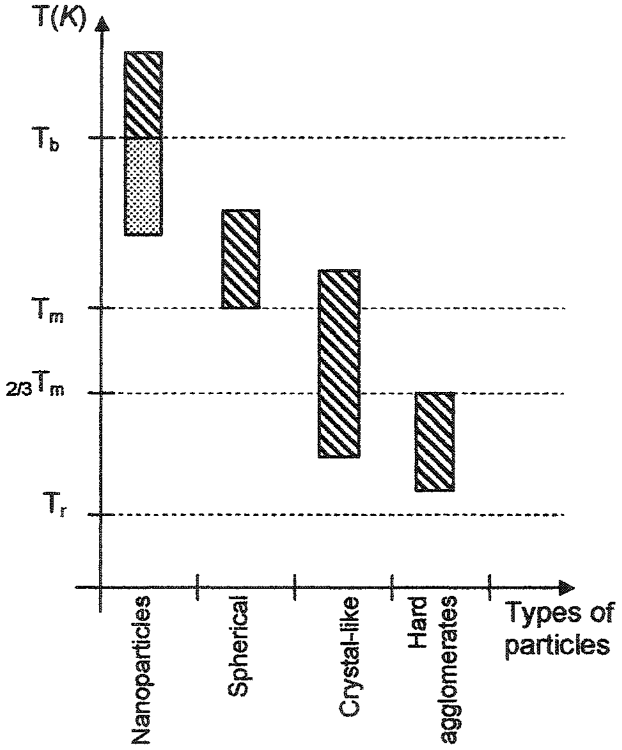

Figure 5.3 Schematic temperature histories of the different types of particles (T_b: boiling temperature, T_m: melting temperature, T_r: reaction or calcination temperature)

5. B Effect of selected plasma operating parameters and collection regions on product size

5.B.1 Effect of selected plasma operating parameters on product size

The plate power definitely affected the particle size distribution and more hard and porous agglomerates (i.e. modes located in the > 10 μm range) were obtained as the plate power decreased (these experiments were done keeping gas and liquid feed rates constant) (Fig. 5.1). This trend was not followed by the samples synthesized at 30 kW (Fig. 5.1b). Imperfect particle dispersion prior to measuring particle size was believed to be the cause of this unusual behavior. Hard agglomerates were present at all different plasma powers and were predominant at the lowest power, i.e. 15 kW, possibly as a result of being the only sample in which nitrates were detected (i.e. from the EDS analysis). However, since hard agglomerates were present in samples that showed no traces of nitrates, the presence of hard-agglomerates did not constitute a proof of poor calcination. Hard agglomerates could arise as a consequence of semi molten and fully calcined particles colliding and not only because insufficient energy was available for reaction. The presence of spherical and crystal like particles in the 0.1 to 1 μm range augmented as the plasma power increased, indicating that higher plate powers promote particle spheroidization and densification.

Different plasma operating parameters were investigated for the plate power that had produced the lowest amount of hard-agglomerates (i.e. 25 kW) (Fig. 5.4a). In general, there was very little change regarding the particle size distribution when the reactor pressure and the central gas flow rate were changed. It would be adventurous to draw conclusions based on the few experiments carried out because changing the reactor pressure and the central gas flow rate affected both the particle residence time and the plasma enthalpy. Few experiments were carried because of the limited time that the experimental equipment was available for operation at the CRTP Sherbrooke.

Having a lower reactor pressure increased the particle velocity (*Coulombe, 1994*) thus decreasing the particle residence time, but at the same time, low pressure enlarged the plasma plume and increased the zone in which the particles could be in contact with the plasma. These two opposing trends may have cancelled out with the net effect of an apparent unvarying particle size distribution. Low chamber pressures are needed to prevent the backflow of particles injected in the plasma. This low pressure allows the particles and droplets to retain a sufficient initial momentum to penetrate the reverse flow associated with the top of the high-temperature zone of the plasma and to promote axial droplet and particle trajectories close to the centerline of the torch *(Fan et al, 1998)*. Higher central gas flow rates could favor the interaction between the particles and the plasma because the plasma volume was increased, promoting particle coalescence. But in doing so, the plasma enthalpy was lowered which may retard particle calcination and densification (the plate power was kept constant in these experiments).

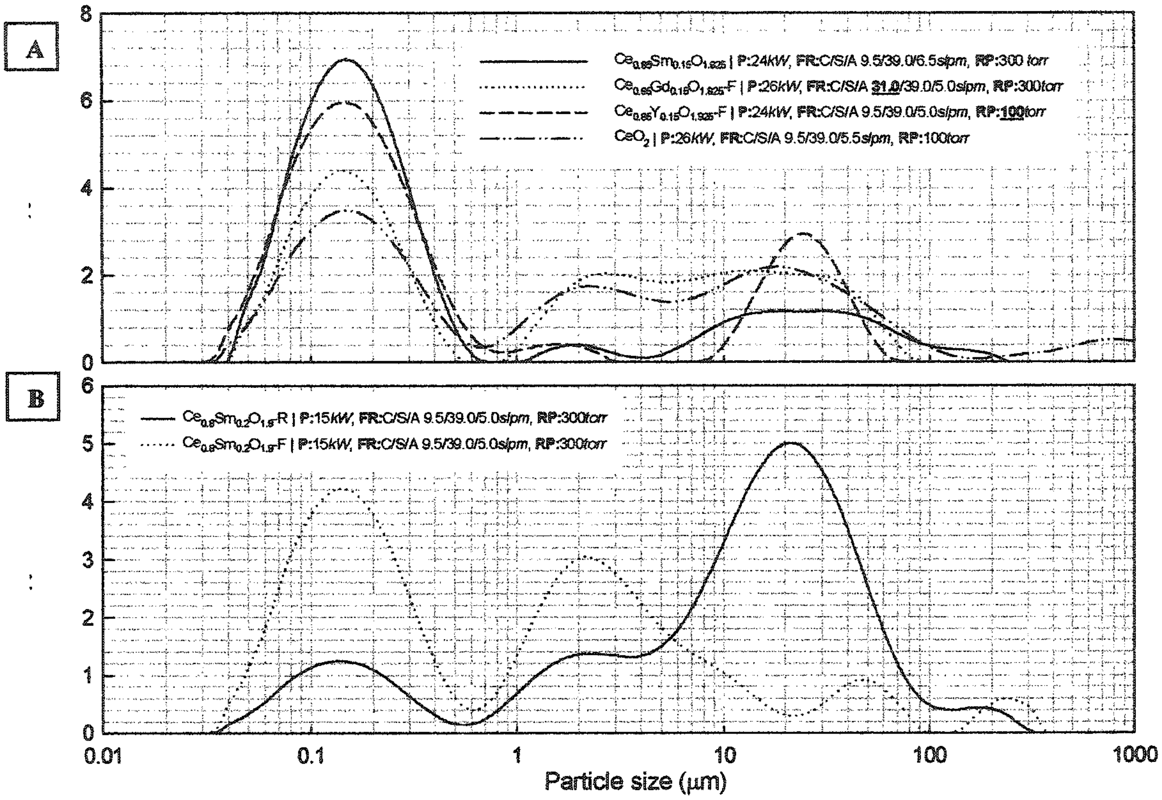

Figure 5.4 a) Comparison of different operating parameters for selected synthesized powders at 25 kW; b) PSD of samples from two different collection regions

5.B.2 Effect of collection regions on product size

The results showing the different particle size distributions of particles collected from the main reactor walls and those collected from the metallic filters are shown in Fig. 5.4b. Two distinct PSD were observed as a result of different particle collection mechanisms that will be explained later in this chapter. The comparatively larger hard-agglomerates were deposited at the bottom of the first collector and the smaller nanoparticles and spherical particles followed the gas stream until the particles were collected at the filters.

5. C Study of nanopowder distributions (SEM image analysis)

Although, the laser diffraction technique used to measure the particles size distribution of these samples was a powerful tool, it was not adequate to measure the small loosely agglomerated nanoparticles. Therefore, a quantitative method (i.e. the in-house PSD software) was developed to determine the particle size distribution of these nanoparticles based on the SEM images acquired of the different synthesized particles. In doing so, a complete overview of the different types of powders produced using the plasma synthesis method was now possible.

The results of the image analysis method using the in-house software are presented in Fig. 5.5 and summarized in Table 5.1. The parameters displayed in this table were calculated from the best fit of a log-normal distribution of the truncated raw data. The original PSD obtained by the in-house software was truncated for reasons explained earlier (chapter 3).

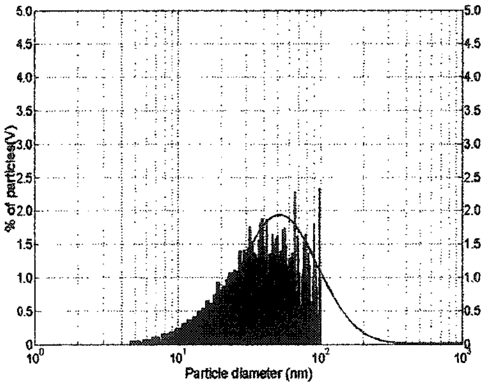

$Ce_{0.8}Gd_{0.2}O_{1.9}$

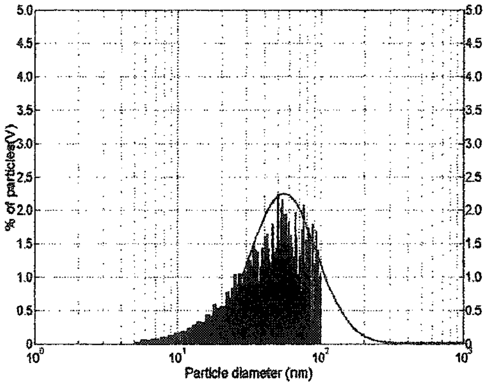

$Ce_{0.9}Sm_{0.1}O_{1.95}$

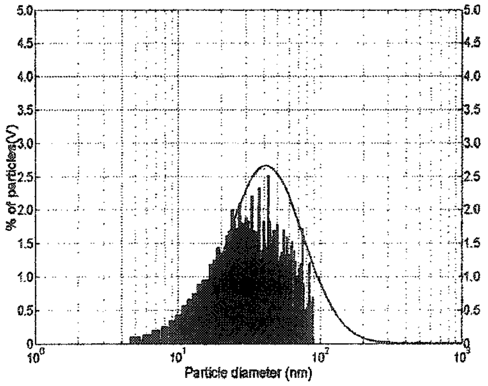

$Ce_{0.9}Gd_{0.1}O_{1.95}$

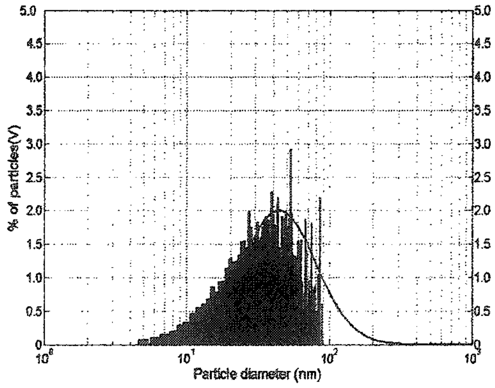

$Ce_{0.88}Y_{0.12}O_{1.94}$

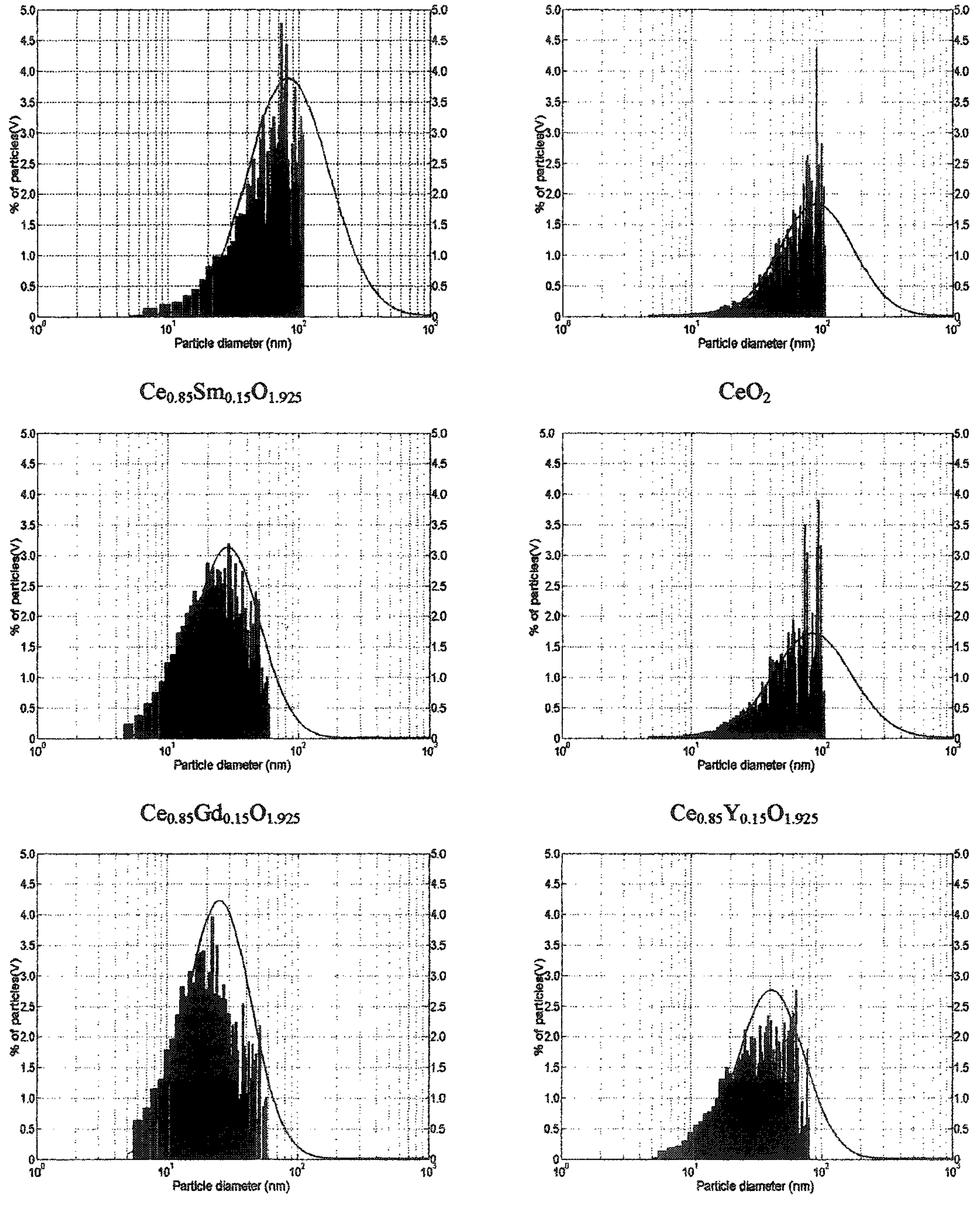

$Ce_{0.85}Sm_{0.15}O_{1.925}$ CeO_2

$Ce_{0.85}Gd_{0.15}O_{1.925}$ $Ce_{0.85}Y_{0.15}O_{1.925}$

$Ce_{0.8}Sm_{0.2}O_{1.9}$-R $Ce_{0.8}Sm_{0.2}O_{1.9}$-F

Figure 5.5 Particle size distribution of the synthesized samples based on their SEM micrographs using the in-house PSD software

The fit was good as observed by the overlaying proximity of the continuous curve to the histogram data for the volume-based particle size distributions. A Bartlett's statistical test (*Mason et al, 1989*) (see appendix A) was conducted to test the hypothesis of equal error in standard deviations for samples from more than two populations or processes. A B=434 was obtained for all the Sm samples and the 15% Gd sample and a *B*=171 was calculated for the remaining samples. The level of significance assumed was α=5% with 4 degrees of freedom. A t-statistical test (α=0.05) (see appendix A) was performed to compare the Dv_{50} values of samples synthesized at the same power. The results were t=345, 247 and 1,371 for 35, 30 and 15 kW respectively and 3,764 and 266 for 25 kW. All values clearly exceeded the t-critical value of 1.960. These results lead to the conclusion that each of the standard deviations as well as Dv_{50} values presented in Table 5.1 belonged to different and distinguishable populations, despite their apparent closeness. The central gas flow rate was changed for the 15% Gd sample and the reactor pressure was modified for the 15% Y sample with respect to the base case operating conditions.

Table 5.1 Volume based median and standard deviation values calculated from the PSD obtained from the in-house software for different synthesized conditions

Power [*kw*]	**Synthesized product**	**Base case operating conditions FR: 9.5/39.0/5.0-6.5 *slpm*; RP: 300 *torr***	**Dv[50] [*nm*]**	**σ**
35	$Ce_{0.8}Gd_{0.2}O_{1.9}$-R	Same as in base case	51.3	0.62
	$Ce_{0.9}Sm_{0.1}O_{1.95}$-R	Same as in base case	54.5	0.53
30	$Ce_{0.9}Gd_{0.1}O_{1.95}$-R	Same as in base case	41.3	0.60
	$Ce_{0.88}Y_{0.12}O_{1.94}$-R	Same as in base case	43.7	0.60
25	$Ce_{0.85}Sm_{0.15}O_{1.925}$-R	Same as in base case	82.9	0.72
	$Ce_{0.85}Gd_{0.15}O_{1.925}$-R	FR: 31.0/39.0/5.0 slpm	28.5	0.57
	$Ce_{0.85}Y_{0.15}O_{1.925}$-F	RP: 100 torr	83.6	0.70
	CeO_2-R	Same as in base case	89.7	0.65
15	$Ce_{0.8}Sm_{0.2}O_{1.9}$-R	Same as in base case	24.8	0.57
	$Ce_{0.8}Sm_{0.2}O_{1.9}$-F	Same as in base case	40.9	0.58

The volume PSD measurements characterized by the median values and standard deviations were very close for samples synthesized under the same experimental conditions which confirmed the good reproducibility for experiments conducted under the same plasma conditions (Table 5.1). The Dv_{50} values of all the samples were also within the same order of magnitude as the estimated crystallite sizes obtained from the X-ray diffraction patterns (~20-40 nm). This indicated that the size of the nanoparticles closely corresponded to the size of individual crystals.

The Dv_{50} values of powders collected from the reactor walls (labeled "R") did not show a clear distinction for doped samples synthesized under the base case conditions at plate powers greater than 25 kW, i.e. 10 and 20% Gd, 10 and 15% Sm, and 12% Y (the minimum value was 41.3 and the maximum 82.9 nm). However, the 20% Sm sample at 15 kW did show a considerably lower Dv_{50} value, i.e. 24.8 nm. These results were in agreement with the PSD results obtained with laser diffraction (Fig. 5.1) in which the patterns obtained for samples synthesized at 25 kW was not significantly different, especially in the < 0.1 µm range. However, these patterns did show an appreciable difference compared to the pattern of the 15 kW-synthesized sample.

The nanoparticles collected at the metallic filters were larger than the ones collected from the reactor walls for the lowest power sample, i.e. 20% Sm. The different particle collection mechanisms were responsible for this phenomenon; smaller particles would tend to deposit on the reactor walls (this will be later explained at the end of this chapter). Two extreme cases of this behavior are illustrated in Fig. 5.6.

There was not sufficient experimental evidence to conclude about the effect of changing the reactor pressure or the plasma flow rate. But it was experimentally observed that the majority of the particles were collected at the metallic filters when the reactor pressure was lowered as result of the stronger vacuum. Also, a larger number of small particles were collected from the main reactor when the plasma gas flow rate was increased in comparison with samples produced under the base case conditions. Further investigation is required to explain this behavior.

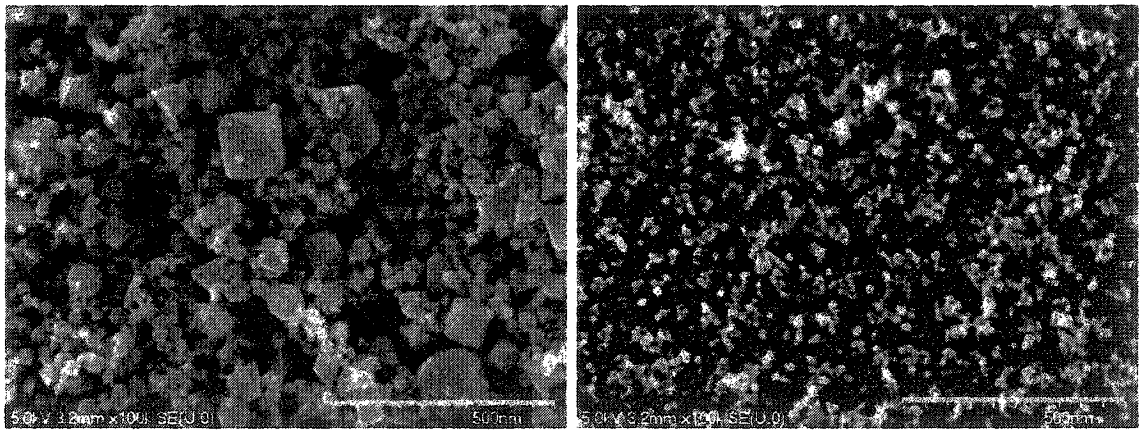

A b

Figure 5.6 a) 15% mole Y powders collected from the metallic filters; b) 15% mole Gd powders collected from the main reactor walls

5. D Proposed mechanism of powder formation

A modified particle formation mechanism for RF-ICP thermal plasma synthesized oxide particles starting from liquid precursors is proposed. The first mechanism was suggested by Bouyer (*Bouyer et al, 1997*). According to Bouyer's mechanism, the size distribution of the final oxide powders could be predicted by mass balance and density data, assuming a final particle shape, either angular or spherical, complete water evaporation and full calcination of the droplet. However, experimental evidence from laser diffraction measurements, in-house PSD software and SEM micrographs discussed below contradicts Bouyer's mechanism. This evidence is the following: 1) no spherical oxide particles of size predicted (i.e. no 10 μm particles from 30 μm atomized droplets), 2) some spherical particles but of much smaller diameter, i.e. 0.1 to 1 μm, 3) some larger particles but mostly hard agglomerates (1 to 20 μm), 4) most particles of angular or crystal-like shape, generally cubical, 5) many nanosized particles and finally 6) all synthesized samples were fully calcined (with the exception of the one synthesized at 15 kW). Based on these findings a new model is proposed and it is compared to Bouyer's in Fig 5.7.

Two parallel and different reaction paths starting from the original sprayed droplets have been hypothesized. First, fine atomized droplets of a given critical size followed Bouyer's model up to the calcination step. After this point, if the oxide particles were in sufficient contact with the plasma, they would vaporize and later condense into the most stable structure which seemed to be the typical cubic fluorite structure. If not in sufficient contact with the hot plasma, vaporization did not occur, and the particles solidified into angular or cubic-like structures. These particles, if partially molten, would be prone to form hard agglomerates upon collision (left branch of the proposed mechanism in Fig. 5.7).

Second, the decrease in predicted particle size and the great number of small particles obtained suggested that droplet explosion occurred. Droplet explosion could occur through crust formation or droplet superheating. Crust formation was a result of the rapid water evaporation at the droplet surface. This caused the solute to precipitate out of solution and form a crust. The crust finally collapsed as a result of buildup of vapor pressure from water being evaporated inside the droplet. Evidence of reaction burst particles in the production of Y_2O_3 stabilized ZrO_2 from nitrate and chloride salts have been reported before *(Dubais et al, 1989)*. Droplet superheating was the collapse of a droplet as a result of violent water evaporation. After droplet explosion some particles would be of the adequate size to undergo the reaction mechanism proposed by Bouyer; therefore forming spherical and dense particles of much smaller sizes than those predicted. Also after explosion, some other particles could form crystal-like or angular structures once cooled from liquid droplets. These particles were typically smaller than spherical particles, and could be prone to form hard agglomerates upon collision, if partially molten. A fast cooling rate would favor the formation of spherical particles and a slow cooling rate would promote angular ones (center and right branch of the proposed mechanism in Fig. 5.7).

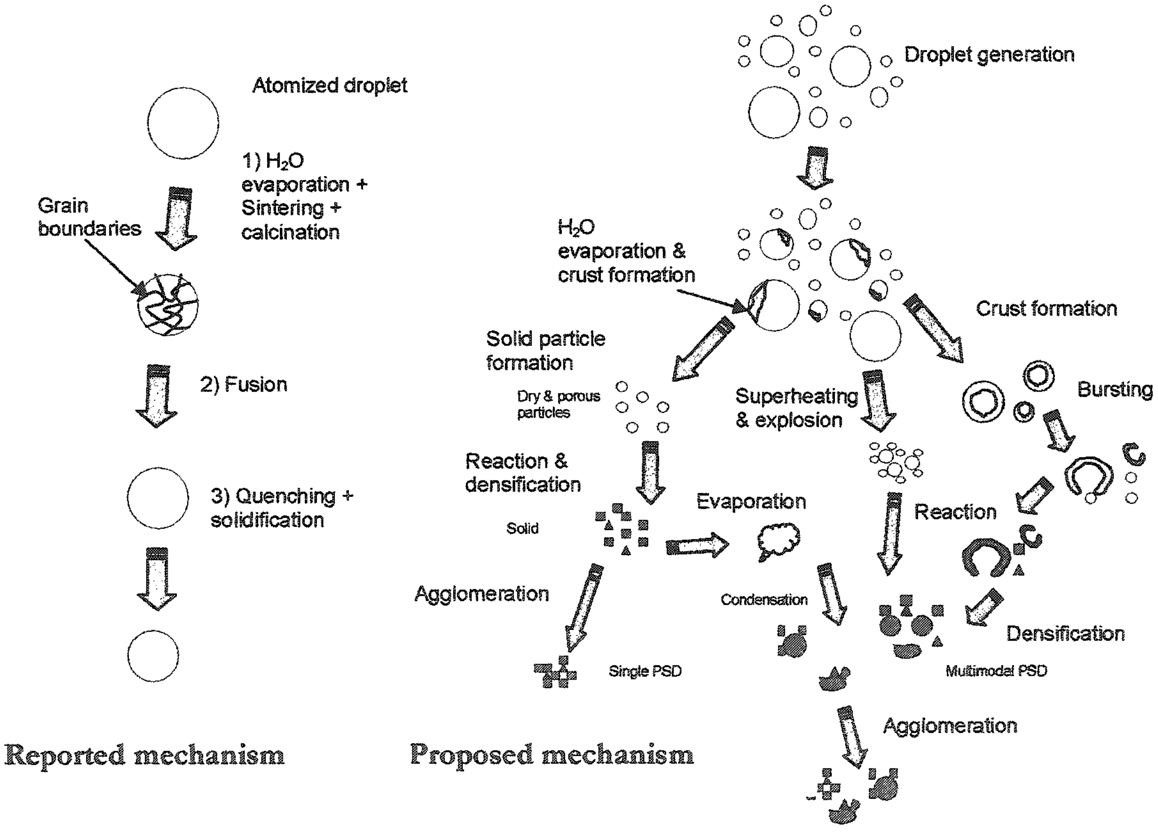

Figure 5.7 A modified particle formation mechanism for RF-ICP thermal plasma synthesized particles starting form liquid precursors

In summary, the solid particle formation mechanism shown in Fig. 5.7 illustrates the probable paths for the conversion of liquid droplets into solid particles, from the moment the droplets come into contact with the plasma until the moment at which solid particles exit the plasma tail flame. A rigorous treatment of the droplet-particle formation mechanism requires a more detailed study of the physical phenomena occurring in the plasma system, such as: a comparison of the rates of heat consumption (the latent heat of evaporation of the solvent and the heat of reaction to form oxides from nitrates) and the heat transfer into the droplet, a temperature history of particle formation and solidification, oxide vaporization and vapor condensation, etc. The mechanism proposed in this work is a step forward from the relatively simple synthesized route previously reported and aims for a more complete understanding of the phenomena associated with particle formation from liquid precursors. Many attempts have been made to describe the plasma-particle interactions of oxide particles in plasma environments but unfortunately they did not study liquid precursors (*Proulx et al, 1985; Ramachandran, et al, 1996; Sobolev, et al 1999; Ramasamy et al 2001*)

5. E Study of particle collection mechanisms

Particles were collected from different locations in the reactor and it was observed that not all the types of particles discussed previously were obtained in similar amounts at all locations. Table 5.2 gives a summary of the findings. The reasons for these discrepancies can be explained by the different collection mechanisms which operated on the particles at different locations in the system. The four most probable collection mechanisms operating in the reactor system were thermophoresis, Brownian diffusion, turbulent diffusion and inertia.

Table 5.2 Predominant particle collection region for the different types of particles

Collection region/Types of particles	Hard-agglomerates	Spherical particles	Crystal-like particles	Nanoparticles
A1: Main reactor upper wall	Yes	Yes	Yes	Yes
A2: Main reactor lower wall	No	Yes	Yes	Yes
B: Main reactor collector	Yes	No	No	Yes
C: Secondary reactor wall	Yes	Yes	Yes	Yes
D: Metallic filters	No	Yes	Yes	Yes

Thermophoresis acts on very small particles in the presence of strong thermal gradients and causes the particles to move down the thermal gradient. Thermophoresis is caused by the greater momentum of gas molecules bombarding the particle on the hotter side of the particle. In the present case, the small spherical and crystal-like particles as well as the nanoparticles would be driven to the cold reactor wall from the hot plasma gas. Since the velocities produced by thermophoresis are typically small, the particles and hot gas would first have to be brought into the vicinity of the wall by bulk flow. The expansion of the plasma jet into the top of the reactor gives rise to a recirculating flow which accomplishes this transfer.

The collection mechanisms of Brownian and turbulent diffusion would also act near the walls in the vicinity of the recirculating flow, acting again on the smaller particles. Brownian diffusion results in a net particle transport from regions of high to low concentrations due to the fluctuating forces exerted on them by the surrounding molecules (*Friedlander, 2000*). These two mechanisms would become the primary means of collection in the lower parts of the first reactor, where thermal gradients become relatively small, and in the second chamber. Brownian diffusion would be a major mechanism in the filter, assisting in the capture of the smallest particles on a bed of previously captured particles.

Inertial impaction, or simply inertia, caused capture when there is a sudden change in flow direction and the particles cannot follow the flow streamlines. It would be effective in the upper recirculating zone where the gas flow is towards the wall or upper flange of the reactor. It would act primarily on larger particles, i.e. hard-agglomerates. It would also act on larger particles where the gas flow turns by 90° at the bottom of the first chamber leading to capture in the main reactor collector and along the wall opposite to the gas entry in the second collection chamber. Finally, inertial impaction would be an important collection mechanism on the metal filter for all but the nanoparticles as the gas flows through a tortuous path in the bed of captured particles and the filter medium.

Figure 5.8 summarizes the locations of these collection mechanisms and the results in Table 5.2 are consistent with this interpretation.

Figure 5.8 Different physical phenomena affecting particle collection

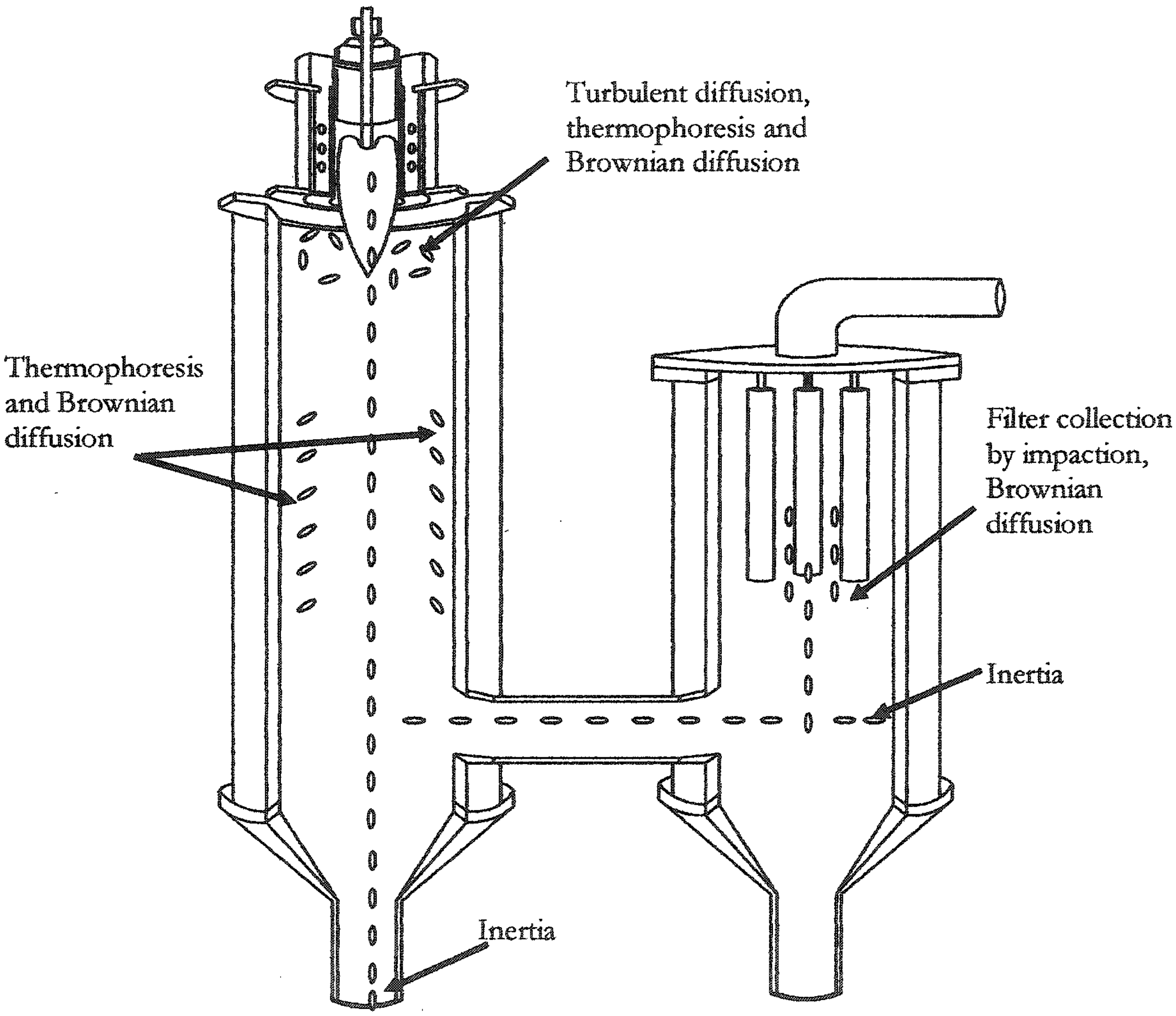

Chapter 6 Conclusions, future work and recommendations

6. A Conclusions

The following conclusions were obtained from this study:

a) It was determined from a review of the literature that the addition of 10 to 20% mol of Gd, Sm or Y would provide the CeO_2 with the maximum ionic conductivity and stability as electrolyte material for SOFC operation.

b) Nitrate salts were chosen as the most suitable raw materials compared to chlorides, hydroxides and organometallic compounds based on their low cost, minimal production of comparatively less hazardous byproducts and high water solubility.

c) The synthesis of fine oxide powders ($Ce_{1-x}Me_xO_{2-x/2}$) of different dopant compositions (Me=Gd, Sm and Y) from nitrate salts dissolved in water using radio frequency inductively coupled plasma was demonstrated.

d) Solution atomization using an air-blast Tekna atomizing probe was shown to be a reliable and reproducible way to obtain narrow droplet size distributions centered over a given droplet diameter value. Adequate droplet atomization was achieved varying atomization parameters such as atomizing probe opening, gas flow rate and liquid flow rate. It was found that probe opening and gas flow rate had major effects.

e) The synthesized powders retained the metallic elemental composition of the injected solutions (within a 5% error) as demonstrated by the ICP measurements and could be fully calcined (within a N detection limit of 5-10%) as shown by EDS analyses.

f) The synthesized powders exhibited a high degree of crystallinity and purity. The X-ray diffraction patterns for all the samples closely resembled the pattern of pure CeO_2 in terms of peak location and relative intensity. This was obtained for all the samples independently of the plasma operating parameters and of the choice of dopant. Further, the amount of dopant added for a given dopant did not affect the basic CeO_2 crystalline lattice. This finding contradicted the results reported in the literature in which similar oxide powders were synthesized using conventional sol-gel and sintering methods. It is probable that the plasma synthesized particles would serve as better electrolyte material since the CeO_2 lattice was less distorted. Based on this, a superior performance of the electrolyte layer is expected (once formed and tested in actual SOFC operation).

g) The powders showed a crystallite size ranging from 20 to 40 nm that was independent of plasma operating parameters, choice of dopant and dopant amounts. However, larger crystals (i.e. 40-60 nm) were obtained when pure CeO_2 was synthesized, suggesting that dopant addition retarded CeO_2 crystal growth.

h) The EDS analysis showed that cross-contamination was avoided in the plasma synthesis route. The calcination efficiency was independent of other plasma operating parameters such as reactor pressure and central gas flow rate within the range examined.

i) The SEM micrographs showed three different particle types and size distribution ranges that were later confirmed using laser diffraction to measure particle size. There were hard agglomerates of 1 to 20 μm, dense spheres and agglomerates of 0.1 to 1 μm and nanoparticles of less than 0.1 μm. These three particle distribution ranges were found in all samples in different amounts and varied with plasma operating parameters, but were independent of both the choice and the amount of dopant added.

j) Plasma plate power had a strong effect in the amount of the different types of particles. At lower powers more hard agglomerates were found and at higher powers more dense spherical and cubical-like structures were identified at the same collection region. Higher plasma powers favored droplet superheating and explosion and probably promoted the collision and densification of particles into spherical and cubical shapes. Changing the reactor pressure and varying the plasma gas flow rate had little or no apparent effect on particle synthesis as a result of competing phenomena, i.e. particle residence time, plasma plume length and plasma power within the range studied. However, further research is required to expand on the effect of plasma parameters on PSD to arrive at more conclusive remarks.

k) A novel particle size distribution measurement method (PSD) based on image analysis was developed to measure agglomerated nanoparticles. The algorithm used exploited the fact that in SEM micrograph individual nanoparticles possessed similar grey level values that allow the identification of particle boundaries. The grey level intensities could be obtained at each pixel and thus measure particle lengths from one particle boundary to another. The algorithm allowed a quick way to count a large number of particles, and thus offer the possibility of generating both a number PSD and a volume PSD with statistical significance.

l) A new particle formation mechanism was proposed based on the findings reported in the literature and the experimental results obtained. It was concluded that droplet explosion was responsible of the decrease in expected particle size and that Bouyer's mechanism was not the primary particle formation model. The proposed mechanism accounted for all the different types of particles observed. Four different particle collection mechanisms in the plasma system were discussed, i.e. thermophoresis, Brownian diffusion, turbulent diffusion and impaction (due to particle inertia).

6. B Future work and recommendations

The production of SOFC components or SOFC materials using RF-thermal plasma technology has a great potential based on the facility to prepare all the components/materials by accurately controlling their composition, plasma operating parameters and plasma method, i.e. solution or suspension plasma synthesis/spraying or thermal plasma vapor deposition. A proper selection of the method and material compositions offers the possibility to synthesize and/or spray oxide powders of excellent quality at high rates. Therefore, the use of RF-plasma is highly recommended. A list of more specific recommendation and future work is now presented:

1) The formation of electrolyte layers from the synthesized particles must be carried out to compare the performance of an electrolyte layer composed of plasma synthesized

particles with the performance of an electrolyte layer composed of powders synthesized using other methods, especially sol-gel followed by sintering. The electrolyte layers could be formed by using suspension plasma spraying or by compressing the powders under heat. In doing so, the best electrolyte materials, i.e. the most suitable dopant and dopant amount, could be determined.

2) The effect of different plasma operating parameters on particle size distribution (PSD) must be further investigated. More experiments must be conducted at lower reactor pressures (i.e. 100 torr) as well as at higher pressures (i.e. 500 and 700 torr). The gas flow rate must also be varied to higher values (i.e. greater than 30 slpm). These experiments will provide more experimental evidence towards a final conclusion of the effect of plasma operating parameters on PSD.

3) The synthesis of particles of a single PSD must also be further investigated. The importance of having a single PSD lies on the fact that coating uniformity will be greatly improved as only a small particle size range will be deposited. A new reactor system that allows particle collection in-flight at several reactor locations will provide experimental information of the particle size at different trajectory regions. This information must be used as a feedback to tune the plasma operating parameters. Varying the plasma operating parameters alone may not be sufficient to obtain a single PSD and thus other methods must be examined, i.e. modifying the solution or suspension characteristics or implementing equipment that selectively deposits or screens for particles of a given size range

4) The particle dispersion for both laser diffraction and SEM analyses must also be improved. The use of DMF was very successful but there could be other solvents and/or dispersant agents that will provide a better particle de-agglomeration.

5) Recently, lanthanum gallate, $LaGaO_3$, doped with strontium and gallium has attracted considerably attention as this electrolyte does not show the problems exhibit by CGO (cerium gadolinium oxide) at the temperatures between (500-600 °C) and the ionic conductivity of a favored composition (i.e. $La_{0.9}Sr_{0.1}Ga_{0.8}Mg_{0.2}O_{2.85}$) is just slightly less than CGO at 500 °C (*Ormerod, 2003*). However, there are problems associated to prepare pure

single phase electrolytes of LSGM and additional phases including $La_4Ga_2O_9$ and $SrLaGa_3O_7$ have been detected at the grain boundaries. It is possible that the thermal plasma synthesis of this material will provide better results than those obtained with sintering methods. In doing so, new electrolyte materials could also be investigated.

References

A Dictionary of Physics. Oxford Reference Online. Oxford University Pres. <http://www.oxfordreference.com/views/ENTRY.html?subview=Main&entry=t83.002997> (2003)

Aristizabal, F. "Modeling of the generation of ultra fine aluminum particles from the quench of superheated vapour in turbulent flow". *Master Thesis.* McGill. Canada. p. 156 (2002)

Badwal, S. P. S., Ciacchi, F. T., Drenan, J. "Investigation of the stability of ceria-gadolinia electrolytes in solid oxide fuel cell environments". *Solid State Ionics.* Vol. 121. pp 253-262. (1999)

Bauerle, J. E. "Solid electrolyte polarization by a complex admittance method". *Journal of Physics and Chemistry of Solids.* Vol. 30. pp. 2657. (1969)

Bernhardt, C. Particle Size Analysis. "Classification and sedimentation methods". 1st Ed, Chapman & Hall. 430 p. (1994).

Bonneau, M. E. « Déposition d'électrolyte de type fluorite pour les SOFC en utlisant la projection de suspensions par plasma ». *Maîtrise.* Sherbrooke, Canada. p. 103 (2001)

Boulos, M. I. "RF induction plasma spraying: State-of-the-art review". *Journal of Thermal Spray technology.* Vol. 1. pp 33-40. (1992)

Boulos, M. I. "Thermal plasma processing". *IEEE Transactions on Plasma Science.* Vol. 19. No. 6. p. 1078 (1991)

Bouyer, E., Gitzhofer, F., Boulos, M. I. "Suspension plasma spraying for hydroxyapatite powder preparation by RF plasma". *IEEE Transactions on Plasma Science.* Vol. 25. No. 5. pp. 1066-1072. (1997)

Bouyer, E., Muller, M., Henne, R. H., Schiller, G. "Thermal plasma processing of nanostructured Si-based ceramic materials'. *Journal of Nanoparticle Research.* Vol. 3. pp. 373-378 (2001)

Bouyer, E., Schiller, G., Muller, M., Henne, R. H. "Thermal plasma chemical vapor deposition of Si-based ceramic coatings from liquid precursors". *Plasma Chemistry and Plasma Processing.* Vol. 21. No. 4. pp. 523-546 (2001)

Chen, Y., Liang, Y., Zheng, F., Zhou, R., Feng, Z. "The dispersion behavior of Si-C-N nanopowders in organic liquids". *Ceramics International.* Vol. 27. pp. 73-79 (2001)

Coulombe, S. « Diagnostic des particules en vol dans un plasma inductif ». *Master Thesis.* University of Sherbrooke. Canada. p. 92. (1994)

CRC 83rd Handbook of chemistry and physics. Online. http://www.hbcpnetbase.com/

Cullity, B. D., Stock, S. R. "Elements of X-ray diffraction". 3rd Ed. Prentice Hall. USA. 664 p. (2001)

De Carolis, S. Pascual, J. L. Pettersson, L. G. M. Baudin, M. Wojcik, M. Hermansson, K. Palmqvist, A. E. C. Muhammed, M. "Structure and electronic properties of Ca-doped CeO2 and implication on catalytic activity: an experimental and theoretical study ". *J. Phys. Chem. B.* 103(36). pp. 7627-7636 (1999)

Delbos, C., Fazilleau, J., Coudert, J. F., Fauchais, P., Bianchi, L., Wittmann, K. "DC plasma spray elaboration of fine structured coatings by ceramic liquid suspension injection". Abstract and full papers. *16th International Symposiun on Plasma Chemistry (ISPC-16).* Italy. (2003)

Dubois, B., Ruffier, D., Odier, P. J. "Preparation of fine, spherical yttria stabilize zirconia by the spray pyrolysis method". *Journal of the American Ceramic Society.* Vol. 72(4), pp. 713-715 (1990)

Eguchi, K. "Ceramic materials containing rare earth oxides for solid oxide fuel cell". *Journal of Alloys and Compounds.* Vol. 250. pp 486-491 (1997)

El-Adham, K., Gadai, M. "Decomposition of some cerium salts and crystallite size of ceric oxide products". *International Ceramic Review.* Vol. 26(3). pp.223-226. (1977)

Fan, X., Gitzhofer, F., Boulos, M. "Statistical design of experiments for the spheroidization of powdered alumina by induction plasma processing". *Journal of Thermal Plasma Technology.* Vol. 7. June. pp. 247 (1998)

Friedlander, S. K. "Smoke, dust and haze: fundamental of aerosol dynamics". Oxford University press. Oxford. p. 680 (2000)

Gilman, W. S., Seabaugh, P. W., Sullenger, D. B. "Stable substoichiometric cerium oxide formed in an air plasma." *Science: New Series.* Vol. 160. No. 3833. p. 1239 (1968)

Gitzhofer, F., Boulos, M., Heberlein, J., Henne, R., Ishigaki, T., Yoshida, T. "Integrated fabrication processes for solid-oxide fuel cells using thermal plasma spray technology". *MRS Bulletin.* Vol. 25. No. 7. pp. 38-42. (2000)

Gödickemeier, M., Sasaki, K., Gauckler, L. J., Riess, I. "Perovskite cathodes for solid oxide fuel cells based on ceria electrolytes". *Solid state ionics.* Vol. 86-88. pp. 691-701. (1996)

Goldstein, J et al. "Scanning electron microscopy and X-ray microanalysis: a text for biologist, material scientists and geologists". 2nd Ed. Plenum. USA. 820 p. (1992)

Guo, J. Y., Gitzhofer, F., Boulos, M. I., Ishigaki, T., and Mieno, M. "Study of the Sintering Properties of Plasma Synthesized Ultrafine SiC Powders". *Journal of Materials Science Letters* 32. pp. 5257-5269 (1997).

Gutierrez S. and Gitzhofer F. "Formation of $MoSi_2$ nanopowders by induction plasma synthesis". *15th International Symposium on Plasma Chemistry (ISPC 15).* Proceedings, Vol. VII. Orléans (France). pp. 2749-2756 (2001)

Inaba, H. "Ceria-based solid electrolytes (review)". *Solid State Ionics.* Vol. 83. pp. 1-16. (1996)

Institut fur Wersktoffe und versfahren der energietechnik. http://www.fz-juelich.de/portal/index.php?index=99 (2003)

Jorge, E., Chartier, T. "Ultrasonic dispersion of ceramic powders". *Journal of the American Ceramic Society.* Vol. 73(8). pp. 2552-2554 (1990)

Jurewicz, J., Lemoine, G., Fortier, A. "Alternative routes of thermal plasma synthesis of composite oxide nanopowders". Abstract and full papers. *16th International Symposiun on Plasma Chemistry (ISPC-16).* Italy. (2003)

Karppinen, M., Kyläkoski, P., Niinistö, L., Rodellas, C. "Thermal decomposition as a preparative route to anhydrous rare earth nitrates". *Journal of Thermal Analysis.* Vol. 35. pp. 347-353. (1989)

Kaye, B. H. "Characterization of powders and aerosols". Wiley-VCH. Germany. p. 311 (1999)

Kimpton, J., Randle, T.H., Drennan, J. "Investigation of electrical conductivity as a function of dopant-ion radius in the systems $Zr_{0.75}Ce_{0.08}M_{0.17}O_{1.92}$ (M=Nd, Sm, Gd, Dy, Ho, Y, Er, Yb, Sc)". *Solid State Ionics.* Vol. 149. pp. 89-98. (2002)

Lang, M., Henne, R., Schaper, S., Schiller, G. "Development and characterization of vacuum plasma sprayed thin film solid oxide fuel cells". *Journal of Thermal Spray Technology.* Vol. 10(4). pp. 618-625 (2001)

Lange, Handbook of chemistry (15th Ed). Online.

http://www.knovel.com/knovel2/Toc.jsp?SpaceID=10093&BookID=47#node10821253

Lau, Y. C., Kong, P. C., Pfender, E. "Synthesis of zirconia powders in an RF plasma by injection of inorganic liquid precursors". *Ceramic Transactions 1.* pp 298-303 (1988)

Lefebre, A. H. "Atomization and sprays". Hemishphere publishing corporation. USA. p. 420, (1989)

Lemoine, G., Ménard, H., Jurewiczs, J. W. "Solution plasma spraying of NiO/YSZ cermet anode for SOFC preparation. Influence of plasma processing parameters on the porosity deposits". Abstract and full papers. *16th International Symposiun on Plasma Chemistry (ISPC-16).* Italy. (2003)

Lewis, G. S., Atkinson, A., Steele, B. C. H. "Cobalt additive for lowering the sintering temperature of yttria-stabilized zirconia". *Journal of Materials Science Letters.* Vol. 20. pp. 1155-1157. (2001)

MacDonald, J. R. "Impedance Spectroscopy: Emphasizing solid materials and systems". Wiley. New York. p. 346 (1987)

Mailhot, K., Gitzhofer, F., Boulos, M. I. "Supersonic induction plasma spraying applied to dense yttria stabilized zirconia electrolyte coatings". *13th International Symposium on Plasma Chemistry (ISPC-13).* Beijing, China. Vol. III. pp. 1445-1450. (1997)

McCabe, W., Smith, J., and Harriot, P. "Unit operations of chemical engineering". 5th Ed. McGraw Hill. USA. pp. 1130. (1993)

Merkouf, A., Boulos, M. I. "Distributed energy analysis for an integrated radio frequency induction plasma system". *J. Phys. D: Appl. Phys.* Vol 33. pp 1581-1587. (2000)

Minh, N. Q. "Ceramic fuel cells". *J. of the American Ceramic Society.* Vol. 76(3). pp. 563-588. (1993)

Monterrubio, C., Ageorges, H., Chartier, T., Coudert, J. F., Fauchais, P. "Comparison between two different torches to inject a suspension to produce thin perovskite coatings". Abstract and full papers. *16th International Symposiun on Plasma Chemistry (ISPC-16).* Italy. (2003)

Mosse, A. L., Krasovska, L. I., Dvindenko, I. A., Gorbunov, A. V. "Synthesis of rare-earth element oxides by thermal decomposition of dispersed salts and their aqueous solutions in a plasma jet reactor". *International Journal of Materials and Product Technology.* Vol. 10. No. 3-6. pp. 566-577. (1995)

Muller, M., Bouyer, E., Bradke, M. V., Branston, D. W., Heinmann, R. B., Henne, R., Lins, G., Schiller, G. "Thermal induction plasma processes for the synthesis of SOFC materials". *Materialwissenshchaft und werkstofftechnik.* Vol. 33. No. 6. pp 322-330. (2002)

Nevers, N., "Air pollution control engineering", McGraw-Hill, 506 p. (1995)

Ormerod, R. M. "Solid oxide fuel cells". *Chemical Society Reviews.* Vol. 32. pp. 17-28. (2003)

Proulx, P., Mostaghimi, J., Boulos, M. "Plasma-particle interaction effects in induction plasma modeling under dense loading conditions". *Internal Journal of Heat and Mass Transfer.* Vol. 28. No. 7, pp. 1327-1336, (1985)

Quadakkers, W. J., Piron-Abellan, J., Shemet, V., Singheiser, L. "Metallic interconnectors for solid oxide fuel cells – a review". *Materials at High Temperatures.* Vol. 20(2). pp. 115-127. (2003)

Ralph, J. M., Schoeler, A. C., Krumpelt, M. "Materials for lower temperature SOFC". *Journal of Materials Science.* Vol. 36. pp. 1161-1172. (2001)

Ramachandran, K., Selvarajan, V., "Trajectory and temperature history of the particles of different sizes and their injection velocities in a thermal plasma". *Computational Materials Science.* Vol. 6. pp. 81-91, (1996) Ramasamy, R., Selvarajan, V. "Injected particle behavior in a thermal plasma". *Applied surface science*. Vol. 169-170. pp. 617-621, (2001)

Schiller, G., Müller, M., Bouyer, E., Bradke, M. V. "RF Plasma synthesis and deposition of SOFC materials." Abstract and full papers. *16th International Symposiun on Plasma Chemistry (ISPC-16)*. Italy. (2003)

Schiller,G., Muller, M., Gitzhofer, F. "Preparation of perovskite powders and coatings by radio frequency suspension plasma spraying". *Journal of Thermal Spray Technology*. Vol. 8. No. 3. pp 389-392. (1999)

Silveira, J. L., Gomes, L. A. "Fuel cell cogeneration system: a case of technoeconomic analysis", *Renewable and Sustainable Energy Reviews*. Vol. 3. pp. 233-242, (1999)

Simner S. P., Bonnett, J. R., Canfield, N. L., Meinhardt, K. D., Shelton, J. P., Sprenkle, V. L., Stevenson, J. W. "Development of lanthanum ferrite SOFC cathodes". *Journal of Power Sources*. Vol. 113(1). pp. 1-10. (2003)

Sobolev, V. V., Guilemany, J. M., Martin, A. J. "In-flight behaviour of steel particles during plasma spraying". *Journal of Materials Processing Technology*. Vol. 87. pp. 37-45, (1999)

Song, H. Z., Wang, H. B., Zha, S. W. Peng, D. K., Meng, G. Y. "Aerosol-assisted MOCVD growth of Gd_2O_3-doped CeO_2 thin SOFC electrolyte film on anode substrate". *Solid State Ionics*. Vol. 156. pp. 249-254. (2003)

Sorensen, T. "Nonstoichiometric oxides". Academic Press. USA. p. 441 (1981)

Stambouli, A. B., Traversa, E. "Solid oxide fuel cells (SOFCs): a review of an environmentally clean and efficient source of energy". *Renewable and Sustainable Energy Reviews*. Vol. 6. pp. 433-455. (2002)

Steele, B. C. H. "Appraisal of Ce1-yGdyO2-y/2 electrolytes for the IT-SOFC operation at 500 °C". *Solid State Ionics*. Vol. 129. pp. 95-110. (2000)

Steele, B. C. H. "Materials for IT-SOFC stacks. 35 years R&D: the inevitability of gradualness?". *Solid State Ionics*. Vol. 134. pp. 3-20. (2000)

Steele, B. C. H. "Survey of materials selection for ceramic fuel cells, II. Cathodes and anodes". *Solid State Ionics*. pp. 1223-1234. (1996).

Steele, B. C. H., Heinzel, A. "Materials for fuel-cell technologies". *Nature*. Vol. 414. pp. 345-352. (2001)

Theophile, E., Gitzhofer, F., Boulos, M. I. "Supersonic induction plasma spraying of yttria stabilized zirconia for solid oxide fuel cells". *14th Intenational Symposium on Plasma Chemistry (ISPC-14)*. Vol. IV. Czech Republic. Pp. 2145-2148.

Tian, C., Chan, S. W. "Ionic conductivities, sintering temperatures and microstructures of bulk ceramic CeO_2 doped with Y_2O_3" *Solid State Ionics*. Vol. 134. pp. 89-102. (2000)

Time Magazine. "Blackout. Can it happen again?" Canadian Edition. August 25. pp. 12-27. (2003)

Wendlandt, W. W. "The thermal decomposition of the heavier rare-earth metal chloride hydrates". *Journal of Inorganic and Nuclear Chemistry*. Vol. 9. pp. 136-139. (1959)

Wendlandt, W. W. "The thermal decomposition of yttrium, scandium and some rare-earth chloride hydrates". *Journal of Inorganic and Nuclear Chemistry*. Vol. 5. pp. 118-122. (1957)

Wendlandt, W. W. "The thermolysis of the rare earth and other metal nitrates". *Analytica Chimica Acta*. Vol. 15. pp. 435-439. (1956)

Wendlandt, W. W. "Thermal decomposition of the heavier rare-earth metal nitrate hydrates. Thermobalance and differential thermal analysis studies". *Journal of Inorganic and Nuclear Chemistry*. Vol. 12, pp 276-280. (1960)

Xiong, Y., Yamaji, K., Sakai, N., Negishi, H., Horita, T., Yokokawa, H. "Electronic conductivity of ZrO_2-CeO_2-$YO_{1.5}$ solid solutions". *Journal of the Electrochemical Society*. Vol. 148 (12). pp. 489-492. (2001)

Zha, S., Xia, C., Meng, G. "Effect of Gd (Sm) doping on properties of ceria electrolyte for solid oxide fuel cells". *Journal of Power Sources*. Vol. 115. pp. 44-48. (2003)

Appendix A. Physical properties of selected oxides, ionic conductivity theory of oxides and sample calculations.

a. Physical properties of selected solid oxides

	MW	ρ $[g/cm^3]$	$T_{melting}$ [°C]	$T_{boiling}$ [°C]
CeO_2	172.13	7.65	2,400	
Gd_2O_3	362.50	7.07	2,339	3,900
Y_2O_3	225.81	5.03	2,438	*4,300
Sm_2O_3	348.70	7.60	2,269	3,780

Ref: 83rd CRC Handbook of Chemistry and Physics
*Ref: Lange, Handbook of chemistry (15th Ed)

Schema illustrating oxygen environment around a) Ce-cubic structure, b) Zr-tretagonal structure (Ref. R&D Review of Toyota CRDL. Vol. 37. No. 4).

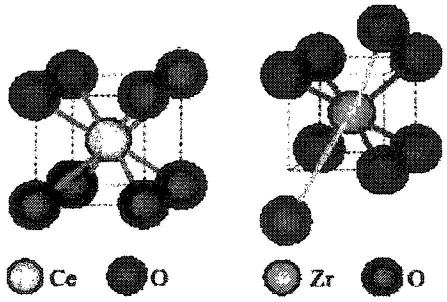

a b

Definition of different embedded cluster surface models of doped CeO_2 in the full surface environment; atoms contained in the model cluster are highlighted. Cluster models 5A (right), 5B (center), and 5C (left) have five-coordinated central cerium ions, while clusters 6B (right), 6A (center), and 6C (left) represent fully coordinated surface cerium ions (Ca-ion acting as dopant) (ref. de Carolis et al.)

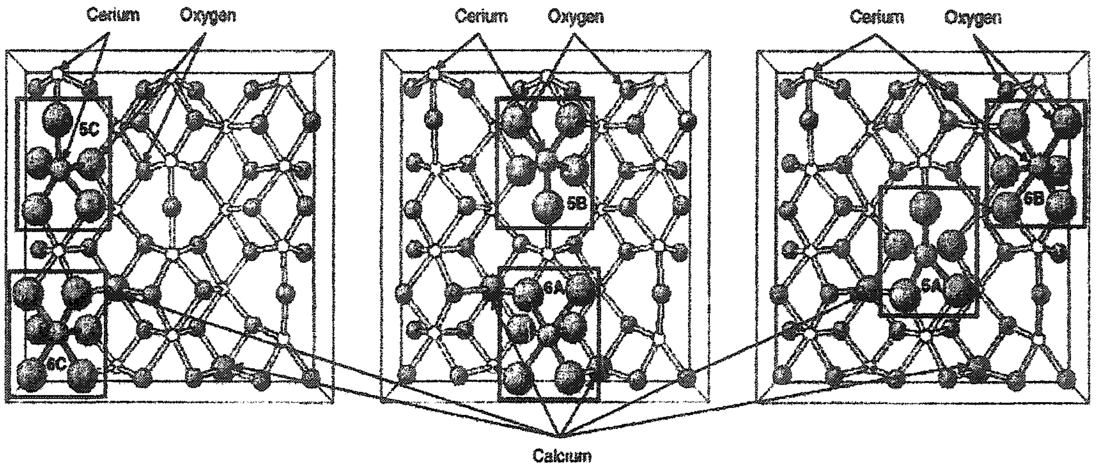

b. Theory of ionic conductivity in fluorite oxides

Nonstoichiometric oxides can be classified in three types depending on their composition range, i.e. (i) essentially stoichiometric with a very narrow composition range, (ii) nonstoichiometric with limited composition ranges and (iii) grossly nonstoichiometric with broad composition ranges. Fluorite structure falls into grossly nonstoichiometric, e.g. CeO_2, PrO_2, TbO_2, etc. Interest in anion-deficient fluorites has been due to their unusual transport and thermodynamic properties. These defective compounds show very high anion mobilities; sufficient in some cases for the materials to be classified as superionic conductors (*Sorensen*, 1981). Vacancies randomly distributed throughout the oxide sublattice are an essential element required for oxygen-ion conduction in electrolyte materials, because these vacancies increase the likelihood of an oxygen ion to "jump" within the lattice (i.e. increase oxygen mobility) (*Kimpton*, 2002)

The electrical conductivity, and more specifically the ionic conductivity, is the more commonly accepted parameter to determine the most satisfactory electrolyte. Hence, it is important to explain the theory behind the calculation of this parameter in order to find the correct chemical composition to optimize the cell functionality. The theory of electrical conduction has been described by Kilner and Steel (*Sorensen*, 1981) and it is summarized here.

The electrical conductivity of any solid can be expressed as (*Eq. 1*)

$$\sigma_{total} = \sum_{j} \sigma_j \qquad (1)$$

where σ_j are the partial conductivities of each of the charge carriers (in siemens per meter) j present in the solid. These charge carriers can be either electronic in nature (i.e. either electrons or electron holes) or atomic in nature and usually are defects of either the anionic or cationic sublattice (i.e. ionic). We can expand each of the partial conductivities as

$$\sigma_j = C_j Z_j e \mu_j \qquad (2)$$

where C_j is the number of carriers of type j per meter^3, Z_j the number of electronic charges e of these carriers (Coulombs), and μ_j their mobility in the solid (meter^2 per second per volt). Substitution of *Eq. 2* into *Eq. 1* gives

$$\sigma_{total} = \sum_{j} C_j Z_j e \mu_j \qquad (3)$$

We can see from *Eq.2* that each partial conductivity is a product of the number of carriers multiplied by a mobility; consequently, if two carriers are present in equal concentrations, it will be their mobilities that determine which mode of conductivity will predominate. For oxides, the mobilities of electronic defects are approximately 10^2-10^3 times greater than the mobilities of ionic defects, and therefore a relatively small concentration of electrons can have a large effect on the total conductivity. Nonetheless, the ionic conductivity is augmented by increasing the ionic defects (vacancies) in the solid lattice with the introduction of a dopant agent, which facilitates oxygen ion migration. With this addition, the ionic conductivity of the fluorite oxides dominates over the other conductivities and thus the total electrical conductivity of the material is mainly due to the ionic component. This is an important concept because electrical conductivity is assumed to be equivalent to ionic conductivity in most of the articles reviewed.

Empirically it has been found that the temperature dependence of the conductivity can be expressed by an equation of the form

$$\sigma * T = A * \exp\left(\frac{-E_a}{kT}\right) \tag{4}$$

where A is a constant or pre-exponential term, E_a the activation energy, and k the Boltzmann constant.

In the case of oxygen-ion conductors (i.e. SOFCs), the conduction occurs via anion vacancies, and therefore the mobility can be expanded according to the Nerst-Einstein relation as follows

$$\mu = \gamma(Ze/kT)a_o^2 v_o \exp\left(\frac{-\Delta G_m}{kT}\right) \tag{5}$$

where γ is a geometric factor, v_o is the jump attempt frequency, ΔG_m the Gibbs free energy for the jump, a_o is the jump distance and $Z=2$ for oxygen. Recalling that $\Delta G_m=\Delta H_m-T\Delta S_m$ and defining the number of charge carriers as follows (*Eq. 6*), the ionic conductivity can be then expressed (*Eq. 7*)

$$C = [V_o^{\cdot\cdot}]\{1-[V_o^{\cdot\cdot}]\}N_o \tag{6}$$

where C is the number of charge carriers, $[V_o^{\cdot\cdot}]$ is the concentration of oxygen deficiencies and N_o is the number of oxygen sites per unit volume.

$$\sigma * T = A'[V_o^{\cdot\cdot}]\exp\left(\frac{-\Delta H_m}{kT}\right); A' = (4e^2/k)a_o^2 v_o N_o \exp(\Delta S_m/k) \tag{7}$$

To conclude this review and therefore obtain a final expression for ionic conductivity, some assumptions should be introduced. First, it is generally accepted that the vacancies induced by doping of aliovalent cations (i.e. cations with a valence number lower than that of the host cation) are not free but are bound to dopant cations to form defect associates (W). Second, this binding energy (E_a) is mainly due to the coulombic attraction of the defects caused by their effective charges in the lattice; however, it also contains terms due to relaxation of the lattice around the defect, which depend upon the effective charge, the size of the dopant, and the cation polarizability. Incorporating these assumptions into *Eq. 6* and for the case in which a metal M^{3+} is added to an oxide such as CeO_2, the ionic conductivity is expressed as follows (*Eq. 9*)

$$[V_o^{\cdot\cdot}] = (1/W)\exp\left(\frac{-\Delta H_A}{kT}\right); \tag{8}$$

where W is the number of orientations of the associate and ΔH_A is the enthalpy of association

$$\sigma T = (A'/W)\exp\left(\frac{-\Delta H_m + \Delta H_A}{kT}\right); \tag{9}$$

$$A = A'/W; E_a = \Delta H_m + \Delta H_A$$

c. Calculation of the density of solid oxide mixtures

The density was calculated as a weighted average of the densities of two oxides according to the number of moles, *x*, employed for each dopant, i.e. $(CeO_2)_{1-x}(Me_2O_3)_{x/2}$ Me=Gd, Sm and Y. For example for x=0.1, the solid oxide $Ce_{0.9}Me_{0.1}O_{1.95}$ results. This solid oxide is composed of 90% mole CeO_2 and 5% mole Me_2O_3 (i.e. 10% $MeO_{1.5}$). Those mole percentages must be transformed into weight percentages using the molecular weight of their respective oxides. Finally, the new basis is then used to calculate the density of the solid (Eq. 3).

$$\rho_{solid\cdot mixture} = \rho_{CeO2} * \%wt_{(of\cdot the\cdot new\cdot basis)} + \rho_{Me2O3} * \%wt_{(of\cdot the\cdot new\cdot basis)} \qquad (10)$$

d. Calculation of the atomized droplet size

The diameter of the atomized droplet can be calculated using the following set of equations. This value is a function of the diameter of the oxide particle and its calculated density, the density of the precursor solution, the metal content in the nitrate salts and the solubility of those salts in distilled water.

$$A = \frac{D_{Ox}^3 \cdot \pi}{6} x \frac{\rho_{Ox}}{\%wt \cdot Ce \cdot in \cdot Ce(NO_3)_3 \cdot 6H_2O}; \qquad (11)$$

$$B = \frac{D_{Ox}^3 x \pi}{6} x \frac{\rho_{Ox}}{\%wt \cdot Ce \cdot in \cdot Me(NO_3)_3 \cdot 6H_2O} \qquad (12)$$

$$C = \frac{A}{Sol_A} + \frac{B}{Sol_B}; \qquad TM = A + B + C; \quad D_{Droplet} = \left(\frac{6}{\pi} x \frac{TM}{\rho_{Sol}}\right)^{1/3} \qquad (13)$$

where

D_{Ox} = Desired diameter of dense and spherical oxide particle [μm]

$D_{Droplet}$ = Calculated diameter of the spherical atomized droplet [μm]

ρ_{Ox} = Calculated density of the synthesized oxide [g/cm^3]

ρ_{Sol} = Measured density of the corresponding precursor solution for the synthesized oxide [g/cm^3]

%wt Me in $Me(NO_3)_3.6H_2O$ = Percentage weight of the Me=Ce,Gd, Sm or Y in $Me(NO_3)_3.6H_2O$.

Sol_A = Solubility of $Ce(NO_3)_3.6H_2O$ in distilled H_2O [g $Ce(NO_3)_3.6H_2O$ / g H_2O]

Sol_B = Solubility of $Me(NO_3)_3.6H_2O$ in distilled H_2O [g $Me(NO_3)_3.6H_2O$ / g H_2O], Me=Gd, Sm or Y

e. Sensitivy analysis

The basis of calculation for the sensitivity analysis was the correlations proposed by Lefebre (*Lefebre, 1989*) in which the Sauter mean diameter (SMD) for atomized droplets was empirically determined and fitted using the following equation.

$$SMD = 0.95\frac{(\sigma\dot{m}_L)^{0.33}}{U_R\rho_L^{0.37}\rho_A^{0.3}}\left(1+\frac{1}{ALR}\right)+0.13\left(\frac{\mu_L^2 d_o}{\sigma\rho_L}\right)^{0.5}\left(1+\frac{1}{ALR}\right)^{1.7} \quad (14)$$

σ = liquid surface tension [kg/s^2]
m_L = liquid mass flow rate [kg/s]
U_R = velocity of the atomizing gas relative to the liquid velocity [m/s]
ρ_L = liquid density [kg/m^3]
ρ_A = gas density [kg/m^3]
ALR = atomizing mass liquid/gas flow rate ratio [dimensionless]
μ_L = liquid viscosity [kg/m.s]
d_o = internal diameter of the nozzle of the atomizing probe [m]
SMD = Sauter mean droplet diameter [m]

f. Scherrer's formula

$$T = \frac{0.9\lambda}{B\cos\theta_B} \quad (15)$$

T = crystalline size [Å]
B = full width half maximum [rad]
θ_B = Bragg angle [deg]
λ = wavelength of the incident monochromatic beam [Å]

g. Bartlett's test

1. For each of the k samples denote the standard deviations by s_i and the corresponding samples sizes by n_i (number of particles measured)
2. Calculate the pooled sample variance

$$Sp_p^2 = \frac{\sum(n_i - 1)s_i^2}{\sum(n_i - 1)} \quad (16)$$

3. Compute the test statistic

$$B = \ln(Sp_p^2)\sum(n_i - 1) - \sum(n_i - 1)\ln(s_i^2) \quad (17)$$

4. Reject the hypothesis of equal standard deviations if B exceeds an upper-tail chi-square critical value with significance level α and degrees of freedom $\nu = k-1$.

h. Comparison of two means of independent samples

1. Hypothesis: H_o: $\mu_d = \mu_o$ vs H_a: $\mu_d \neq \mu_o$
2. Reject H_o if the absolute value of $t_c > t_{\alpha/2}$
3. Calculate t (Student's t-distribution)

$$t = \frac{(\bar{y}_1 - \bar{y}_2) - (\mu_1 - \mu_2)}{\left(s_1^2 / n_1 + s_2^2 / n_2\right)^{1/2}} \tag{18}$$

4. Calculate the number of degrees of freedom ν from the following formula

$$\upsilon = \frac{(w_1 + w_2)^2}{w_1^2 /(n_1 - 1) + w_2^2 /(n_2 - 1)} \text{ where } w_1 = s_1^2 / n_1 ; w_2 = s_2^2 / n_2 \tag{19}$$

Appendix B. Calibration curves

a. Peristaltic pump calibration curve

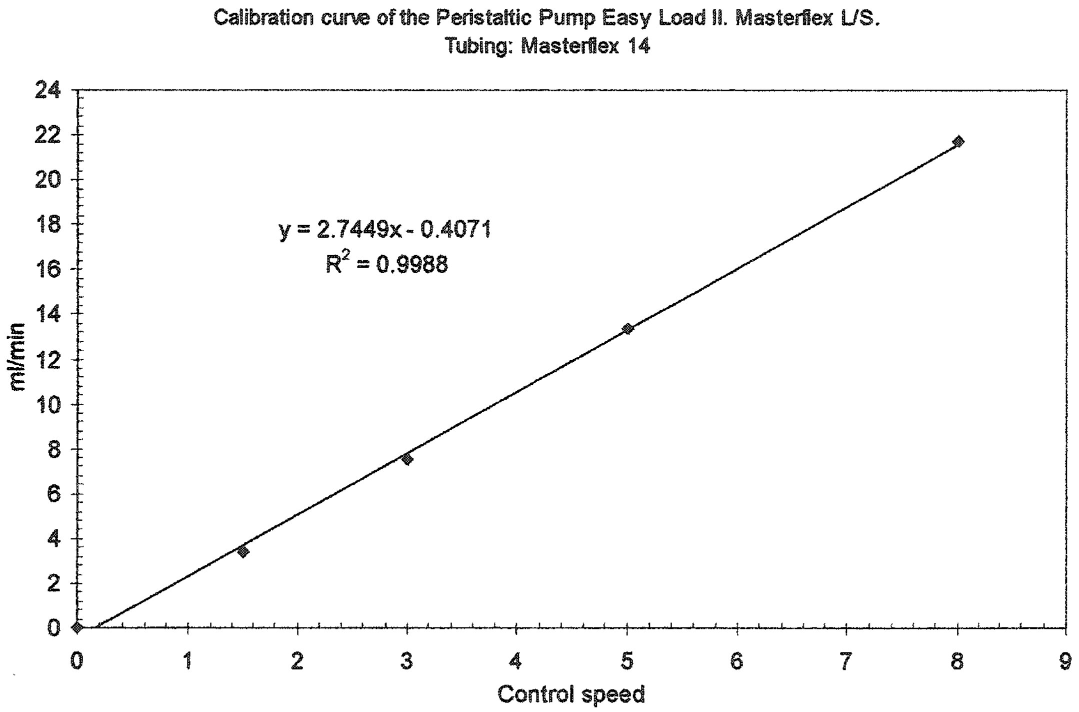

b. Rotameter calibration curve

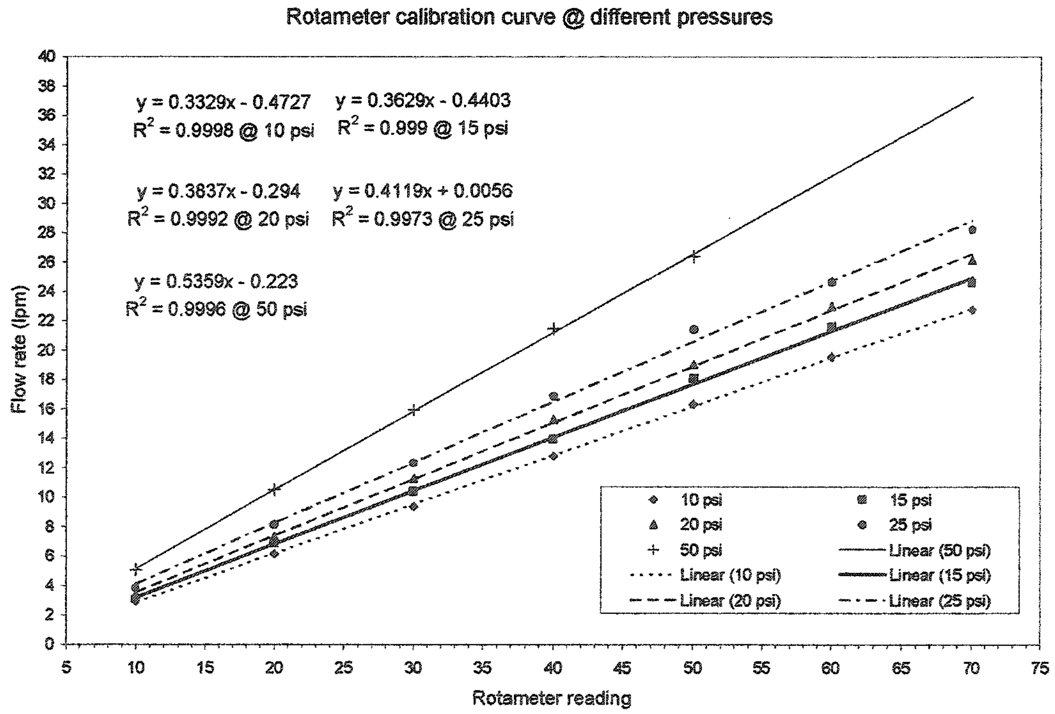

Appendix C. Image analysis

a. Commercial software methodology

1. Scion Image software must be installed
2. Open the image that is to be analyzed
3. Under the *options* menu → *profile plot options* → check *fixed y-axis scale* from 0 to 255
4. Under the *process* menu → click *smooth* once
5. Under the *special* menu → *load macros* → browse for the Scion Macros folder and select the *plotting* macro
6. Under the *special* menu → *export profile plots* → provide the y-increment in pixels (usually 20 is a good starting value)
7. Save all the files in a particular folder and leave the default file name *(PLOT0000)* → click *save*
8. Exit Scion image software (not need to save the image changes)

b. Developed algorithm methodology

1. Open MATLAB and under the *file* menu → *set path* → specify the folder in which the exported Scion files were saved
2. Run the *PSA2.m* function. Pay special attention to the *IniFile,*(usually 0) *TotFiles,*(total number of files exported, usually 44) *Conversion* (the equivalence of one pixel in nanometers) and *ThresPart* (the greyscale value that defines the background) variable definitions.
3. The program will ask you for the grey scale tolerance, enter a value of 10 as a fist guess.
4. The *lineplot.m* and the *plothist.m* will be needed to run the *PSA2.m* function. These two functions are provided below
5. Make sure that the results given by the software are visually compared to the image under analysis, be aware of the 2 artifacts of this technique and if needed recalculate the distribution using a different grey scale tolerance.
6. The *SamOrg.m* function must be now run. This stores the information of the analyzed image in a structure array. The ID value corresponds to the number of the sample analyzed.
7. All the variable from the workspace must be deleted with the exception of the struct array variable whose name could be modified in the *SamOrg.m* file
8. Steps 1 to 8 from the commercial software are repeated and steps 2 to 6 from the in-house software are also repeated.
9. A new ID value must be given when running *SamOrg.m* so that the struct array stores the information of the second image and thus increase in size.
10. After running SamOrg.m for the 5th image DO NOT delete the variables in the workspace. Run the *buildup.m* function and now save the workspace variables. This concludes the data analysis for one sample.
11. The particle size distribution can now be truncated using the *truncation.m* function. The upper and lower bound must be input.
12. The *OvOrg.m* function is now run to store the truncated PSD values.
13. The *OvOrg.m* function must be run 5 times to store 5 different samples before proceeding to the next step

14. The *OvGraphs1set.m* function is run to plot the final results. This function requires the standard deviation and the median values of the different distributions. These values are calculated based on the method described by Nevers (*Nevers, 1995*)

PSA2.m

```
%***Program created by Ian Castillo July 9, 2003*****
%**************************************************
%**************************************************************
%This program reads the plot values generated by Scion
%and organizes them into a basic array for further manipulation
%**************************************************************
%Memory clear
%clear all;
clc;
clear TolGrey;
clear ThresPart;
clear DataMatrix;
%Variable declaration
IniFile=0;
TotFiles=44;
PixStep=1;
%Initialization & Basic matrix generation
A=load(['plot000',int2str(IniFile)]);
BasicArraySize=size(A);
BasicMatrix=zeros((BasicArraySize(1,1)),(TotFiles+2));
%Initial data reading
BasicMatrix(:,IniFile+2)=A(:,1);
PixelVec=[IniFile+1:PixStep:BasicArraySize(1,1)]';
BasicMatrix(:,1)=PixelVec(:,1);
%Main Reading loop
for n=1:TotFiles
  if n<=9
    A=load(['plot000',int2str(n)]);
    BasicMatrix(:,n+2)=A(:,1);
  end
  if n>=10
    A=load(['plot00',int2str(n)]);
    BasicMatrix(:,n+2)=A(:,1);
  end
end
%Clearing unnecessary variables
clear A;
clear PixelVec;
%***Program created by Ian Castillo July 11, 2003*****
%**************************************************
%**************************************************************
%This program reads the plot values generated in the BasicMatrix
%and converts the BasicMatrix into a binary matrix
%**************************************************************
%Variable declaration
NumPart=0;
PixCor=2;
Conversion=1; % 1 pixel is equivalent to X nm
TolGrey=input('Tolerance Grey Value = '); %Tolerance of grey scale to define a particle
ThresPart=110; %Minimum grey value for a pixel to be considered a particle
PartSizeInterval=Conversion;
MinPartSize=5; %Minimum particle size in nanometers
MaxPartSize=1000; %Maximum particle size in nanometers
```

```
%Binary Basic Array
BinaryMatrix=zeros(BasicArraySize(1,1),TotFiles);
for j=2:TotFiles+2
   for i=2:(BasicArraySize(1,1)-1)
   %Condition for binary matrix
      if BasicMatrix(i,j)>=ThresPart & abs(BasicMatrix(i,j)-BasicMatrix(i-1,j))<=TolGrey &
abs(BasicMatrix(i,j)-BasicMatrix(i+1,j))<=TolGrey
         BinaryMatrix(i,j)=1;
      else
         BinaryMatrix(i,j)=0;
      end
   end
end
%Completing the Binary Array
for j=2:TotFiles+2
   if BinaryMatrix(2,j)==1
       BinaryMatrix(1,j)=1;
    else
       BinaryMatrix(1,j)=0;
    end
 end
%Particle size counting
for j=2:TotFiles+2
   Length=0;  %Initializing particle size counter
      for i=2:BasicArraySize(1,1)
         if BinaryMatrix(i,j)==1
            Length=Length+1;
            if Length==1
               NumPart=NumPart+1;
            end
         else
            if NumPart~=0 & Length~=0
                  DataMatrix(NumPart)=Length;
                  Length=0;
            end
         end
      end
end
%Pixel correction
DataMatrix=DataMatrix';
DataMatrix=DataMatrix+PixCor;
DataMatrix=DataMatrix*Conversion;
plothist(MinPartSize,PartSizeInterval,MaxPartSize,NumPart,DataMatrix)
lineplot(TotFiles,BasicMatrix,BinaryMatrix)
clear i;
clear j;
clear n;
clear PixStep;
clear PixCor;
clear Length;
clear BasicArraySize;
clear BasicMatrix;
clear BinaryMatrix;
clear Conversion;
clear IniFile;
clear TotFiles;
%clear DataMatrix;
%clear NumPart;
```

plothist.m

```
%**********************************************************************
%This program plots the total number of particles counted
%and the histogram and cumulative frequency of the volume and
%number particle size
%**********************************************************************
function
[CumFreqVol,FractCumFreq,Xcategory,FractCounts,FractHistVol]=plothist(MinPartSize,PartSizeInterval,Max
PartSize,NumPart,DataMatrix);
%Generating values for the graph plotting
Xcategory=[MinPartSize:PartSizeInterval:MaxPartSize];
%Number particle size distribution
Counts=hist(DataMatrix,Xcategory); %Counts is related to the length of the particles
CumFreq=cumsum(Counts);
FractCumFreq=CumFreq/NumPart;
FractCounts=Counts/NumPart;
%Volume particle size distribution
HistVol=Xcategory.*Xcategory.*Xcategory;
HistVol=HistVol.*Counts;
HistVol=HistVol*pi/6;
TotalPartVol=sum(HistVol);
FractHistVol=HistVol/TotalPartVol;
CumFreqVol=cumsum(FractHistVol);
%Plotting
subplot(5,1,1)
X=[1:1:NumPart]';
plot(X,DataMatrix(:,1),'k'),grid
xlabel('Number of particles')
ylabel('Particle length (nm)')
title('Particle length Vs Number of particles');
subplot(5,1,2)
bar(Xcategory,FractCounts,'k'),grid
xlabel('Particle Size (nm)')
ylabel('% of particles')
title('Particle Size Distribution')
set(gca,'XScale','log')
axis([1 1000 0 0.5]);
subplot(5,1,3)
plot(Xcategory,FractCumFreq,'k'),grid
xlabel('Particle Size (nm)')
ylabel('% of Particles')
set(gca,'XScale','log')
axis([1 1000 0 1]);
subplot(5,1,4)
bar(Xcategory,FractHistVol,'k'), grid
xlabel('Particle Size (nm)')
ylabel('% of Particles')
set(gca,'XScale','log')
axis([1 1000 0 0.5]);
subplot(5,1,5)
plot(Xcategory,CumFreqVol,'k'),grid
xlabel('Particle Size (nm)')
ylabel('% of Particles')
set(gca,'XScale','log')
axis([1 1000 0 1]);
```

lineplot.m

```
%**********************************************************************
```

```
%This program plots three different lines to compare the performance of
%the grey scale-binary algorithm
%**********************************************************************
function lineplot(TotFiles,BasicMatrix,BinaryMatrix);
%obtaining information from the user
%Yinc=input('Yinc = ');
Yinc=20;
%defining the number of lines that will be plotted
%FirstLineFile=round(TotFiles/4);
FirstLineFile=5;
%SecondLineFile=FirstLineFile+FirstLineFile;
SecondLineFile=15;
%ThirdLineFile=SecondLineFile+FirstLineFile;
ThirdLineFile=31;
%transfering information
BasicMatrixLine1=BasicMatrix(:,FirstLineFile+2);
BasicMatrixLine2=BasicMatrix(:,SecondLineFile+2);
BasicMatrixLine3=BasicMatrix(:,ThirdLineFile+2);
BinaryMatrixLine1=BinaryMatrix(:,FirstLineFile+2);
BinaryMatrixLine2=BinaryMatrix(:,SecondLineFile+2);
BinaryMatrixLine3=BinaryMatrix(:,ThirdLineFile+2);
%getting the y location of the chosen lines
YPixLine1=Yinc*FirstLineFile;
YPixLine2=Yinc*SecondLineFile;
YPixLine3=Yinc*ThirdLineFile;
%plotting
figure(2);
subplot(3,1,1)
plot(BasicMatrix(:,1),BasicMatrixLine1,'k'),grid
title(['Y location @ ',num2str(YPixLine1),' pixels for No. ',...
      num2str(FirstLineFile),' line']);
%xlabel('X-direction (pixels)')
ylabel('Grey Scale')
set(gca,'YTick',[0:50:250],'FontSize',9)
set(gca,'XTick',[0:50:1280],'FontSize',9)
axis([0 1280 0 255]);
%plotting the binary data on the first graph
h1=gca;
h2=axes('Position',get(h1,'Position'));
plot(BasicMatrix(:,1),BinaryMatrixLine1,'rx',...
   BasicMatrix(:,1),BinaryMatrixLine1,'r:')
set(h2,'YAxisLocation','right','Color','none','XTickLabel',[]);
set(h2,'XLim',get(h1,'XLim'),'Layer','top');
set(gca,'YTick',[0:0.2:1],'FontSize',9)
%*********************************************
subplot(3,1,2)
plot(BasicMatrix(:,1),BasicMatrixLine2,'k'),grid
title(['Y location @ ',num2str(YPixLine2),' pixels for No. ',...
      num2str(SecondLineFile),' line']);
%xlabel('X-direction (pixels)')
ylabel('Grey Scale')
set(gca,'YTick',[0:50:250],'FontSize',9)
set(gca,'XTick',[0:50:1280],'FontSize',9)
axis([0 1280 0 255]);
%plotting the binary data on the second graph
h1=gca;
h2=axes('Position',get(h1,'Position'));
plot(BasicMatrix(:,1),BinaryMatrixLine2,'rx',...
   BasicMatrix(:,1),BinaryMatrixLine2,'r:')
```

```
set(h2,'YAxisLocation','right','Color','none','XTickLabel',[]);
set(h2,'XLim',get(h1,'XLim'),'Layer','top');
set(gca,'YTick',[0:0.2:1],'FontSize',9)
%***********************************************
subplot(3,1,3)
plot(BasicMatrix(:,1),BasicMatrixLine3,'k'),grid
title(['Y location @ ',num2str(YPixLine3),' pixels for No. ',...
      num2str(ThirdLineFile),' line']);
xlabel('X-direction (pixels)')
ylabel('Grey Scale')
set(gca,'YTick',[0:50:250],'FontSize',9)
set(gca,'XTick',[0:50:1280],'FontSize',9)
axis([0 1280 0 255]);
%plotting the binary data on the third graph
h1=gca;
h2=axes('Position',get(h1,'Position'));
plot(BasicMatrix(:,1),BinaryMatrixLine3,'rx',...
   BasicMatrix(:,1),BinaryMatrixLine3,'r:')
set(h2,'YAxisLocation','right','Color','none','XTickLabel',[]);
set(h2,'XLim',get(h1,'XLim'),'Layer','top');
set(gca,'YTick',[0:0.2:1],'FontSize',9)
```

SamOrg.m

```
%***Program created by Ian Castillo July 28, 2003*****
%**************************************************
%*************************************************************
%This program creates a structure array of the sample under study
%*************************************************************
ID=input('ID = ');
%the name of the different dopants must be changed once the pictures are
%analyzed
Gd01_R(ID).name='Gd01_R';
Gd01_R(ID).number=ID;
Gd01_R(ID).numpart=NumPart;
Gd01_R(ID).data=DataMatrix;
Gd01_R(ID).threshold=ThresPart;
Gd01_R(ID).tolerance=TolGrey;
```

buildup.m

```
%***Program created by Ian Castillo July 28, 2003*****
%**************************************************
%*************************************************************
%This program builds-up the matrix containing the information of a
%particular sample
%*************************************************************
%*******change values*******
function [SumDataMatrix,SumTotPart]=buildup(Gd01_R,MinPartSize,...
   PartSizeInterval,MaxPartSize);
clear DataMatrix;
%*******change values*******
   AA=getfield(Gd01_R(1),'data');
   AB=getfield(Gd01_R(2),'data');
   AC=getfield(Gd01_R(3),'data');
   AD=getfield(Gd01_R(4),'data');
   AE=getfield(Gd01_R(5),'data');
SumDataMatrix=vertcat(AA,AB,AC,AD,AE);
%SumDataMatrix=vertcat(AA,AB,AC);
A=size(SumDataMatrix);
```

```
SumTotPart=A(1,1);
%********change values*********
save('yellowdata','SumTotPart','SumDataMatrix','-ASCII')
plothist(MinPartSize,PartSizeInterval,MaxPartSize,...
   SumTotPart,SumDataMatrix)
```

truncation.m

```
%***Program created by Ian Castillo August 13, 2003*****
%**************************************************
%**************************************************************
%This program creastes a truncated array of the particle size information
%and generates a histogram of the number and volume particle size
%**************************************************************
function
[NumTruncPart,FractCumFreq,CumFreqVol,Xcategory,FractCounts,FractHistVol]=truncation(SumDataMatri
x,SumTotPart,MinPartSize,...
   PartSizeInterval,MaxPartSize);
UpLimPartSize=input('Upper particle size limit= ');
LowLimPartSize=input('Lower particle size limit= ');
k=1;
NewDataMatrix=SumDataMatrix;
for i=1:SumTotPart
   if NewDataMatrix(i,1)>=LowLimPartSize & NewDataMatrix(i,1)<=UpLimPartSize
      TruncDataMatrix(k)=NewDataMatrix(i,1);
      k=k+1;
   end
end
TruncDataMatrix=TruncDataMatrix';
NumPartTruncDataMatrix=size(TruncDataMatrix);
NumTruncPart=NumPartTruncDataMatrix(1,1);
[CumFreqVol,FractCumFreq,Xcategory,FractCounts,FractHistVol]=plothist(MinPartSize,PartSizeInterval,Max
PartSize,..
   NumTruncPart,TruncDataMatrix);
```

OvOrg.m

```
%***Program created by Ian Castillo August 13, 2003*****
%**************************************************
%**************************************************************
%This program creates a structure array of the sample under study
%**************************************************************
ID=input('ID = ');
%the name of the different dopants must be changed once the pictures are
%analyzed
%OvResults3 is for the second set of samples
OvResults2(ID).name='Gd01-R';
OvResults2(ID).number=ID;
OvResults2(ID).numpart=NumTruncPart;
OvResults2(ID).datanumber=FractCumFreq;
OvResults2(ID).datavolume=CumFreqVol;
OvResults2(ID).xcategory=Xcategory;
OvResults2(ID).fractcounts=FractCounts;
OvResults2(ID).fracthistvol=FractHistVol;
```

OvGraphs1set.m

```
%***Program created by Ian Castillo August 13, 2003*****
%**************************************************
%**************************************************************
%This program generates a graph showing the different samples
```

```
%************************************************************
function [B]=OvGraphs1set(OvResults2)
  A1=getfield(OvResults2(1),'datanumber');
  B1=getfield(OvResults2(1),'datavolume');
  C1=getfield(OvResults2(1),'xcategory');
  D1=getfield(OvResults2(1),'fractcounts');
  E1=getfield(OvResults2(1),'fracthistvol');
  F(1)=getfield(OvResults2(1),'numpart');
  A2=getfield(OvResults2(2),'datanumber');
  B2=getfield(OvResults2(2),'datavolume');
  C2=getfield(OvResults2(2),'xcategory');
  D2=getfield(OvResults2(2),'fractcounts');
  E2=getfield(OvResults2(2),'fracthistvol');
  F(2)=getfield(OvResults2(2),'numpart');
  A3=getfield(OvResults2(3),'datanumber');
  B3=getfield(OvResults2(3),'datavolume');
  C3=getfield(OvResults2(3),'xcategory');
  D3=getfield(OvResults2(3),'fractcounts');
  E3=getfield(OvResults2(3),'fracthistvol');
  F(3)=getfield(OvResults2(3),'numpart');
  A4=getfield(OvResults2(4),'datanumber');
  B4=getfield(OvResults2(4),'datavolume');
  C4=getfield(OvResults2(4),'xcategory');
  D4=getfield(OvResults2(4),'fractcounts');
  E4=getfield(OvResults2(4),'fracthistvol');
  F(4)=getfield(OvResults2(4),'numpart');
  A5=getfield(OvResults2(5),'datanumber');
  B5=getfield(OvResults2(5),'datavolume');
  C5=getfield(OvResults2(5),'xcategory');
  D5=getfield(OvResults2(5),'fractcounts');
  E5=getfield(OvResults2(5),'fracthistvol');
  F(5)=getfield(OvResults2(5),'numpart');
  %************************************************************
  %Figure 1
  %************************************************************
  figure(1);
  subplot(2,1,1)
  plot(C1,A1,'k',C2,A2,'b',C3,A3,'r',C4,A4,'g',C5,A5,'c'),grid
  xlabel('Particle size diameter (nm)')
  ylabel('Fraction of Particles')
  legend('Sm015-R','Sm01-R','Gd01-R','Sm02-F','Sm02-R')
  set(gca,'XScale','log')
  axis([1 1000 0 1]);
  subplot(2,1,2)
  plot(C1,B1,'k',C2,B2,'b',C3,B3,'r',C4,B4,'g',C5,B5,'c'),grid
  xlabel('Particle size diameter (nm)')
  ylabel('Fraction of Particles')
  legend('Sm015-R','Sm01-R','Gd01-R','Sm02-F','Sm02-R')
  set(gca,'XScale','log')
  axis([1 1000 0 1]);
  %************************************************************
  %Figure 2
  %************************************************************
  figure(2);
  %Number distribution graphs
  muC1n=17.566;
  sigmaC(1)=0.7191;
  muC2n=23.271;
  sigmaC(2)=0.5328;
```

```
muC3n=14.071;
sigmaC(3)=0.5991;
muC4n=15.015;
sigmaC(4)=0.5779;
muC5n=9.478;
sigmaC(5)=0.5667;
%Plot y-scale-maximum
ymaxn=10;
AdjFact1=0.14;
AdjFact3=0.06;
AdjFact5=0.08;
AdjFact7=0.08;
AdjFact9=0.12;
%subplot(5,2,1) %inactive in order to oganize the M. Eng thesis presentation
%New location
subplot(5,2,3)
%************
bar(C1,D1*100,'k'),grid
%xlabel('Particle size diameter (nm)')
ylabel('% of particles(N)')
set(gca,'XScale','log')
axis([1 1000 0 ymaxn]);
h1 = gca;
%Create the second axes at the same location before plotting the second dataset.
h2 = axes('Position',get(h1,'Position'));
y=lognpdf(C1,log10(muC1n),sigmaC(1));
y=y*AdjFact1;
plot(C1,y*100,'r','LineWidth',2)
set(gca,'XScale','log')
%To ensure that the second axes does not interfere with the first, locate the y-axis on the right side of the axes, make the background transparent, and set the second axes' x-tick marks to the empty matrix.
set(h2,'YAxisLocation','right','Color','none','XTickLabel',[])
axis([1 1000 0 ymaxn]);
%Align the x-axis of both axes and display the grid lines on top of the bars.
%subplot(5,2,3) %inactive in order to oganize the M. Eng thesis presentation
%New location
subplot(5,2,1)
%************
bar(C2,D2*100,'k'),grid
%xlabel('Particle size diameter (nm)')
ylabel('% of particles(N)')
set(gca,'XScale','log')
axis([1 1000 0 ymaxn]);
h1 = gca;
%Create the second axes at the same location before plotting the second dataset.
h2 = axes('Position',get(h1,'Position'));
y=lognpdf(C2,log10(muC2n),sigmaC(2));
y=y*AdjFact3;
plot(C2,y*100,'r','LineWidth',2)
set(gca,'XScale','log')
%To ensure that the second axes does not interfere with the first, locate the y-axis on the right side of the axes, make the background transparent, and set the second axes' x-tick marks to the empty matrix.
set(h2,'YAxisLocation','right','Color','none','XTickLabel',[])
axis([1 1000 0 ymaxn]);
%Align the x-axis of both axes and display the grid lines on top of the bars.
% subplot(5,2,5) same as before
%New location
subplot(5,2,9)
%************
```

```
bar(C3,D3*100,'k'),grid
xlabel('Particle size diameter (nm)')
ylabel('% of particles(N)')
set(gca,'XScale','log')
axis([1 1000 0 ymaxn]);
h1 = gca;
%Create the second axes at the same location before plotting the second dataset.
h2 = axes('Position',get(h1,'Position'));
y=lognpdf(C3,log10(muC3n),sigmaC(3));
y=y*AdjFact5;
plot(C3,y*100,'r','LineWidth',2)
set(gca,'XScale','log')
%To ensure that the second axes does not interfere with the first, locate the y-axis on the right side of the
axes, make the background transparent, and set the second axes' x-tick marks to the empty matrix.
set(h2,'YAxisLocation','right','Color','none','XTickLabel',[])
axis([1 1000 0 ymaxn]);
%Align the x-axis of both axes and display the grid lines on top of the bars.
subplot(5,2,7)
bar(C4,D4*100,'k'),grid
%xlabel('Particle size diameter (nm)')
ylabel('% of particles(N)')
set(gca,'XScale','log')
axis([1 1000 0 ymaxn]);
h1 = gca;
%Create the second axes at the same location before plotting the second dataset.
h2 = axes('Position',get(h1,'Position'));
y=lognpdf(C4,log10(muC4n),sigmaC(4));
y=y*AdjFact7;
plot(C4,y*100,'r','LineWidth',2)
set(gca,'XScale','log')
%To ensure that the second axes does not interfere with the first, locate the y-axis on the right side of the
axes, make the background transparent, and set the second axes' x-tick marks to the empty matrix.
set(h2,'YAxisLocation','right','Color','none','XTickLabel',[])
axis([1 1000 0 ymaxn]);
%Align the x-axis of both axes and display the grid lines on top of the bars.
%subplot(5,2,9) %same as before
%New location
subplot(5,2,5)
%************
bar(C5,D5*100,'k'),grid
%xlabel('Particle size diameter (nm)')
ylabel('% of particles(N)')
set(gca,'XScale','log')
axis([1 1000 0 ymaxn]);
h1 = gca;
%Create the second axes at the same location before plotting the second dataset.
h2 = axes('Position',get(h1,'Position'));
y=lognpdf(C5,log10(muC5n),sigmaC(5));
y=y*AdjFact9;
plot(C5,y*100,'r','LineWidth',2)
set(gca,'XScale','log')
%To ensure that the second axes does not interfere with the first, locate the y-axis on the right side of the
axes, make the background transparent, and set the second axes' x-tick marks to the empty matrix.
set(h2,'YAxisLocation','right','Color','none','XTickLabel',[])
axis([1 1000 0 ymaxn]);
%Align the x-axis of both axes and display the grid lines on top of the bars.
%****************************************************
%Volume distribution graphs
%Plot y-scale-maxium
```

```
ymaxv=5;
muC1=82.871;
muC2=54.538;
muC3=41.305;
muC4=40.897;
muC5=24.826;
AdjFact2=0.07;
AdjFact4=0.03;
AdjFact6=0.04;
AdjFact8=0.04;
AdjFact10=0.06;
%subplot(5,2,2) %same comment
%New location
subplot(5,2,4)
%************
bar(C1,E1*100,'k'),grid
%xlabel('Particle size diameter (nm)')
ylabel('% of particles(V)')
set(gca,'XScale','log')
axis([1 1000 0 ymaxv]);
h1 = gca;
%Create the second axes at the same location before plotting the second dataset.
h2 = axes('Position',get(h1,'Position'));
y=lognpdf(C1,log10(muC1),sigmaC(1));
y=y*AdjFact2;
plot(C1,y*100,'r','LineWidth',2)
set(gca,'XScale','log')
%To ensure that the second axes does not interfere with the first, locate the y-axis on the right side of the axes, make the background transparent, and set the second axes' x-tick marks to the empty matrix.
set(h2,'YAxisLocation','right','Color','none','XTickLabel',[])
axis([1 1000 0 ymaxv]);
%Align the x-axis of both axes and display the grid lines on top of the bars.
%subplot(5,2,4)
%New location
subplot(5,2,2)
%************
bar(C2,E2*100,'k'),grid
%xlabel('Particle size diameter (nm)')
ylabel('% of particles(V)')
set(gca,'XScale','log')
axis([1 1000 0 ymaxv]);
h1 = gca;
%Create the second axes at the same location before plotting the second dataset.
h2 = axes('Position',get(h1,'Position'));
y=lognpdf(C2,log10(muC2),sigmaC(2));
y=y*AdjFact4;
plot(C2,y*100,'r','LineWidth',2)
set(gca,'XScale','log')
%To ensure that the second axes does not interfere with the first, locate the y-axis on the right side of the axes, make the background transparent, and set the second axes' x-tick marks to the empty matrix.
set(h2,'YAxisLocation','right','Color','none','XTickLabel',[])
axis([1 1000 0 ymaxv]);
%Align the x-axis of both axes and display the grid lines on top of the bars.
%subplot(5,2,6)
%New location
subplot(5,2,10)
%************
bar(C3,E3*100,'k'),grid
xlabel('Particle size diameter (nm)')
```

```
  ylabel('% of particles(V)')
  set(gca,'XScale','log')
  axis([1 1000 0 ymaxv]);
  h1 = gca;
  %Create the second axes at the same location before plotting the second dataset.
  h2 = axes('Position',get(h1,'Position'));
  y=lognpdf(C3,log10(muC3),sigmaC(3));
  y=y*AdjFact6;
  plot(C3,y*100,'r','LineWidth',2)
  set(gca,'XScale','log')
  %To ensure that the second axes does not interfere with the first, locate the y-axis on the right side of the
axes, make the background transparent, and set the second axes' x-tick marks to the empty matrix.
  set(h2,'YAxisLocation','right','Color','none','XTickLabel',[])
  axis([1 1000 0 ymaxv]);
  %Align the x-axis of both axes and display the grid lines on top of the bars.
  subplot(5,2,8)
  bar(C4,E4*100,'k'),grid
  %xlabel('Particle size diameter (nm)')
  ylabel('% of particles(V)')
  set(gca,'XScale','log')
  axis([1 1000 0 ymaxv]);
  h1 = gca;
  %Create the second axes at the same location before plotting the second dataset.
  h2 = axes('Position',get(h1,'Position'));
  y=lognpdf(C4,log10(muC4),sigmaC(4));
  y=y*AdjFact8;
  plot(C4,y*100,'r','LineWidth',2)
  set(gca,'XScale','log')
  %To ensure that the second axes does not interfere with the first, locate the y-axis on the right side of the
axes, make the background transparent, and set the second axes' x-tick marks to the empty matrix.
  set(h2,'YAxisLocation','right','Color','none','XTickLabel',[])
  axis([1 1000 0 ymaxv]);
  %Align the x-axis of both axes and display the grid lines on top of the bars.
  %subplot(5,2,10)
  %New location
  subplot(5,2,6)
  %************
  bar(C5,E5*100,'k'),grid
  %xlabel('Particle size diameter (nm)')
  ylabel('% of particles(V)')
  set(gca,'XScale','log')
  axis([1 1000 0 ymaxv]);
  h1 = gca;
  %Create the second axes at the same location before plotting the second dataset.
  h2 = axes('Position',get(h1,'Position'));
  y=lognpdf(C5,log10(muC5),sigmaC(5));
  y=y*AdjFact10;
  plot(C5,y*100,'r','LineWidth',2)
  set(gca,'XScale','log')
  %To ensure that the second axes does not interfere with the first, locate the y-axis on the right side of the
axes, make the background transparent, and set the second axes' x-tick marks to the empty matrix.
  set(h2,'YAxisLocation','right','Color','none','XTickLabel',[])
  axis([1 1000 0 ymaxv]);
  %Align the x-axis of both axes and display the grid lines on top of the bars.
  %*****************************************************************
  %Figure 3
  %*****************************************************************
  figure(3);
  y=lognpdfian(C1,log10(muC1n),sigmaC(1));
```

```
%y=lognpdf(C1,log(muC1n),sigmaC(1));
plot(C1,y,'r','LineWidth',2)
set(gca,'XScale','log')
%***************************************************************
%Calculates the values of the Bartlett's test for sample comparison
%***************************************************************
%Data
k=5; %Number of samples
Niminusone=0;
NiminusoneSi2=0;
NiminusonelnSi2=0;
for i=1:k
   Ni=F(i);
   Si=sigmaC(i);
   Si2=Si*Si;
   Niminusone=Niminusone+(Ni-1);
   NiminusoneSi2=NiminusoneSi2+(Ni-1)*Si2;
   NiminusonelnSi2=NiminusonelnSi2+(Ni-1)*log(Si2);
end
Sp2=NiminusoneSi2/Niminusone;
B=log(Sp2)*Niminusone-NiminusonelnSi2;
%*************************************
%Creates a file of the raw data so that mu and sigma of the log-normal
%distribution can be calculated
%*************************************
C1=C1';
B1=B1';
C2=C2';
B2=B2';
C3=C3';
B3=B3';
C4=C4';
B4=B4';
C5=C5';
B5=B5';
save('text','C1','B1','C2','B2','C3','B3','C4','B4','C5','B5','-ASCII');
```